

*Proceeding Book of  
First Conference for Engineering Sciences  
and Technology (CEST-2018)  
(Part 3)*

Oil and Chemical Engineering

*25-27 September 2018  
Garaboulli - Libya*

## Table of Contents

Synthesis gas production with high hydrogen concentration aspen simulation.....	250
A Stochastic Optimisation Technique for Tuning a Continuous Stirred Tank Reactor Controllers .....	259
CO <sub>2</sub> Corrosion Inhibitor Assessment Using Various Measurement Techniques in oilfield.....	266
Verification of the reserve of Al-Hamada oil field V-NC6 area by application of well logs. ....	275
Boilers Performance Evaluation of Zuara Desalination Plant.....	287
Estimation of Original Oil in Place for Belhedan Oil Field by Using Volumetric Method, Material Balance Equation Method, and Reservoir Simulation Method .....	295
Pressure Transient Analysis by Using MS. Excel Sheet and Computer Programming.....	307
Evaluation Of Corrosion Resistance Of Mild Steel And Aluminium Using Anodic Inhibitor Method And Passivity.....	318
Optimum Deposition of Tungsten Oxide on Titania Nanotubular Arrays and Study the Photo activity of Nano-Composite Photoanode .....	324
Modeling the Effect of CO <sub>2</sub> on Thermodynamic Behavior of CO <sub>2</sub> /Libyan Natural Gas Mixture .....	336
Novel Green Sorbents Derived from <i>Mesembryanthemum</i> -Based Biomass for Wastewater Treatment Applications.....	345
Novel Green Photocatalysts Derived from Date Syrup-based biomass/TiO <sub>2</sub> for Photocatalytic Oxidation of Methylene Blue Dye in Aqueous Solutions.....	355

## Synthesis gas production with high hydrogen concentration aspen simulation

Abdalhamed A. E. Musbah<sup>1\*</sup>, Salah.M.Algoul<sup>2</sup>, Abdalbaset M.R. Algish<sup>3</sup>, EisaA. abdalaslam<sup>4</sup>  
<sup>1</sup>almazuod@yahoo.com, <sup>2</sup>golsasa40@yahoo.com, <sup>3</sup>algishabdalbaset@gmail.com, <sup>4</sup>a.ali.libya2018@gamil.com  
<sup>1,4</sup>Chemical Engineering Department, Awlad Ali High Institute for Science and Technology, Tarhuna, Libya  
<sup>2</sup>Chemical Engineering Department, The High Institute of Engineering Technology -Zliten, Libya  
<sup>3</sup>Chemical and Petroleum Department, The Higher Institute for Science and Technology, Garaboulli, Libya

### ABSTRACT

There is a growing need for hydrogen and future hydrogen economy becomes high on the scientific agenda, despite the “sustainable” routes are still too expensive; however, Steam reforming of hydrocarbons is the most feasible rout. This paper focuses on the production of Synthesis gas with high hydrogen concentration via process simulation using aspen plus simulator version 2006 and methane as a feedstock; the simulation process aimed mainly to produce synthesis gas rich in hydrogen with a minimum consumption of natural gas and agents of reforming and burning.

An investigation of the effects of reactor (reformer) temperature, steam to natural gas (equivalence ratio) and the oxygen ratio in air on the composition of produced gases are conducted. The combustion reactor operated over a temperature range of 500-900 °C while varying equivalence ratio from 3:1 to 3:5.

The results show that the hydrogen concentration in the produced gas increased rapidly with increasing reforming temperature and the best rang is (750-850 °C) where the highest conversion was at 850°C. Low equivalence ratio 3:1 is not preferred because it results low hydrogen concentration produced in synthesis gas but equivalence ratio equal to 3:3 is preferred for synthesis process as it results complete combustion of methane present in the feed resulting higher percentage of H<sub>2</sub> in the produced gas. In additional, if the content of O<sub>2</sub> in the air used in the combustion reactor as reforming agent was increased the content of hydrogen in the produced synthesis gas increased and on the other hand the content of nitrogen which is an inert gas is decreased by approximately(7.99%). However, 70 % O<sub>2</sub> by volume content in the air stream ensures that the content of hydrogen (63.28%) in compared with pure oxygen gives 63.57%.

**Keyword**— Synthesis gas, hydrogen, simulation.

### 1. Introduction

The use of hydrogen for petrochemicals, fertilizers and as energy carrier in connection with renewable energy production will increase substantially in the next 5-10 years as even more stringent environmental legislation is enforced, Low sulphur gasoline and diesel fuels will become mandatory and harmful emissions will be reduced drastically. Hydrogen will be required by refiners and specialty chemical manufacturers to meet the global need for cleaner products. The growing fuel cell market will be dependent on hydrogen as a primary fuel source [1]. However, the major sources of energy in the world are the traditional fossil fuels (oil, coal and

natural gas) and on consequence of global economic development, especially in the recent decades led to a significant decrease in these non-renewable resources .

In addition, the increasing of energy demands will speed up the exhaustion of the finite fossil fuel, with the current proved reserves and flows, years of production left in the ground coal 148 years, oil 43 years, natural gas 61 years according to scientist's studies [2].

However, non-renewable resources of fossil fuels have led to serious energy crisis and environmental problems such as global warming pollutant emission and acid rain. Carbon dioxide is the main greenhouse gas. The major part of CO<sub>2</sub>emissions is due to combustion of fossil fuels. In addition, combustion of fossil fuel produces toxic gases, such as SO<sub>2</sub>, NO<sub>x</sub> and other pollutants[3].

For these reasons the necessity importunate to find another substitute .Where many efforts have been made to explore clean energy and renewable alternatives such as bio fuels and hydrogen, Hydrogen can replace the conventional fossil fuels because hydrogen overcome fossil fuel and it has the highest energy to weight ratio compared to any fuel[4].

Besides using hydrogen as a source of energy, hydrogen can be used for various other purposes in different industries in hydrogenation process such as saturate compounds and crack hydrocarbons as well as in manufacturing of different chemicals like ammonia, methanol etc. [5].Hydrogen considered as the “fuel of the future” because it is applicable to the technologies which are relating to fuel cells [6].

There are many methods to produce hydrogen but reforming natural gas is a current process of hydrogen production, economical and widely used, provides for short and medium – term energy security and environment friendly, however, producing high concentration synthesis gas is the main drawback of this process.

The reforming reactions correlated with the proprieties package for there former equipment are:



The combustion reaction correlated with the proprieties package for the combustor equipment is:



The equilibrium reaction correlated with the proprieties package for the all three equilibrium reactors is:



Steam reforming process involves the conversion of methane and water vapour into hydrogen and carbon monoxide the conversion is carried out at temperatures of 700 to 850 °C and pressures of 3 to 25 bars. The product contains approximately 12 % CO which can be further converted to CO<sub>2</sub> and H<sub>2</sub> through the water-gas shift reaction [7].

In this paper, a steam reforming process studied and simulated to reach the maximum hydrogen concentration in produced synthesis gas. Thus, one of the advantages of these simulations is to produce hydrogen rich fuel gas and to reduce the percentage of unwanted gas for fuel cell system and environment.

**Table1:** thermodynamic characteristics of the reactions presented above [8]:

	standard heat of reaction(KJ/Kgmol) at 25°C	equilibrium constant at 800°C
reaction 1	2.1X 10 <sup>5</sup>	0.0313
reaction 2	1.6X 10 <sup>5</sup>	0.0166
reaction 3	-8X10 <sup>5</sup>	1.8X10 <sup>17</sup>
reaction 4	-4.2X10 <sup>4</sup>	4.063

The values for the proprieties of the gaseous phases implied in the reforming process were chosen from specialty literature. Table2shows the initial condition of the streams [9].

**Table2:** the initial stoichiometric composition and conditions of first iteration simulation

component mole fraction %	natural gas	Air	Combustion steam	reforming steam
H <sub>2</sub> O	-	-	1	1
CH <sub>4</sub>	1	-	-	-
CO	-	-	-	-
CO <sub>2</sub>	-	-	-	-
H <sub>2</sub>	-	-	-	-
N <sub>2</sub>	-	0.79	-	-
O <sub>2</sub>	-	0.21	-	-
Temperature °C	25	350	400	500
pressure atm	1	1	1	1

## 2. Process Description

Four reactors needed in a typical process of synthesis gas production [3]. However, the proposed simulation model requires three reactors, firstly, the Reformer: The reformer is an equilibrium reactor, in which most of them ethane is reacted with steam to produce hydrogen, carbon monoxide and carbon dioxide. The outlet gas will also contain the un-reacted methane and excess water vapour from the steam. The two reforming reactions are endothermic therefore heat must supply into the reactor to maintain the reactor temperature.

The temperature of combustor feed is simulated to find the best temperature, which maximizes the reacted methane.

Secondly, the Combustor: the combustor is a conversion reactor where, the feed streams include the reformer product and an air stream. The oxygen in the air almost consumed in the combustion of the rest of unreformed methane to produce carbon monoxide and carbon dioxide. Depending on the content of oxygen in the air, the synthesis gas composition is changing.

Finally, Shift reactors: the shift reactors is an equilibrium reactor within the water-gas shift reaction occurs. In the combustor shift reactor the produced carbon monoxide is converted to carbon dioxide and more hydrogen is produced. The natural gas is reformed in a conversion reactor (Reformer) when it is combined with steam.

The proposed flow sheet of the feedstock, architecture of the model and the intermediary or final products are shown in figure 1.

### 3. Methodology

This conceptual model was realized in HYSYS software according with the existing technologies. The Soave Redlich kwong (SRK) equation of state has extensively used in calculating phase and reaction equilibrium. It gives good agreement with experiments it was used to calculating the reaction equilibrium to correct the non-ideality of the gas mixture.

The synthesis gas Production was simulated using the Aspen Hysys V6.software where the following parameters simulated to find out their effects on purity and productivity of produced synthesis gas, and to increase the hydrogen produced volume fraction. These parameters are including reformer temperature, the mole ratio of natural gas to air (equivalence Ratio) used to burn it, the reforming / combustion agent (mixture steam – air with different concentration of O<sub>2</sub>); and the volumetric composition (v/v%) of the gases resulting from the reforming / combustion process of natural gas. The process takes place at atmospheric pressure.

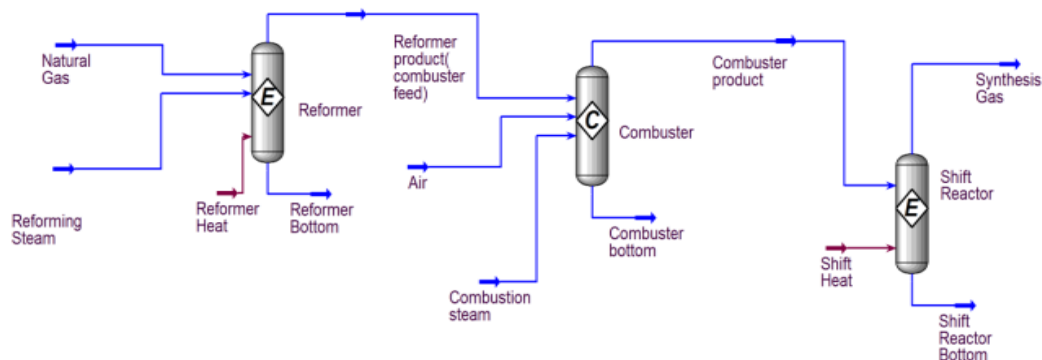


Figure 1: synthesis process flow diagram

#### 4. Results and Discussion

To initialize the process and to run the simulation, the values for the properties of the gaseous phases implied in the reforming processes were chosen from specialty literature and shown in table 2.

##### 4.1. Effects of varying reformer temperature on methane reforming process and produced synthesis gas composition (CO & +H<sub>2</sub>) at constant equivalence ratio.

Form first iteration simulation forstoichiometric mole quantity of reforming process at inlet conditions it can be clearly seen that by increasing the reforming temperature the conversion of methane increased. However, the volume fraction of CO is increased and this will make the process need more shifting reaction in the third reactor to convert CO to CO<sub>2</sub> and H<sub>2</sub>. For this reason the equilibrium reaction at 850 °C was chosen for the simulation where it gives highest methane conversion and in next reactor the produced Carbone monoxide will be eliminated.

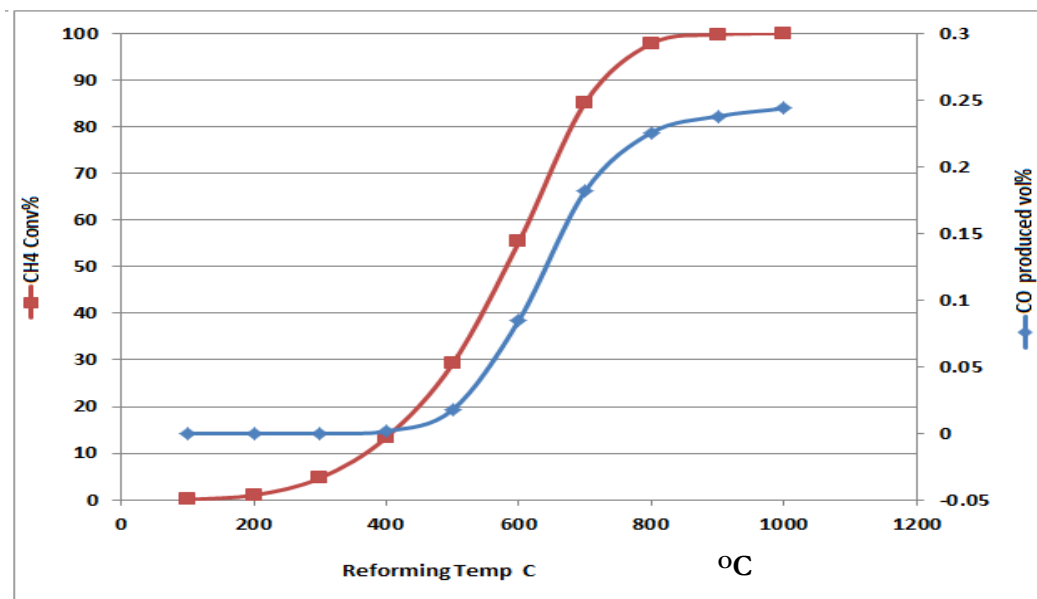


Figure 2: Reforming temperature effects on methane conversion and produced CO Vol fraction.

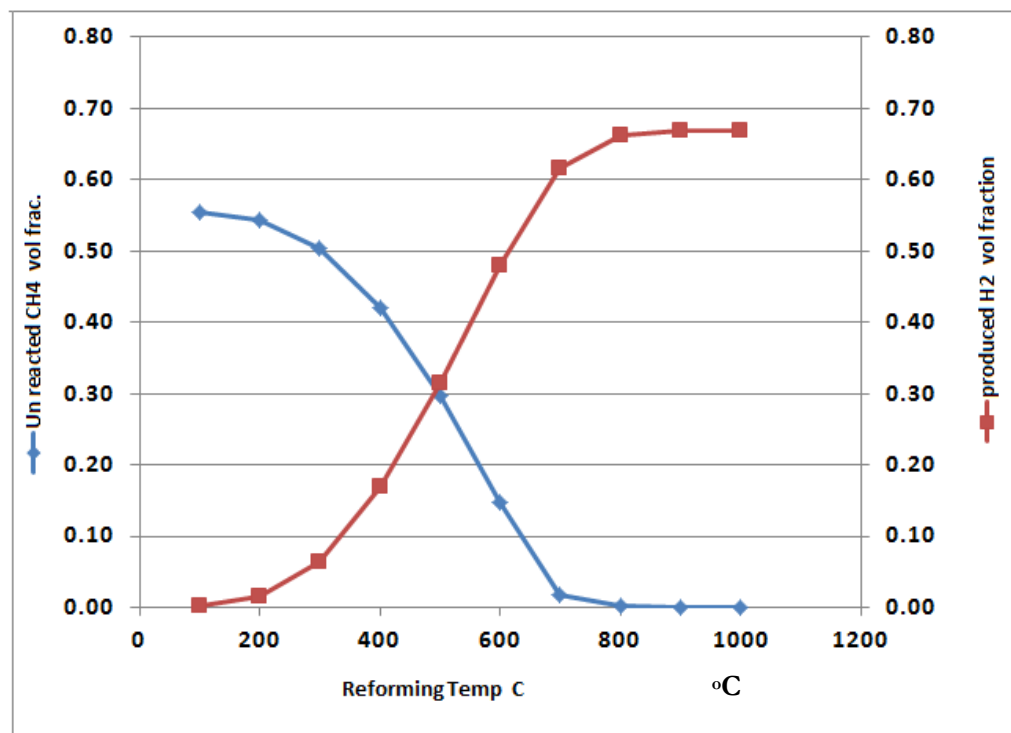


Figure3: Reforming temperature effects on produced hydrogen and unreacted methane vol fraction

From figures above, when temperature become greater than 700 °C, the volume fraction of unreacted methane approach 1 or 2 volumes present and the produced hydrogen reach the maximum value.

The addition of oxygen in the second reactor serves to the purpose of ensuring that the excess of methane from the natural gas stream is consumed and since reforming reactions, is an exothermic reaction, the product gas composition is sensitive toward temperature change and it was observed that the concentration of H<sub>2</sub> increases with increase in temperature. Higher temperature provides more favourable condition for steam reforming of methane therefore, with increasing in temperature the concentration of methane decreases in the product gas and this is attributed to increase in concentration of hydrogen. On the other hand, the CO<sub>2</sub> concentration decreases with increase in temperature because higher temperature favours endothermic formation of CO from CO<sub>2</sub> via reverse reaction.

#### 4.2. Effects of varying equivalence ratio (steam to methane) on produced synthesis gas composition (CO & H<sub>2</sub>)

Equivalence ratio is the most important parameter of synthesis process. The effect of equivalence ratio on product synthesis gas composition was studied in the range 3:1 to 3:5 at 850 °C. Figure4 shows CO<sub>2</sub> volume

fraction is directly proportional to the equivalence ratio to specific limit. Equivalence ratio (methane to steam equal to 2 or 3) gives the highest hydrogen volume fraction, and small carbon dioxide volume produced. With increasing in equivalence ratio, more complete synthesis process takes place producing more H<sub>2</sub> and this leads to decrease in concentration of CO, so less CO is produced from water gas shift reaction. However, it can increase the carbon monoxide and in this case, it needs to be eliminated in equilibrium reactor and convert it to CO<sub>2</sub> according to the equilibrium reaction.

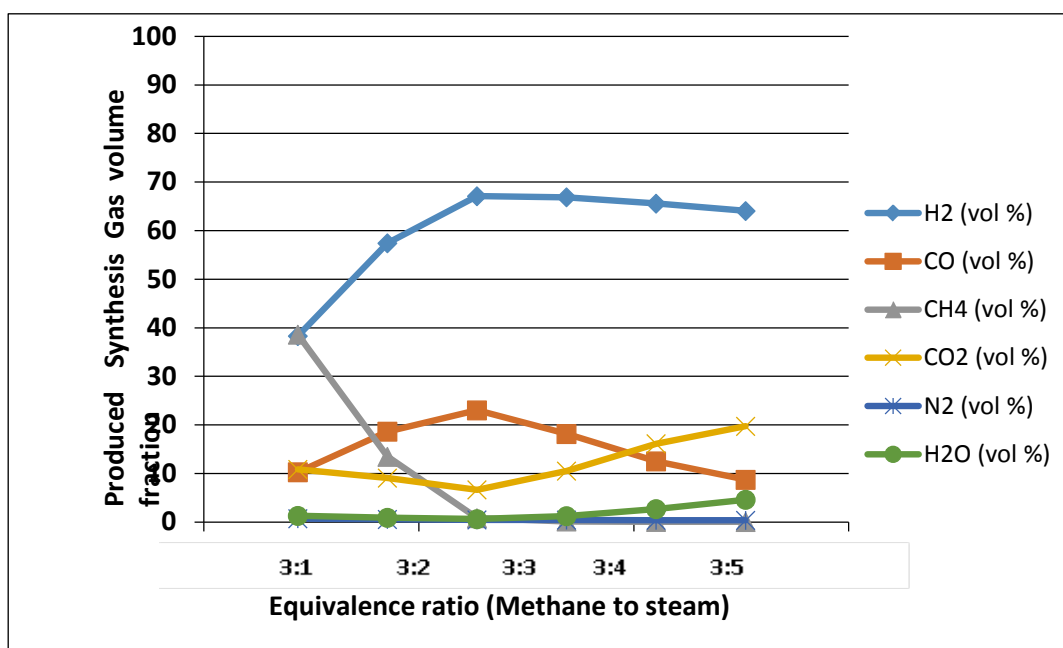


Figure 4: Simulated product gas composition (volume %) at different temperatures

#### 4.3. Effects of varying oxygen mole fraction in air on produced synthesis gas composition at different equivalence ratio

In the conversion reactor, if the temperature in reformer reactor is less than 800 °C some amount of methane can be unconverted and in this case it needs to convert into CO<sub>2</sub> and H<sub>2</sub>O via enhancing the combustion reaction. In the case of steam to methane used was 3:2 at temperature 750 °C, and air with different content in O<sub>2</sub> varied from 21 volumes present to 100% were used, the simulation process of the natural gas reforming gives the follow results for the ratio of Oxygen required to burnet the unreacted methane is equal to 2 : 1 stoichiometric.

If the concentration of O<sub>2</sub> in the air used in the second reactor, combustor reactor increased, the concentration of hydrogen in synthesis gas product will increase and as a secondary effect will decrease the

concentration of nitrogen, which is an inert gas where, for a concentration of 50% O<sub>2</sub> it was obtained the best results of the simulation process: 63% H<sub>2</sub> and 4.03% N<sub>2</sub>.

It can be recommended to balance the amount of air to combust the remains un reacted CH<sub>4</sub> and the amount of water required in the equilibrium reactor to eliminate the un reacted methane, it recommended that it is better to carry out the reforming reaction in temperature about 850oC and the required amount of air can be cut down to become near zero, however, the results are shown in table (3), where the best equivalence ratio is 3:3.

**Table3:** the simulated volume fraction of produced synthesis gases

Parameters	CH <sub>4</sub> Vol %	H <sub>2</sub> OVol%	COVol%	CO <sub>2</sub> Vol%	H <sub>2</sub> Vol%	N <sub>2</sub> Vol%	O <sub>2</sub> Vol%
<b>equivalence ratio</b>	<b>3:1</b>						
Air with 21% Vol O <sub>2</sub>	0.3427	0.035	0.0428	0.1334	0.3538	0.0926	0.000
Air with 50%Vol O <sub>2</sub>	0.3204	0.0507	0.0383	0.1691	0.3622	0.0593	0.00
Air with 70%Vol O <sub>2</sub>	0.3050	0.0623	0.0361	0.1930	0.3677	0.0359	0.00
Air with 100% Vol O <sub>2</sub>	0.2815	0.0807	0.0337	0.2284	0.3757	0.000	0.00
<b>equivalence ratio</b>	<b>3:2</b>						
Air with 21% Vol O <sub>2</sub>	0.1322	0.0201	0.1111	0.1329	0.5293	0.0744	0.000
Air with 50% Vol O <sub>2</sub>	0.1117	0.0290	0.1010	0.1707	0.5404	0.0473	0.000
Air with 70%Vol O <sub>2</sub>	0.0974	0.0357	0.0951	0.1955	0.5477	0.0285	0.00
Air with 100% Vol O <sub>2</sub>	0.0760	0.0467	0.0877	0.2313	0.5583	0.000	0.00
<b>equivalence ratio</b>	<b>3:3</b>						
Air with 21% Vol O <sub>2</sub>	0.0109	0.0178	0.1483	0.1331	0.6265	0.0634	0.000
Air with 50% Vol O <sub>2</sub>	0.0072	0.0192	0.1466	0.1409	0.6309	0.0403	0.0150
Air with 70% Vol O <sub>2</sub>	0.0072	0.0193	0.1470	0.1413	0.6328	0.0242	0.0281
Air with 100% Vol O <sub>2</sub>	0.0072	0.0194	0.1477	0.1420	0.6357	0.000	0.048
<b>equivalence ratio</b>	<b>3:4</b>						
Air with 21% Vol O <sub>2</sub>	0.1015	0.0132	0.1481	0.1075	0.5739	0.0558	0.000
Air with 50% Vol O <sub>2</sub>	0.0858	0.0186	0.1380	0.1390	0.5831	0.0354	0.000
Air with 70% Vol O <sub>2</sub>	0.075	0.0227	0.1318	0.1600	0.5893	0.0213	0.000
Air with 100%Vol O <sub>2</sub>	0.0588	0.0293	0.1233	0.1903	0.5984	0.0000	0.000

Theoxygen from the air is consumed in an exothermic combustion reaction while the inert nitrogen passes through the system but if the content of oxygen in the air is raised, the effect is increasing of hydrogen content in the synthesis gas and decreasing the nitrogen content, these effects are desirable because the hydrogen is the final product and nitrogen is a useless inert gas.

It gives the highest produced hydrogen volume fraction but in contrast it is clearly seen that the volume fraction of un converted carbon oxide is greater than some others, therefore, this process has a complexity that make it not easy to optimize the required amount using the simple software.

## 5. Conclusions

Using ASPEN PLUS simulator, a model for synthesis gas production in an atmospheric process was simulated using natural gas (Methane) as feed material. A series of simulations were carried on to investigate the effect of temperature, equivalence ratio on produced synthesis gas.

The volume percentages of H<sub>2</sub>, CO, CH<sub>4</sub> and CO<sub>2</sub> were calculated, the results showed that, the hydrogen concentration in the product gas increases rapidly with increase in temperature (750-850 °C). Low equivalence ratio 3:1 is not preferred as it results low hydrogen concentration produced in synthesis gas. However, Equivalence ratio 3:3 is preferred for synthesis process as it results complete combustion of methane present in the feed, resulting higher percentage of H<sub>2</sub> in the product gas. High steam to methane ratio results higher water gas shift reaction and this leads to better yield of hydrogen but much higher steam flow rates will have an opposing effect on producing higher CO produced which need higher efficient technique to be separated.

In additional, if the content of O<sub>2</sub> in the air used to the second reactor as reforming agent was increased, the content of hydrogen in the produced synthesis gas is higher and also the content of nitrogen which is an inert gas is decreased where it reaches (7.99%). However, 70 % O<sub>2</sub> by volume content in the air stream ensure that, the content of hydrogen (63.28%) in compared with pure oxygen gives 63.57%.

## References

- [1]. Niels R. Udengaard , hydrogen production by steam reforming of hydrocarbons, Prepr. Pap. -Am. Chem. Soc., Div. Fuel Chem. 2004, 49(2), 907. El Camino Real, Suite 300.Houston, Texas 77058
- [2]. E. Rytter, Method and reactor for reformation of natural gas and simultaneous production of hydrogen, 2001
- [3]. M. R. Beychok, Process and environmental technology for producing SNG and liquid fuels, U.S. EPA report EPA-660/2-75-011, 1975
- [4]. Hartstein, Hydrogen production from natural gas, 2003
- [5]. M. Feidt, Energy efficiency and environment, U.P.B. Sci. Bull., Series C, Vol. 72, Iss. 1, 39-53, 2010
- [6]. S. C. Amendola, M. Binder, M.T. Kelly, P.J. Petillo, S.L. Sharp-Goldman, Advances in Hydrogen Energy, 69–86, 2002. S. Gagnon, Hydrogen. Jefferson Lab., 2008
- [7]. Riis T., Hagen E. F., Vie P. J. S. and Ulleberg O., Hydrogen production and storage R&D: priorities and gaps. Paris, IEA Publications, 2006
- [8]. C. Basagianis, X.E. Verykos, Production of Hydrogen from Biomass via Steam Reforming of Bio-oil, Proceedings International Hydrogen Energy Congress and Exhibition IHEC 2005,Istanbul.
- [9]. Nath K. and Das D., Hydrogen from biomass, Current Science, vol. 85, No. 3, (2003): pp.265-271

# A Stochastic Optimisation Technique for Tuning a Continuous Stirred Tank Reactor Controllers

Yousif A. alsadiq

ysf\_826@yahoo.co.uk

Chemical Engineering Department, Engineering faculty, Sirte University, Libya

## ABSTRACT

A continuous stirred tank reactor mathematical model is developed based on the mass and energy balances for the reactor and heating system. A step change of the concentration is introduced and the temperature change in the reactor is measured. The objective of this paper is to comparatively study the application of PID, Generic Model Control, and Fuzzy logic controllers on the system and evaluate their performances according to the Integral of absolute error resulted. A simulated annealing algorithm is used to tune the controller's parameters. The control and simulation study has been implemented using MATLAB/SIMULINK.

**Keyword**— Mathematical modelling of continuous stirred tank reactor, MATLAB Simulation, PID controller, Generic Model Control, Fuzzy Logic Control, and Simulated Annealing .

## 1. Introduction

Continuous stirred tank reactor systems (CSTR) are the most important unit of a chemical plant used for unit operations. Basically a chemical reactor system has a complex nonlinear dynamic characteristic. There has been considerable interest in its state estimation and real time control based on mathematical modelling. However, the lack of understanding of the dynamics of the process, the highly sensitive and nonlinear behaviour of the reactor, has made it difficult to develop a suitable control strategy. An efficient control of the CSTR can be achieved only through an accurate model [1].

A PID controller represents the simplest form of controller that utilises Derivative and Integral operations on the system. PID controllers have several important functions: they have the ability to eliminate steady-state error through the integral action, and they can cope with actuator saturation, if used with anti-windup. These controllers are also effective for many control problems, particularly where there are a benign process dynamics and modest performance requirements [2]. PID controller can be represented by the following equation.

$$u(t) = K_c \left( \varepsilon(t) + \frac{1}{\tau_i} \int_0^t e(t) dt + \tau_D \frac{d\varepsilon(t)}{dt} \right) \quad (1)$$

Where:  $K_c$  is Proportional constant,  $\tau_i$  is Time integral constant,  $\tau_D$  is Derivative time constant,  $\varepsilon$  error, and  $u$  is the controller output The need for improved process control has become obvious in recent years. Since

1987, there have been growing interest in the use of generic model control (GMC), which has been exposed to have certain robustness for a wide range of process nonlinearity against model mismatches [3]. The desired response can be obtained by incorporating two tuning parameters. More details of GMC method can be found in [4]. Consider a process described by the following equation:

$$\dot{x} = f(x, u, d, t) \quad (2)$$

$$y = g(x) \quad (3)$$

Where  $x$  is the state variable,  $u$  is the manipulated variable,  $d$  is the disturbance variable  $t$  is the time, and  $y$  is the output. In general,  $f$  and  $g$  are some nonlinear functions. It follows from (2) and (3) that:

$$y = G_x f(x, u, d, t) \quad (4)$$

For a specific desired steady state value, the GMC algorithm specifies a rate of change of the output variables as:

$$\dot{y} = K_1(y_{sp} - y) - K_2 \int (y_{sp} - y) dt \quad (5)$$

In (5), two process desires are obvious. First, when the system is at a greater distance from the setpoint, then the system should travel towards the set point more quickly. Moreover, the longer that the system has remained offset from the setpoint, then the system should also travel towards the setpoint more quickly. The values of  $K_1$  and  $K_2$  are what determine the speeds. Therefore, to solve for the control, the actual output rate is set equal to the desired output rate, in other words setting (4) equal to (5), result in the following equation from which the control,  $u$ , can be solved.

$$G_x f(x, u, d, t) = K_1(y_{sp} - y) - K_2 \int (y_{sp} - y) dt \quad (6)$$

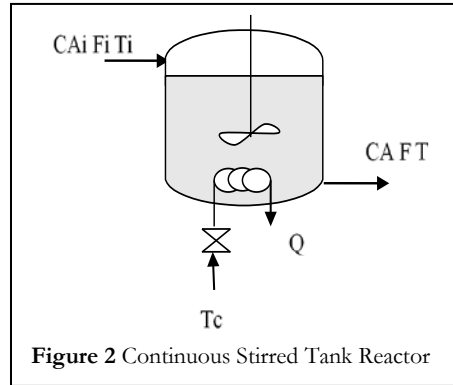
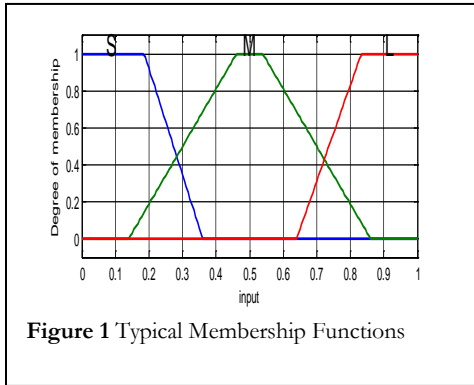
Fuzzy Logic Control has emerged as one of the most active and fruitful areas [5,6]. FLC is based on a spirit that is close to human thinking, and natural language, where the essential part of fuzzy logic is a set of linguistic control rules related by the dual concepts of fuzzy implication and compositional rules of inference [7]. FLC differs from conventional control methods, it incorporates a simple rule-based approach to solve the control problem rather than modelling the system mathematically. It also uses imprecise data, but descriptive of what must happen [8]. Figure 1, shows typical MFs of the controller. Hence the number of MFs used for variable is 3, then the number of rules required to map the input into the output is 3.

## 2. mathematic model of the continuous stirred tank reactor

A mathematical model of a continuous stirred tank reactor is developed depending on mass and energy balances. A summing first order irreversible exothermic reaction ( $A \rightarrow B$ ) in a Continuous Stirred Tank Reactor as shown in Figure 2. The heat generated by the reaction is removed using a cooling coil inside the reactor. Perfectly mixing is assumed in CSTR and the change in volume due to reaction is negligible. The reactor mass and energy equations are:

Over all mass balance

$$\frac{dV}{dt} = F_i - F \text{ and } F_i = F \quad (7)$$



$F_i, F$  are inlet, outlet flow,  $V$  reactor volume,  $t$  is the time,  $C_{Ai}, C_A$  inlet, outlet concentration of component A,  $T_i, T$  inlet, outlet temperature,  $r$  is reaction rate,  $E$  is activation energy,  $R$  is gas constant,  $k_0$  is pre-exponential constant,  $\rho$  is density,  $C_p$ , specific heat capacity,  $H_r$  heat of reaction,  $T_c$  coolant temperature, and  $UA$  is a product of heat transfer coefficient and area.

Component (A) mass balance

$$\frac{dVC_A}{dt} = F_i C_{Ai} - FC_A - rV \quad (8)$$

Where  $r$  is the rate of a first order reaction

$$r = k_0 e^{\frac{-E}{RT}} C_A \quad (9)$$

and  $V$  is constant then (8) can be written as:

$$\frac{dC_A}{dt} = \frac{F}{V} C_{Ai} - \frac{F}{V} C_A - k_0 e^{\frac{-E}{RT}} C_A \quad (10)$$

Heat balance

$$\frac{\rho dVC_p T}{dt} = \rho C_p F_i T_i - \rho C_p F T - H_r V C_A k_0 e^{\frac{-E}{RT}} - UA(T - T_c) \quad (11)$$

Where,  $V$  is constant, and the specific heat  $C_p$  is a function of temperature then from (8), and (11).

$$\frac{dT}{dt} = \frac{F}{V} (T_i - T) - \frac{H_r C_A k_0 e^{\frac{-E}{RT}}}{\rho C_p} - \frac{UA}{\rho C_p V} (T - T_c) \quad (12)$$

### 3. simulated annealing and its application to controller tuning

Simulated annealing is a global search method that is based on the analogy with the physical annealing process of solids [9, 10, 11]. This optimisation technique has been applied to a CSTR for tuning proportional

integral (PI), generic model (GMC), and Fuzzy controllers that are used to control the temperature and the concentration of the process, in MATLAB and SIMULINK environment. More detail on Simulated annealing can be found in [12].

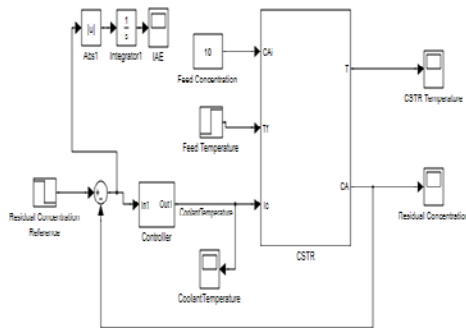


Figure 3 Feedback control system

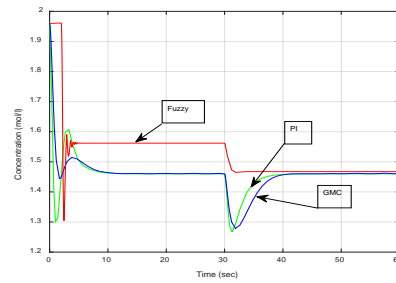


Figure 4 Concentration response of different controllers by conventional settings

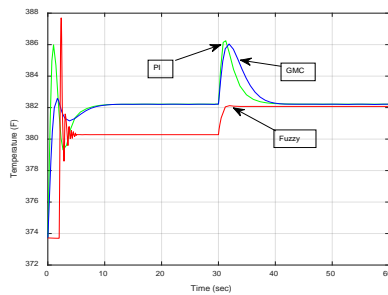


Figure 5 Temperature response of different Controllers by conventional settings

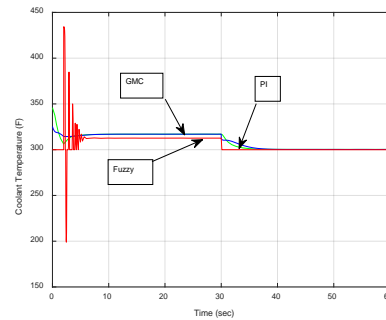


Figure 6 Coolant Temperature response for different Controllers by conventional

#### 4. Simulation Results

The feedback control system can be represented in a Simulink as shown in Figure 3. The performance of the three types of controllers are illustrated below. Figures 4, 5, 6 show the results obtained by conventional settings. However, when applying the stochastic simulated annealing optimization method, the best values of the IAE obtained are 0.1791, 0.1693, 0.2048 for PI, GMC and fuzzy Controllers respectively. Where, the number of investigated solutions used for PI and GMC are 1000, while for Fuzzy controller are 3500 as there are 8 points to be tuned for both input and output membership functions. However, the best solutions were found at a simulation times 905, 655, 548 for PI, GMC, and Fuzzy controllers respectively. Figures 7, 8, 9, 10, 11, 12 and 13 depict the results obtained using (SA) algorithm.

It is obvious that for both PI and GMC controllers an acceptable result can be achieved using conventional tuning methods, but it is very difficult to have a good membership function setting for fuzzy controller using trial and error. While, when applying simulated annealing the performance of the controllers in tracking the step change of the concentration from its initial value of 1.96 to 1.46 mol/l has been achieved. However, the controllers have the capability of eliminating the effect of the feed temperature disturbance from 300 F to 305 F on the concentration which is obvious at 30 sec as can be seen in figures 8, and 9. Moreover, it can be clearly seen in figures 10, and 12 that the Temperature and the coolant Temperature (Controller output) responses are changing according to their dependency to the concentration change, where, it is realized that at the initial concentration value, the temperature is 373.72 F, and the coolant Temperature is 300 F. When the concentration step change introduced at time 2 sec where it has been reduced to 1.46 mol /l, the temperature

value rose to 382.22 F as well as the coolant temperature that rose to 316.9 F. However, at 30 sec when the feed temperature disturbance was added, the controllers quickly overcame the disturbance and brought the temperature back to its steady state value, while the coolant temperature has dropped to 300.3 F which is the required controller value to keep the controlled parameter at its desired value. It is obvious that fuzzy controller response is a bit oscillatory at the start of the step change. Moreover, the fuzzy controller has better overcome of the feed temperature disturbance than the PI and the GMC controllers although it is a bit slower, but on other hand they are much better in eliminating the steady state error. The following table shows the results obtained when tuning the controllers using conventional methods available in MATLAB optimization toolboxes and simulated annealing optimization technique illustrated above.

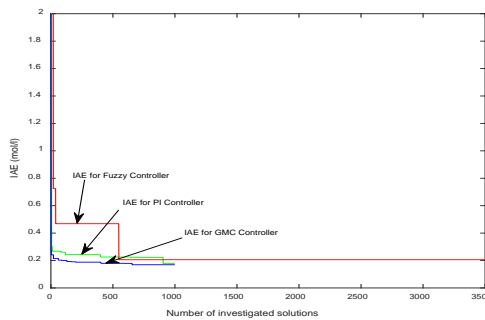


Figure. 7 IAE obtained by SA for using different controllers

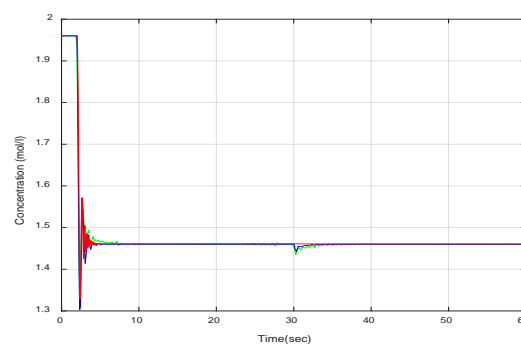
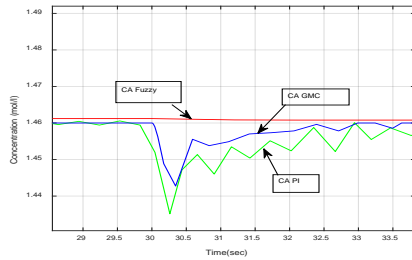
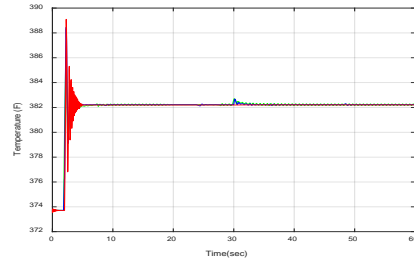


Figure 8 Concentration response of different controllers



**Figure 9** Enlargement of Concentration response of different controllers



**Figure 10** Temperature response of different Controllers

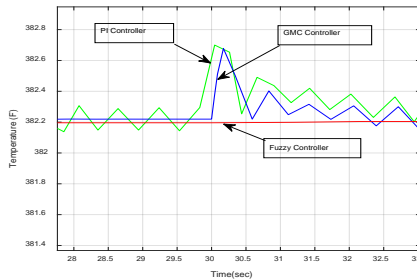


**Figure 11** Enlargement of Temperature response of different Controllers

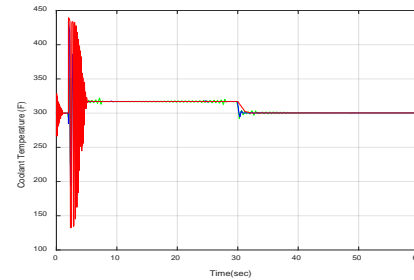


**Figure 12** Coolant Temperature response for different Controllers

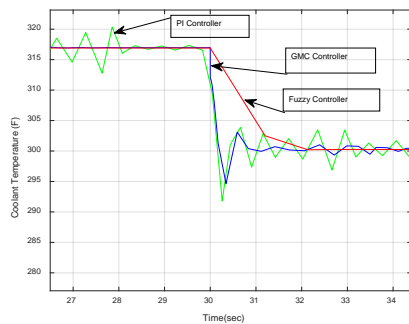


**Figure 13** Enlargement of Coolant Temperature response for different Controllers

**Table 1.** Simulation results

Using Conventional methods	
Controller Type	IAE (mol/l)
PI	1.8992
GMC	1.8606
Fuzzy	4.2093
Using SA algorithm	
PI	0.1791
GMC	0.1693
Fuzzy Logic	0.2048

## 5. Conclusion

Fuzzy Logic Controllers are nonlinear and have the influence of rejecting the disturbances better than the PI, and GMC controllers. Moreover, PI and GMC controllers have the inherent character of eliminating the steady state error which is unbeatable. The table above shows that simulated annealing is a powerful stochastic optimisation search method, where by comparing The IAE obtained using this algorithm to that obtained from conventional methods, it can be clearly seen that simulated annealing has found the best possible parameters that minimise the IAE to its minimum values which gives a better result of controller performance.

## References

- [1]. Suja Malar & Thyagarajan, "Modelling of Continuous Stirred Tank Reactor Using Artificial Intelligence Techniques", Department of Electrical and Electronics Engineering, PET Engineering College of India, Vol.3, pp. 145-155, (2009).
- [2]. WG da Silva; PP Acarnley; JW Finch; 'Tuning of brushless dc drive speed controller with an on-line genetic algorithm', European Power Electronics Conference, Lausanne, 1999.
- [3]. P. L. Lee, G. R. Sullivan. Generic model control (GMC). Computers and Chemical Engineering, 1988, 12(6): 573-580.
- [4]. B. J. Cott, S. Macchietto. Temperature control of exothermic batch reactors using generic model control. Industrial Engineering Chemical Research, 1989, 28(8): 1177-1184.
- [5]. CP. Coleman, D. Godbole: 'A comparison of robustness: fuzzy logic, PID, and sliding mode control', Proceedings of the Third IEEE Conference on Fuzzy Systems, V. 3, P. 1654 -1659, 1994
- [6]. WG da Silva, PP Acarnley, and JW Finch; 'A comparison of fuzzy and conventional speed control in electric drives', European Power Electronics Conference, Lausanne, 1999.
- [7]. N. Gulley, and J. S. Roger Jang, 'Fuzzy logic toolbox for use with MATLAB', The Math Workers Inc., 1995-1999.
- [8]. Haj-Ali, H. Ying; 'Structural analysis of fuzzy controllers with nonlinear input
- [9]. Prof. Song Prof. Irving;" Optimisation techniques for electrical power systems" part 2 Heuristic optimisation methods; Power Engineering Journal, P.151-160, June 2001
- [10]. X. Yao;'A new simulated annealing algorithm', Int. J. Computer Math. V. 56, P.161-168, 1995.
- [11]. Z. Xiaoyum, H. Yun, D. John; 'Genetic algorithms and simulated annealing for robustness analysis', Proceedings of the American Control Conference, V. 6, P. 3756-3760, 1997.
- [12]. Z. Xiaoyum, H. Yun, D. John; 'Genetic algorithms and simulated annealing for robustness analysis', Proceedings of the American Control Conference, V. 6, P. 3756-3760, 1997.
- [13]. Y. Alsadiq 'A Comprehensive Tuning of Distillation Column Composition Controllers using Simulated Annealing ', Int'l Conference on Artificial Intelligence, Energy and Manufacturing Engineering (ICAEME'2014), P. 35- 41, June 9-10, 2014 Kuala Lumpur (Malaysia)

# CO<sub>2</sub> Corrosion Inhibitor Assessment Using Various Measurement Techniques in oilfield

Abdelrazag Aziz

amaziz@elmergib.edu.ly

Department of Chemical and Petroleum, College of Engineering, Elmergib University, Libya

## ABSTRACT

Tests and evaluation studies were conducted to select the best performance and treating rich carbon dioxide fluid composition associated with crude oil are produced. The experiments include standard electrical resistance probe for direct corrosion monitoring technique, and inspection by using an ultrasonic test to assess corrosion inhibitor.

The improvement process for chemical treatments development requires an effective strategy. The effective process for field testing inhibitor required twenty-four days to determine inhibitor performance and verifying minimum effective concentration. The standard electrical resistance probe with changeable dosage test was utilized. Ultrasonic testing one of the most widely used non-intrusive techniques is applied to measure of localized corrosion. Measurement apparatuses are adequate systems for monitoring of treatment efficiency.

**Keyword**— corrosion monitoring, CO<sub>2</sub> corrosion inhibitor, standard electrical resistance.

## 1. Introduction

Corrosion inhibitors are applied to decrease the rate of internal corrosion in pipelines carrying oil and gas from wells to oilfields and processing plants; even so, no single inhibitor claims all situations. The efficiency of an inhibitor is determined not only by the characteristics of the gas, crude oil and associated water of the pipeline and by the characteristics of the inhibitor itself, but the operating conditions of the oilfield (temperature, pressure, and flow rate) [1].

Because of the complication involved in evaluating corrosion inhibitors, the variety of measurement techniques to evaluate inhibitors, the costs coupled with assessing and utilizing corrosion inhibitors to decrease the rate of internal corrosion of pipelines, and the widespread utilizes of inhibitors, it is important to assess inhibitor performance and verifying minimum effective concentration that are measuring quality and quantity of inhibitors.

Knowledge of the inhibitor performance by measurement techniques has historically been used to control whether a system is protected. This requires confidence in the correlation between measurement techniques results and oilfield conditions. If the amount of corrosion inhibitors present in the oilfield is established at minimum effective concentration, then the system is considered protected and economic. As water chemistry changes, such tests need to be repeated to ensure their relevance to current oilfield conditions.

The study has been executed to identify dosage injected of corrosion inhibitor into the crude oil well. The well has been injected in the annulus where it should provide corrosion protection for the tubing. This well is high CO<sub>2</sub> producing and as such have a history of CO<sub>2</sub> induced pitting corrosion on the tubing found during work over. The corrosion inhibitor being injected down hole into the casing to ensure the protection of both the tubing and the flow lines of this well.

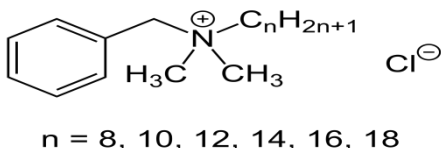
An inhibitor with an efficiency of 90% would be expected to reduce a baseline corrosion rate of 100 mpy down to 10 mpy, which may still not be acceptable based on the corrosion allowance life of oilfield infrastructures. For many conditions inhibitor efficiencies greater than 90% is achievable and desirable, but under certain severe conditions (e.g. highly turbulent flow or slug flow) an efficiency of no better than 70% may be the best attainable. Inhibition efficiency higher than 90% was achieved which is in line with the standard in oilfield [2].

## **2. Chemical Composition and Functionality of Corrosion Inhibitor**

Corrosion inhibitions are chemical treatments that prevent a metallic surface interact with corrosive fluids. This surface is covered to give the surface a certain level of protection. Corrosion inhibitors usually build a film of the adsorbate on the metallic surface of the adsorbent, protecting the metallic surface by creating a film. The life of the film depends on many factors, including the type of inhibitor, dissolved acidic gases, temperature, velocity, water cut, all the latter affecting the corrosive of the system. Continuous treatment is generally the preferred treatment since the concentration of inhibitor can be varied at any given time. A higher concentration of inhibitor can be applied until a film is established, and then the concentration of inhibitor can be reduced to a level enough to maintain the inhibitor film [3].

Several Corrosion inhibitors are available to prevent occurring corrosion, but the effective corrosion inhibitor used in the well is 25% of alkyl dimethyl benzyl ammonium chloride with 25% mixture of aliphatic polyamines in water solution. alkyl dimethyl benzyl ammonium chloride is a corrosion inhibitor designed for use in oil field. The product provides excellent corrosion inhibition in a wide range of environments, including hydrogen sulfide, carbon dioxide and in the presence of trace quantities of oxygen. The product is also effective in the control of bacterially induced corrosion. Physical and chemical properties have been summarized in the Table 1 [4].

**Table 1:** Physical and chemical properties of alkyl dimethyl benzyl ammonium chloride

CAS Number	8001-54-5
Chemical name (CA)	Alkyl dimethyl benzyl ammonium chloride; Quaternary ammonium compounds
Other names	N-Alkyl-N-benzyl-N,N-dimethylammonium chloride; Benzalkonium chloride; ADBAC; BC50.
Molecular formula	$C_9 H_{13} N Cl C_n H_{2n+1}$ where $n = 8, 10, 12, 14, 16, 18$
Structural formula	 <p style="text-align: center;"><math>n = 8, 10, 12, 14, 16, 18</math></p>
Molecular weight (g/mol)	Avg. = 359.6 g/mol
Appearance	100% is white or yellow powder; gelatinous lumps; Solution BC50 (50%) is colourless to pale yellow solutions
Density	0.98 g/cm <sup>3</sup>
Solubility in water (% weight)	100%
Flash point	250 °C (482 °F; 523 K) (if solvent based)

Polyamine refers to a compound that consists of at least two amino groups. It is a highly charged, low molecular weight aliphatic polycation. One of the largest groups of organic corrosion inhibitors is the organic amine group. Aliphatic amines, mono-, di-, or polyamines and their salts, are all used as corrosion inhibitors. Aliphatic amines adsorb by the surface-active -NH<sub>2</sub> groups which forms a chemisorption bond with the metal surface. The hydrocarbon tails orient away from the metal surface toward the solution. Further protection is provided by the formation of a hydrophobic network which excludes water and aggressive ions from the metal surface. Since a lot of metal corrosion is caused by acidic compounds, the basic organic amines can also react with the acidic compound to form an amine salt which then forms a coating on the metal thereby preventing further corrosion of the metal from occurring [5].

The effectiveness of inhibitors depends on the chemical composition, molecular structure, and their attractions with the metal surface. Because film creation is an adsorption process, the operating conditions such as temperature and pressure are important factors for creating the film. Organic corrosion inhibitors will be attracted according to the ionic charge of the inhibitor and the ionic charge on the metallic surface [6].

### 3. Corrosion Rate Measurements

ER probe is generally used for the monitoring and optimization of the chemical treatment efficiency. The locations and positions where ER probes are installed is not always representative of the pipe surface. The flow conditions around probes are different from those on the pipe surface because of the geometry of these elements. The corrosion rates are generally measured on surface filmed by a corrosion inhibitor. the rate of uniform corrosion is generally low and most of the failures are caused by localized corrosion.

#### 3.1. Corrosion Rate and Inhibition Efficiency Calculation

When measuring the ER probe, the instrument produces a linearized signal (S) that is proportional to the exposed element's total metal loss (M). The true numerical value being a function of the element thickness and geometry. In calculating metal loss (M), these geometric and dimensional factors are incorporated into the probe life (P), and the metal loss is given by [7]:

$$M = (S \times P)/1000 \quad (1)$$

Metal loss is conventionally expressed in mils (0.001 inches), as is element thickness.

Corrosion rate (C) is derived by [7]:

$$C = \frac{P \times 365 (S_2 - S_1)}{\Delta T \times 1000} \quad (2)$$

$\Delta T$  being the elapsed time in days between instrument readings  $S_1$  and  $S_2$ .

Efficiency of a corrosion inhibitor is to reduce corrosion rate down to an acceptable level determined by design and operational considerations. The inhibition efficiency was obtained from the corrosion rate (CR) at different concentrations of inhibitor. The efficiency of that inhibitor is thus expressed by a measure of this improvement [8]:

$$\text{Inhibitor Efficiency (\%)} = 100 \times (\text{CR}_{\text{uninhibited}} - \text{CR}_{\text{inhibited}}) / \text{CR}_{\text{uninhibited}} \quad (3)$$

where:  $\text{CR}_{\text{uninhibited}}$  = corrosion rate of the uninhibited system

$\text{CR}_{\text{inhibited}}$  = corrosion rate of the inhibited system

#### 3.2. Evaluating of Corrosion Inhibitor by Electrical Resistance Probe

Corrosion monitoring is a critical part of any oilfield corrosion control program. It should be integrated with other programs designed to optimize the process conditions, chemical injection and inspection to recognize the full potential to successfully manage oilfield operations.

Crude oil transmission pipeline system was operating between a crude oil wellhead terminal and a manifold receiving terminal over several ten miles. Pipeline system crude oil had the water cut 35 % and rich carbon dioxide. An electrical resistance probe was supported before manifold receiving terminal. A corrosion monitoring program was developed to determine if internal corrosion was a problem in the pipeline.

This field evaluation requires approximately 24 days. Figure 1 shows the experimental procedure to estimate minimum effective concentration. the performance is determined using standard electrical resistance probes. This detailed process is designed to qualify an inhibitor formulation for field application. The inhibitor field testing protocol utilizing electrical resistance probes required 12 days to complete an incumbent baseline, 12 days to complete the test using the candidate dosage, for a total of 24 days [9]. Significant information on this technique can be found in ASTM G96 for corrosion monitoring and in NACE Publication 3D170-84.

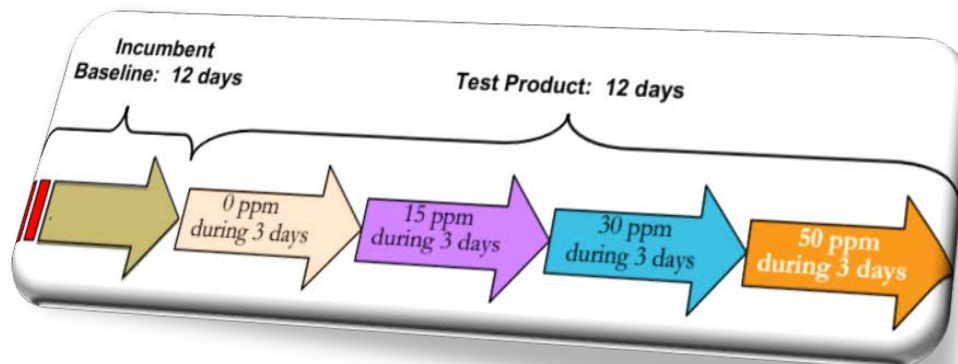


Figure 1: The experiment procedure

### 3.3. Ultrasonic Inspection Test

The limitations of the ER technique are that they provide representative data for general corrosion. They do not have the ability to accurately detect localized attack. The local attack rate can be over ten times the general corrosion rate. Such differences are important when trying to assess the relevance of inspection techniques such as ultrasonic tests of remaining section thickness.

Ultrasonic inspection or ultrasonic testing is applied to measure a variety of material characteristics and conditions. An ultrasonic examination is performed utilizing a device that generates an ultrasonic wave with a piezoelectric crystal at a frequency between 0.1 and 25 MHz into the piece being examined and analyses the return signal. Ultrasonic inspection has been used for decades to measure the thickness of solid objects.

Corrosion Inhibitor has been injected in annuals for approximately two years to protect the inner and outer surface of a tubing string, the flow line and the inner surface of the casing from corrosion. When the pump

failed, and a work over was performed. Two lengths of the pipes were brought; both ends of the pipes were cut-out in different lengths and cut-out in half as samples.

## 4. Results and Discussion

### 4.1. The inhibitor performance and inhibition efficiency

Figures 2 present the data collected from the pipeline of the well. The slope of the metal loss data provides the corrosion rate. uninhibited segment followed by inflexion points or changes in metal loss data. This allows a better analysis of the data, especially at the lower concentrations, leading to an improved understanding of the inhibitor performance at different concentrations.

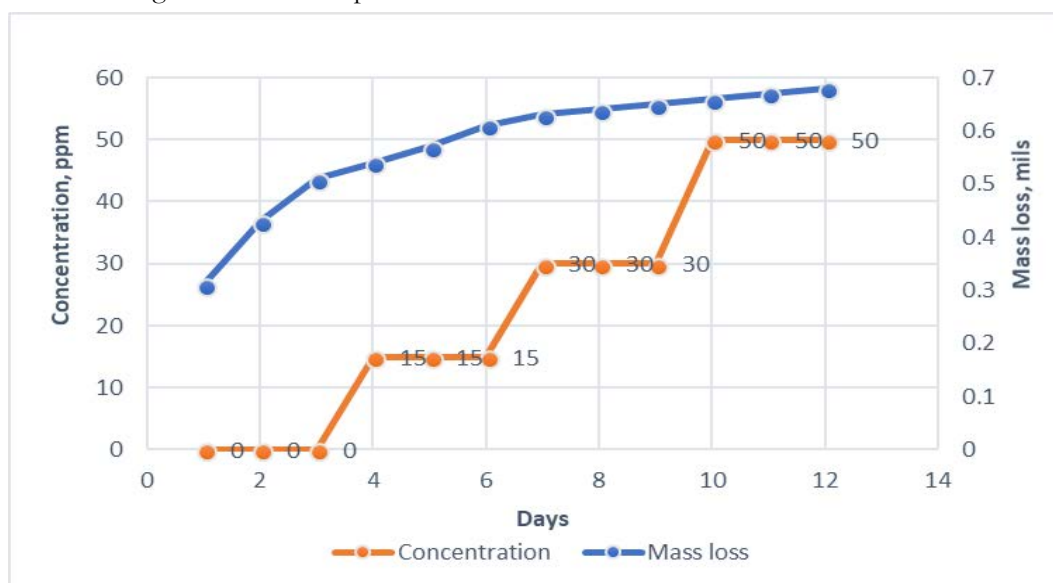


Figure 2: Metal Loss and dosage data by using electrical resistance probe

Figures 3 shows corrosion inhibitor reduced the corrosion rate considerably and the rate decreases with increase in the inhibitor concentration. The uninhibited reading at the rate of 51.1 mpy while 30 ppm concentration reduced the corrosion rates to 3.65 mpy. if the process is prone to rapid changes in corrosivity, ER probes typically may not provide accurate and reliable corrosion rate data. In some cases, namely where  $H_2S$  is present, they can be prone to error due to the presence of conductive sulfide corrosion products on the sensing element which may lead to non-conservative results. While ER data may not give reliable indications of the absolute corrosion rate, they can yield useful indications of trends and changes in corrosion activity [10].

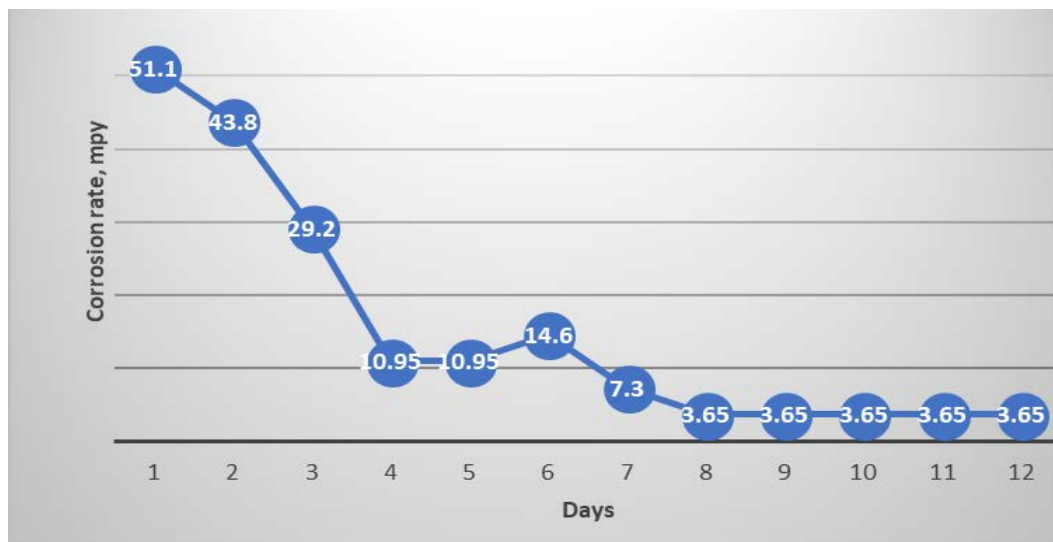


Figure 3: Corrosion rate versus time

Figure 4 shows inhibition efficiency of 93 % was observed at 30 ppm dosage. Moreover, as the concentration increases to 50 ppm, the corrosion performance was constant at the same inhibition efficiency.

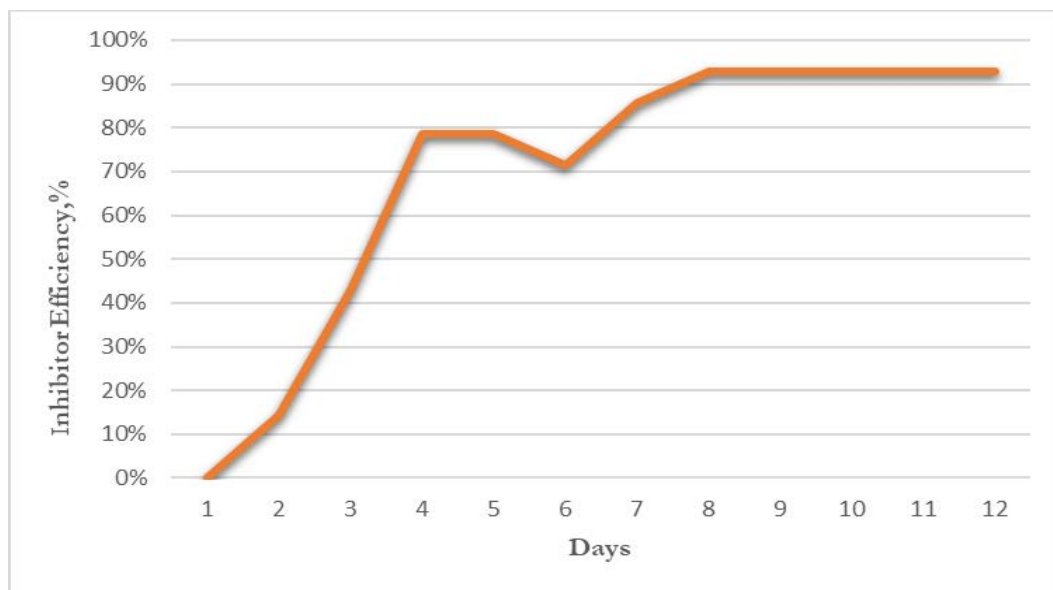


Figure 4: Inhibition efficiency versus time

#### 4.2. localized corrosion Inspection

From the visual inspection performed on the external surface, the pipes appear to be in good condition aside from a thin layer of iron oxide scales were observed, and no signs of any external corrosion were noted at the time of inspection. The internal surfaces of the pipes were in good condition, although the internal surfaces of the pipes were covered with a thin layer of scales. The material was made of carbon steel. All the samples a total in all 8 pieces of the pipes were ultrasonically tested and the normal wall thickness of the pipe is 6.35 mm. The results have been briefly in Table 2.

**Table 2:** Summary of the ultrasonic inspection test

The samples	Minimum Thickness, mm	Maximum Thickness, mm	Findings
Sample No. 1	6.7	7.3	A thin layer of scales
Sample No. 2	6.1	7.5	Minor internal erosion corrosion was observed
Sample No. 3	6.2	7.2	Minor internal erosion corrosion was observed
Sample No. 4	6.5	7.2	A thin layer of scales
Sample No. 5	6.6	7.5	A thin layer of scales
Sample No. 6	6.4	7.5	A thin layer of scales
Sample No. 7	6.2	8.2	Minor internal erosion corrosion was observed
Sample No. 8	6.1	7.3	Minor internal erosion corrosion was observed

#### 5. Conclusions

The chemicals of alkyl dimethyl benzyl ammonium chloride and aliphatic polyamines have been found to be good corrosion inhibitor for the protection of the inner and outer surface of a tubing string, the flow line and the inner surface of the casing from corrosion. The corrosion inhibitor is suitable to protect oilfield infrastructures, where a three-phase and CO<sub>2</sub> - rich fluid combination are present.

The inspection results show that the inspected tubing samples are in good conditions. Thus, local corrosion of carbon steel is effectively decreased by corrosion inhibitor.

#### References

- [1]. Sankara Papavinasam, R. Winston Revie, Milan Bartos, "Testing Methods and Standards for Oilfield Corrosion Inhibitors," *NACE International*, 2004, NACE-04424.

- [2]. Sunday Aribo, Sunday J. Olusegun, Leonard J. Ibhadayi, Akinlabi Oyetunji, Davies O. Folorunso, “Green inhibitors for corrosion protection in acidizing oilfield environment,” *Journal of the Association of Arab Universities for Basic and Applied Sciences*, vol. 24, pp. 34-38, October 2017.
- [3]. J.A. Dougherty, “Effect of Treatment Method on Corrosion Inhibitor Performance,” NACE International, *Corrosion97*, Paper 97344.
- [4]. [https://en.wikipedia.org/wiki/Benzalkonium\\_chloride](https://en.wikipedia.org/wiki/Benzalkonium_chloride)
- [5]. Peter Kusch, Gerd Knupp, Marcus Hergarten, Marian Kozupa, Maria Majchrzak, “Identification of corrosion inhibiting long-chain primary alkyl amines by gas chromatography and gas chromatography–mass spectrometry,” *International Journal of Mass Spectrometry*, no. 263, pp. 45-53, December 2006.
- [6]. <http://www.corrosion-doctors.org/Inhibitors/organic.htm>
- [7]. Mr. Scott Paul, PE “Report for Corrosion Inhibitor Application Tank 120-8, Valero Facility” NACE Corrosion Specialist No. 4163, May 2007.
- [8]. Pierre R. Roberge. “Handbook of Corrosion Engineering,” 1999.
- [9]. Timothy H. Bieri, David Horsup, Ph.D., Melvyn Reading, Richard C. Woollam, “Corrosion Inhibitor Screening Using Rapid Response Corrosion Monitoring,” NACE International CORROSION 2006, Paper 06692
- [10]. <https://www.scribd.com/document/355728522/Corrosion-Monitoring>

## Verification of the reserve of Al-Hamada oil field V-NC6 area by application of well logs.

Tariq Basher <sup>1</sup>, Essa Tabar <sup>2</sup>, Ali Omran <sup>3</sup>

<sup>1</sup> tariq.alkaseh@gmil.com, <sup>2</sup> etabare4@gmail.com, <sup>3</sup> ali\_omran95@yahoo.com

<sup>1,2,3</sup> Department of Petroleum Engineering, College of Engineering, Sirte University, Libya

### ABSTRACT

The motivation behind this paper is to enrich and deepen our knowledge in the field of logging and log interpretation. The ultimate target is to have in situ assaying of a particular zone. In petroleum application this means determining the amount of oil and/ or gas that is contained in the formation. The Geological structure of V- NC6 area in AL-HAMADA oil field has been studied and volumetrically estimated in seeks of the amount of hydrocarbons in the structure. To achieve this, a bunch of well logging data from different wells in V-NC6 area have been reviewed, analyzed and interpreted. Physical properties of the reservoir have been measured which include porosity and water saturation by interpretation of SP log and Induction – Electrical logs. In situ porosity has been determined by applying the Archie's equation on a real data from different resistivity tools. The average porosity of the multi pay zones structure was 14.23 % of the total volume of the reservoir 83336.3 acre ft. The second basic parameter which has been determined for in situ assaying is the saturation of the V- NC6 structure with water and hydrocarbons and they were 30% and 70% respectively. The V- NC6 area in AL-HAMADA oil field volumetrically occupied around 5.44 Million Stock tank barrels of oil.

**Keyword**— well logging; log interpretation; resistivity log, SP log, porosity; Water saturation.

### 1. Introduction

The volume of hydrocarbon reserves is a primary component of an energy company's value. Estimating that volume is a complicated, but essential and regulated, part of the resource industry's business. Geophysical methods continue to advance and are playing a more fundamental role in reservoir assessment (Hardage, 2009; PRMS-AD, 2011). To achieve this, physical properties of the reservoir have to be measured which include porosity and water saturation. Unfortunately, no one tool can give these results. Therefore, tool combinations that will measure porosity and hydrocarbons in place in the reservoir have been developed for various targets. Determining in situ properties (porosity and fluid saturation) can be done by the use of three porosity tool and resistivity tool as well. Those porosity tool that are used normally are the sonic, density and the Neutron porosity tools. A second basic parameters to be determined for in situ assaying is the saturation of the formation with hydrocarbons and water. The V- NC6 area has been owned and running by the Arabian Gulf Oil Company, on November 1976 the reservoir engineers have been estimated the original hydrocarbons in place to be around 5 MM STB, and this value was economically stratified for the operator to

start production from this area. In this paper we tried to redo the same job and estimate the volume of hydrocarbons occupied originally in place.

## 2. Materials and Methods

Al Hamadah al hamra area is located on the southern flank of the Ghadamis basin between lat 29° 00' to 29° 40' N and long 12° 35' to 13° 10' E occupying a strategic position midway between Al Qaraqaf arch to the south and centre of the basin to the north.

Over 1200 ft of sediments are accumulated in the basin and range in age from Precambrian to Paleocene. While most of the lower two-thirds are clastics, the upper third is mostly marine carbonates and evaporates. Most of the lower Paleozoic units pinch out rapidly against AL Qaraqaf arch to the south in addition to their being cut off by several unconformities. These unconformities represent different erosions during early and late Paleozoic and Mesozoic times.

Large ENE-WSW trending compressional faults and folds were associated with the early Alpine progeny which were later modified with smaller N-S and NW-SE normal faults.

Where; ENE – East North East and WSW – West South West

### 2.1. Well Location and Prospective Horizons

Based on correlation with the nearby wells, the following are the expected stratigraphic, table (1) shows tops of the interested zones in V8 –NC8 well.

**Table 1** shows tops of the interested zones in V8 –NC8 well.

Lower Devonian	<b>-2950 Ft</b>
Do-Sandstone	- 2950 Ft.
Do-Shale	- 2969 Ft.
D1-Sandstone	- 2917 Ft.
D1 –Shale	- 3000 Ft
D2 –Sandstone	- 3019 Ft.
D2 –Shale	- 3065 Ft.
D3-Sandstone	- 3083 Ft.
Total Depth	<b>- 3250 Ft.</b>

## 3. Theory and Calculation

In this section we will show the calculation of each parameter we did use in our research and we have used real logs to interpret the data to come out with these results.

**3.1. Volumetric Method:**

The volumetric method requires the exactest possible data on :

- a) The thickness of the reservoir rock.
- b) Its extension.
- c) Its porosity and
- d) its saturation.

By a multiplication of these 4 factors we then get the original reserves in the field under reservoir conditions as in equation (1). The thickness of the pay horizon is usually obtained from downhole measurements (SP, resistance). As only the net thickness is measured

$$N = \frac{7758 * A * h * \phi * (1 - S_{wi})}{B_{oi}}$$

Where; N= Oil in place STB, A= Productive area Ft<sup>2</sup> , h= net thickness Ft,  $\phi$ = porosity %  
 Swi= connate water saturation %, Boi = Formation Volume Factor Rb/STB.

**3.2. Volumetric Reserve Calculation:**

**3.2.1 Thickness (h):**

The gross net pay thickness has been estimated from logs.

**3.2.2 Calculation of the bulk volume of the reservoir by using ISOPACH MAP:**

A net Isopach map is a map showing lines connecting points of equal net formation thickness. The bulk volume of the reservoir has been determined by using these maps. The Trapezoidal equation has been used to determine the volume of the production zones from planimeter reading.

**A) Trapezoidal Equation:**

$$\Delta VB_n = h/2(A_{n-1} - A_n) \dots\dots\dots(1)$$

This equation used when

$$\frac{A_n}{A_{n-1}} \geq 0.5$$

**3.2.3 Porosity ( $\phi$ ):**

It is generally measured directly in the laboratory from cores or cutting and then plotted in a porosity profile these measurements are usually verified by various downhole measurements. In this paper we did use an Arche's equation to calculate the average porosity of multi strata reservoir.

$$\phi_{avg} = \frac{\sum h * \phi}{\sum h} \dots\dots\dots(2)$$

**3.2.4 Water saturation (SW):**



It is major factor the irreducible water saturation  $S_{wi}$  is best established by capillary pressure measurements carried out on cores or cutting in addition to this the (archie) formula is also useful in this respect an exact determination of the oil/water contact is usually difficult and requires experience.

**a. Calculation of water saturation (SW) from SP log**

The fluid saturation of a rock is the ratio of the volume of the fluid within the pores of the rock to the total pore volume. In this paper the water saturation has been calculated within two different methods; chart method and ARP'S equation method.

To estimate the water saturation of the formation must determine the  $R_o$  ,  $R_t$  and  $R_w$

Where

$R_o$ : oil resistivity ,  $R_t$ : true resistivity,  $R_w$ : water resistivity &  $F$ : formation resistivity factor

**ARP'S equation method:**

Compute the constant  $K$

$$K = (60 + 1.33Tf) \dots\dots\dots (3)$$

Where  $K$  : a termal convention constant.

Solve for  $R_{weq}$

$$R_{weq} = R_{mf} / 10^{(-sp/k)} \dots\dots\dots (4)$$

Convert  $R_{weq}$  to  $R_w$

If  $R_{weq} < 0.12$  then use

$$R_w = (77R_{weq} + 5/146 - (377R_{weq})) \dots\dots\dots (5)$$

If  $R_{weq} > 0.12$  then use

Where;  $R_{weq}$  : Equivalent resistivity of the formation water ,  $R_{mf}$  : Resistivity of the mud filtrate and  $SSP$  : static SP the maximum deflection possible for a given  $R_{mf}/R_w$ .

$$R_w = -0.58 + 10^{(0.69R_{weq} - 0.24)} \dots\dots\dots (6)$$

$$SW = \sqrt{(R_o / R_t)}$$

$$F = R_o / R_w$$

$$R_o = F R_w$$

$$S_w = \sqrt{(F R_w / R_t)} \dots\dots\dots (7)$$

**b. Formation factor (F):**

Archer experimentally determined that the formation factor could be determined from the porosity cementation ( $m$ ) and rock texture ( $a$ )

$$\text{Thus } F = a / \phi^m \dots\dots\dots (8)$$

Though extensive use of the relationship the following values have been used with great success

$$F = \frac{R_o}{R_w} = \frac{\text{resistivity of rock saturated with fluid}}{\text{resistivity of the saturating fluid}}$$

Where ;  $R_m$ : Resistivity of the mud ,  $R_{mf}$  : Resistivity of the mud filtrate,  $R_{mc}$  - Resistivity of the mud cake, and  $F$ : Formation resistivity factor

#### 4. Results and Discussion

##### 4.1. Estimate the total volume of the reservoir from the Isopach map:

The figure (1) is an isopach map of V-NC6 area that we used to calculate the volume of the reservoir. Table 2 shows the results of reservoir volume calculations.

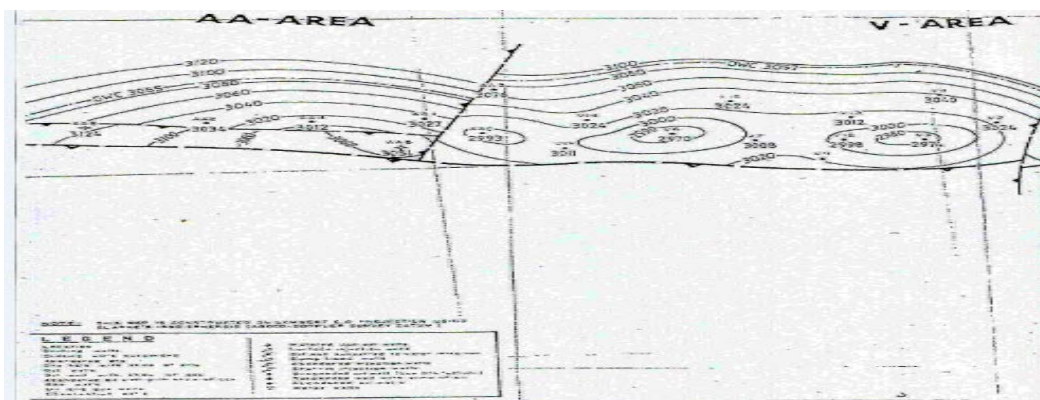


Figure (1) an isopach map of V-NC6 area of Alhamada Alhamra oil field.

Table 2 shows the results of reservoir volume calculations

Area	A (Cm <sup>2</sup> )	A (Acre)	A <sub>n</sub> /A <sub>n-1</sub>	Method Used	ΔVP( acre.ft)
A <sub>0</sub>	13.77	851.123	-	-	-
A <sub>1</sub>	9.31	575.137	0.6757	Trapezoidal	3565.65
A <sub>2</sub>	5.76	355.831	0.6186	Trapezoidal	2327.42
A <sub>3</sub>	3.11	192.124	0.5399	Trapezoidal	1369.88
A <sub>4</sub>	1.7	105.019	0.5466	Trapezoidal	742.85
A <sub>5</sub>	0.975	60.232	0.5735	Trapezoidal	330.502

Total net pore volume (ΔVP) = 8336.302 acre.ft

##### 4.2. Estimate the porosity of the reservoir from the well logging:

As example to calculate the porosity from well logging we estimated it from well V8. The figures 2 & 3 show the well head logs and the SP & Electrical logs of the well V8- NC6, respectively. Table 3 shows the results of the net pay thickness and porosity for each horizon of well V8.



In addition, when we applied this equation for all the wells in the reservoir, we will estimate the average porosity of the reservoir. Table 4 shows the calculation and results of the average reservoir porosity of V-NC6 area.

**Table 4** shows the calculation and results of the average reservoir porosity of V-NC6 area.

Well	Layer	H net (Ft.)	$\emptyset$ %	H* $\emptyset$
V2	D <sub>0</sub>	11	0.132	1.452
	D <sub>1</sub>	10	0.125	1.25
	D <sub>2</sub>	16	0.147	2.352
	D <sub>3</sub>	26	0.131	3.406
V4	D <sub>0</sub>	14	0.15	2.1
	D <sub>1</sub>	18	0.139	2.5
	D <sub>2</sub>	32	0.15	4.8
	D <sub>3</sub>	20	0.146	2.92
V6	D <sub>0</sub>	0	0	0
	D <sub>1</sub>	29	0.13	3.8
	D <sub>2</sub>	16	0.123	1.9
	D <sub>3</sub>	32	0.14	4.55
V7	D <sub>0</sub>	0	0	0
	D <sub>1</sub>	17	0.13	2.21
	D <sub>2</sub>	29	0.154	4.54
	D <sub>3</sub>	15	0.164	2.46
V9	D <sub>0</sub>	10	0.253	2.53
	D <sub>1</sub>	9	0.141	1.26
	D <sub>2</sub>	51	0.144	7.344
	D <sub>3</sub>	13	0.153	1.989
V13	D <sub>0</sub>	0	0	0
	D <sub>1</sub>	16	0.088	1.45
	D <sub>2</sub>	18	0.142	2.55
	D <sub>3</sub>	0	0	0
V14	D <sub>0</sub>	3	0.144	0.432
	D <sub>1</sub>	9	0.135	1.215
	D <sub>2</sub>	29	0.133	3.79
	D <sub>3</sub>	22	0.137	3.014
V15	D <sub>0</sub>	0	0	0
	D <sub>1</sub>	30	0.148	4.514
	D <sub>2</sub>	0	0	0
	D <sub>3</sub>	0	0	0
V18	D <sub>0</sub>	12	0.152	1.748
	D <sub>1</sub>	21	0.095	1.995
	D <sub>2</sub>	0	0	0
	D <sub>3</sub>	0	0	0
$\Sigma$		630		89.729

$$\begin{aligned}\sum H * \phi &= 89.729 \\ \sum H &= 630.5\end{aligned}$$

The average reservoir porosity is 0.1423

**4.3. Estimate the water saturation (Sw) from the well logging:**

As example to estimate (Sw) from well logging we will estimate it from well V8:

Firstly we must find the value of (Rt) and (Rw)

- Rt from reading of the log =17.5 ohms mm
- Estimate of Rt

**i. Rw with chart method at:**

TD = 3250 ft , BHT =158 F, Tavg = 68 F & Rmf = 1.17 Ohm mm @ 68. The geothermal gradient = 2.769 F degree/ 100 feet. °F(from log head)andgeothermalgradient = 2.769°F/100ft

The chart (4) has been used to estimate the formation temperature, Tf. From chart (4) Tf=130 F

The chart (5) has been used to estimate the mud and mud filtrate resistivities.

From chart (5) Rmf@130 F = 0.6 Ohm mm°F = 0.6Ohmmm

The chart (6) has been used to estimate the equivalent mud filtrate resistivity

From chart (6) Rmfeq= 0.375 Ohm mm

The chart (7) has been used to estimate the equivalent water resistivity.

From chart (7) and at SP = -70 milvolts (from log)

Rweq = 0.046 Ohm mm

From chart (6) Rw =0.062 Ohm mm

**ii. Rw with ARP'S equation at :**

Tavg =68 F, BHT =158 F, Df = 2950 ft & Dt = 3250 ft

R1 – 1.17 @68 F and SP= -70 milvolts (from log) °FandSP = -70milvolts(fromlog) and T2=149.7 °F

R2 (New Rmf); R2=0.5591 Ohm mm, thus (New Rmf) R2>0.1



And by applied the Arch,s equation for all the wells in the reservoir, we will estimate the average water saturation of it. Table 5 shows the application of Arch's equation for all wells on V-NC6 area.

**Table 5** shows the application of Arch's equation for all wells on V-NC6 area.

Well	Layer	H net (Ft.)	$\bar{\phi}$ %	Sw %	$H^* \bar{\phi}^* S_w$
V2	D <sub>0</sub>	11	0.132	0.201	0.2918
	D <sub>1</sub>	10	0.125	0.208	0.26
	D <sub>2</sub>	16	0.147	0.279	0.656
	D <sub>3</sub>	26	0.131	0.303	1.032
V4	D <sub>0</sub>	14	0.15	0.19	0.399
	D <sub>1</sub>	18	0.139	0.228	0.57
	D <sub>2</sub>	32	0.15	0.193	0.94
	D <sub>3</sub>	20	0.146	0.36	1.051
V6	D <sub>0</sub>	0	0	0	0
	D <sub>1</sub>	29	0.13	0.494	1.894
	D <sub>2</sub>	16	0.123	0.596	1.172
	D <sub>3</sub>	32	0.14	0.429	1.951
V7	D <sub>0</sub>	0	0	0	0
	D <sub>1</sub>	17	0.13	0.251	0.544
	D <sub>2</sub>	29	0.154	0.372	0.168
	D <sub>3</sub>	15	0.164	0.377	0.927
V9	D <sub>0</sub>	10	0.253	0.399	1.009
	D <sub>1</sub>	9	0.141	0.474	0.601
	D <sub>2</sub>	51	0.144	0.303	2.225
	D <sub>3</sub>	13	0.153	0.299	0.594
V13	D <sub>0</sub>	0	0	0	0
	D <sub>1</sub>	16	0.088	0.371	0.538
	D <sub>2</sub>	18	0.142	0.278	0.710
	D <sub>3</sub>	0	0	0	0
V14	D <sub>0</sub>	3	0.144	0.614	0.2652
	D <sub>1</sub>	9	0.135	0.188	0.22842
	D <sub>2</sub>	29	0.133	0.274	1.038
	D <sub>3</sub>	22	0.137	0.381	1.1483
V15	D <sub>0</sub>	0	0	0	0
	D <sub>1</sub>	30	0.148	0.238	1.0743

	D <sub>2</sub>	0	0	0	0
	D <sub>3</sub>	0	0	0	0
V18	D <sub>0</sub>	12	0.152	0.409	0.7149
	D <sub>1</sub>	21	0.095	1.097	1.09725
	D <sub>2</sub>	0	0	0	0
	D <sub>3</sub>	0	0	0	0
Σ		630			26.93079

$$\sum H * \phi = 89.729 \text{ \& } \sum H * \phi * S_w = 26.93079$$

#### 4.4. Estimate the Original Oil in Place (OOIP) with Volumetric Equation:

$\Delta BV = 8336.3$  acre ft., porosity of the reservoir = 0.142314 , average water saturation of the reservoir = 0.300137 and the oil formation volume factor ( $B_{oi}$ ) = 1.165

$$OOIP = 5.43924 * 10^6 \text{ STB}$$

## 5. Conclusions and Recommendations

From drilling, testing and logging results, it is concluded that V8-NC6 well proved to be one of the best oil wells in Elhamada Alhamra oil field in the “V” structure. The gross thickness of the pay zone attains 154` while the net oil sands attains about 105`. On top of the pay zone “Lower Devonian Sandstone”. The D<sub>0</sub> Sandstone was net at 2971` leveled with V6-NC6 well. The D<sub>2</sub> Sandstone was proved the thickness in the area since it attains 53` in the well V8 while its thickness is 40` in V6. It was decided to start production from D<sub>3</sub> sandstone at first through the perforated interval 5151`-5159` and left the other zones for future planning. It was recommended to drill a development well between the eastern and western culmination of the “V” structure I.e. between V7 and V8-NC6 wells to check the oil water contact in the D<sub>2</sub> sandstone unit.

### Acknowledgment

We do thank the Arabian Gulf Oil Company for their help and support in providing the required data for this paper, as well as our staff member of Sirte University.

### References

- [1]. Pletcher, J.L., 2002. Improvements to Reservoir Material-Balance Methods. SPE, pp. 49–59
- [2]. Konak, A., David, Coit, W., Alice, Smith, E., 2006. Multi-objective optimization using genetic algorithms: a tutorial. Reliab Eng Syst Saf 91 (No. 9), 992–1007.

- [3]. Schulze, R.W., Riegret, Axmann, J.K., Hease, O., Rian, D.T., You, Y.L., 2002. *Evaluationary algorithms applied to history matching of complex reservoirs*. SPE Reser Evalu Eng 5 (2), 163–175.
- [4]. Donald P. Helander – *Fundamentals of Formation Evaluation*. Copyrights © 1983 Tulsa, Oklahoma.
- [5]. Alfred Mayer. *Gurr–Petroleum Engineering* © Ferdinand Enke publishers Stuttgart 1976.
- [6]. Craft and Hawkins- *Applied Petroleum Reservoir Engineering*, Louisiana State University 1959.
- [7]. M.J. Salem & Hammuda - *Gelogy of Libya* Volumes I & II, copyright © 1991 by Tripoli University, Tripoli.

## Boilers Performance Evaluation of Zuara Desalination Plant

Ali K. Muftah<sup>1\*</sup>, Mabruk M. Abugderah<sup>2</sup>, Hakem S. Dakhel<sup>3</sup>

1ali.alkhtabe@yahoo.com, 2mabruk21@hotmail.com, 3hakeem\_sasy@yahoo.com

<sup>1,3</sup>Department of Mechanical Engineering, College of Engineering, Sabratah University, Libya

<sup>2</sup>Research and Consultation Centre, Sabratah University, Sabratah, Libya

### ABSTRACT

Water is the basis of daily life and industrial development for all communities. Water desalination plants emerged as one of the most important alternatives to overcome the shortage of water resources especially in desertified countries like Libya. Boilers are the main part in thermal desalination plants which depends on steam as the working fluid to heat and evaporate the seawater. with a capacity of 80 tons/hr of superheated steam at 220°C and 15bar. Due to operating conditions, there was a decrease in steam boilers productivity and low efficiency. Heavy black smoke in chimneys was also detected. This work investigates the performance of the above mentioned boilers to determine the actual causes of these negative results by comparing the design values with different operating readings data. The results show a decrease in the efficiency of the boilers for low loading rates, which is affected by the air/fuel ratio. The deviation of this ratio from the design values leads to low efficiency and the emergence of heavy smoke in the chimneys, which causes deposits on the boiler pipes reducing the effectiveness of heat exchanger and therefore the thermal efficiency. The study also shows that the long operation suspension of the boilers in the first years of its life, due to the lack of discharge network and electricity cutoffs resulted in bad effect on the pipes conditions. The last led to the pipes deterioration resulting in water leaks and thus low boilers evaporation rates.

**Keyword**— desalination; boiler; thermal efficiency; air/fuel ratio.

### 1. Introduction

Water is the source of life used on in houses, agriculture, industry...etc. The lack and contamination of existing potable water resources led to desalination emergence as an important alternative resource to make up the shortage of demand especially in the countries that suffer from dryness. In general, there are two main types of seawater desalination technology one is the thermal or phase change processes and the other is membrane or processes without phase change. Desalination thermal processes are mostly found in countries, where fuel is quite cheap. Steam is used as the working fluid in desalination thermal type. The steam can be supplied by exhausting or bleeding steam turbines, or directly from boilers. The last one has an advantage of offering the steam with the required quality and quantity.

Performance evaluation is one of the essential requirements for the conservation of energy and optimization of operating parameters of boilers. There are many studies and researches in the field of performance evaluation of boilers contributed lifting of efficient production in many factories, desalination and power

plants. As per the study carried out by Pachaiyappan [1] entitled improving the boiler efficiency by optimizing the combustion air, in which the performance of the air preheater has been studied on the basis of the combustion air passing through it. The author concluded that the correct optimization of the combustion air can increase the boiler efficiency by 2-3%, and also ensures less fuel consumption. By reducing the air preheater leakage, the auxiliary power consumption is also reduced. Thus the fuel is saved which leads to a considerable amount of profit.

Bora1 and Nakkeeran [2] presented an article about the performance analysis from the efficiency estimation of coal fired boiler. This paper puts forward an effective methodology for the efficiency estimation of a coal fired boiler, in comparison with its design value and enlists some of the factors that affect the performance of a boiler and it will help to increase overall boiler efficiency and as a result, annual monetary savings of the thermal power plant.

Improvement of boiler's efficiency using heat recovery and automatic combustion control system was studied by Suntivarakorna and Treedetb [3]. This research was conducted to improve the efficiency of a fire tube boiler with a fixed gate and screw conveyor for feeding fuel, the experimental result indicated that using heat recovery and fuel drying reduces by 3%wt of fuel moisture content and boiler efficiency increases by 0.41%.

As per the study carried out by Baladhiya and Doshi [4], performance evaluation and optimization of steam generating systems. The automatic controls used in modern boilers have improved the efficiency of the boiler by optimizing operating parameters required for efficient combustion process and to achieve safety in operation of fuels. Operation of boiler under optimum conditions not only helps in reducing the cost of steam generation but also helps in reducing the air pollution.

Lahijani and Supeni [5] presented a work about the evaluation of the effect of economizer on efficiency of the fire tube steam boiler. The results show the effect of using an economizer increases the feed water temperature and improves the efficiency of fire tube steam boiler.

Zuara multi effect type (MED) desalination plant is a thermal type. The first stage of the plant contains three water pipes for the boilers, with a capacity of 80 tons/hr. The produced steam has a temperature of 220°C and pressure of 15 bar. The plant was inaugurated in the beginning of 2006. At this stage the boilers thermal efficiency have exceeded 92%. Over time, due to the operating conditions of the plant, there was a decrease in steam boiler productivity and low efficiency.

The objective of this study is to compare the operation real reading data of boilers in the plant with the design values confirmed by the performance tests and detect the reasons behind the low efficiency and productivity of the plant.

## 2. Materials And Methods

Two types of boilers data were collected. The design data was taken from plant documents and the actual operating data (real time data) was taken from the control room of Zuara desalination plant. It is available as

daily and shifts reports from the first unit start up until the last boiler shutdown. The operating reading data selected along the boilers operating life cycle with different load rates. Table (1) presents sample of design and readings data for the boiler unit1 [6].

**Table 1:** Design and real data for different annual operating periods of boiler unit 1.

Item	Unit	Design value	Annual real data				
			2007	2009	2011	2013	2014
Feed water flow rate	t/h	80.000	68.049	72.211	75.684	72.738	70.708
Feed water temperature	°C	115.00	112.96	113.07	113.08	113.07	112.96
F.W temp. after economizer	°C	165.00	165.33	174.38	176.64	173.39	149.94
Fuel mass flow rate	kg/h	4485.2	4221.8	4595.4	4732.0	4607.5	4411.8
Boiler steam product	t/h	80.000	67.598	71.040	74.342	70.003	58.035
Steam pressure	Bar	16.00	15.00	15.03	15.00	15.08	14.79
Steam temperature	°C	233.00	219.51	219.92	222.25	221.88	220.79
Air mass flow rate	t/h	76.845	72.896	69.379	81.565	84.315	81.677
Eco. Inlet gases temp.	°C	355.00	340.92	380.64	413.54	404.9	389.67
Stack temperature	°C	150.00	159.11	177.68	185.09	194.88	169.48
Boiler operating hours/year	hr	---	2093	2857	6103	6506	4502

### 3. Theory and Calculation

The performance evaluation parameters of boiler, like efficiency and evaporation ratio are reduced with time due to poor combustion, as well as the heat transfer surface fouling and poor operating and maintenance conditions. Even for new boilers, some reasons such as fuel and water quality can result in poor boiler performance. Boiler efficiency tests are helpful in finding the deviation of boiler efficiency from the best or design efficiency and target problem area for corrective action. Several indicators must be identified that affect the boiler efficiency and also help to determine the reasons behind the deviation.

#### 3.1. Boiler Efficiency $\eta_B$ :

The efficiency of any equipment is generally defined as the percentage of net energy obtained from the equipment to the total energy given to the machine, regardless of the type of the energy, mechanical, thermal or chemical. There are two methods to calculate the boiler efficiency, for direct and indirect methods. The direct method which is used in this study is easy to apply and does not require many complicated devices. The method is summarized as follows [7]:

$$\eta_{Boiler} = \frac{\dot{m}_s(h_e - h_i)}{\dot{m}_f * HV} \quad (1)$$

### 3.2. Boiler Evaporation Rate(B.E.R):

It is the ratio between the steam produced from the boiler and the fuel consumption, i.e. the number of kilograms of steam obtained when burning one kilogram of fuel, which expresses the performance of the boiler without paying attention to the type and quality of the steam produced or type of fuel consumed [8].

$$B. E. R = \frac{\dot{m}_s}{\dot{m}_f} \quad (2)$$

### 3.3. Air Fuel Ratio (A/F):

The normal way to control excess air volume (Air/Fuel ratio) is by measuring the content of the exhaust gas from the oxygen and adjusting the ratio between fuel and air to achieve the maximum air level as low as possible, while maintaining complete combustion [8].

$$A/F = \frac{\dot{m}_a}{\dot{m}_f} \quad (3)$$

### 3.4. Economizer Effectiveness $\epsilon$ :

The economizer is a heat exchanger used to heat feed water before entering the boiler. It can also be used to heat the combustion air. The effectiveness of the economizer is defined as the ratio of the actual heat transfer rate to the maximum possible heat transfer rate. It can be expressed as: [8]

$$\epsilon_{Economizer} = \frac{q}{q_{max}} \quad (4)$$

$$q = \dot{m}_w C p_w (T_{co} - T_{ci}) \quad (5)$$

$$q_{max} = C_{min} (T_{hi} - T_{ci}) \quad (6)$$

## 4. Results And Discussion

The required results were obtained by substituting the boiler operational data in the previous mathematical relationships. Some important assumptions should be taken in consideration to facilitate the access the results.

- The heating value of the heavy fuel used in the plant is constant and equal to 44084kJ/kg.K [6].
- The thermal heat capacity of feed water is constant and equal to 4.186kJ/kg.K [8]
- The thermal heat capacity of gases combustion is constant and equal to 1.17kJ/kg.K [6]

Tables (2),(3)and (4) show the most important results obtained for the three boilers.

**Table 2:** Performance indicators for boiler unit 1.

Performance indicators	Design value	Results from real data				
		2007	2009	2011	2013	2014
Boiler Load %	100.00	84.50	88.80	92.93	87.50	72.54
Boiler thermal efficiency %	92.32	86.20	83.21	84.57	81.78	70.96
Boiler evaporation rate	17.00	16.01	15.46	15.71	15.19	13.15
Air fuel ratio (A/F)	16.75	17.27	15.10	17.24	18.30	18.51
Economizer effectiveness%	85.42	79.76	75.85	76.03	71.97	79.57

**Table 3:** Performance indicators for boiler unit 2.

Performance indicators	Design value	Results from real data				
		2007	2009	2011	2013	2014
Boiler Load %	100.00	74.79	90.75	94.04	82.79	79.50
Boiler thermal efficiency %	92.32	88.04	85.41	83.90	81.42	74.93
Boiler evaporation rate	17.00	16.35	15.87	15.59	15.13	13.89
Air fuel ratio (A/F)	16.75	16.95	15.32	16.27	19.06	16.98
Economizer effectiveness%	85.42	85.55	71.58	70.65	74.38	77.03

**Table 4:** Performance indicators for boiler unit 3.

Performance indicators	Design value	Results from real data				
		2007	2009	2011	2013	2014
Boiler Load %	100.00	77.11	89.65	87.39	88.56	80.23
Boiler thermal efficiency %	92.32	84.86	82.46	81.56	81.13	75.69
Boiler evaporation rate	17.00	15.76	15.32	15.15	15.07	14.03
Air fuel ratio (A/F)	16.75	16.16	16.92	16.22	16.86	17.52
Economizer effectiveness%	85.42	84.79	76.81	72.64	74.71	72.90

Tables (2),(3) and (4) present the performance indicators for boilers units 1,2 and 3 respectively. It can be seen that the thermal efficiency of the boilers is directly proportional to the boiler load rate. The evaporation rates are also increased by increasing the boilers loads. Figure(1) shows the affect of the loads on the boilers thermal efficiency. It is also clear that the plant in its first years of operation has not been operating with high productivity. This is also evident from the total number of boilers operating hours due to the absence of an

integrated water network linking the desalination plant to the consumption areas. During this period only one boiler was operated. Even though the other boilers were periodically operated this act resulted in the deterioration of their state.

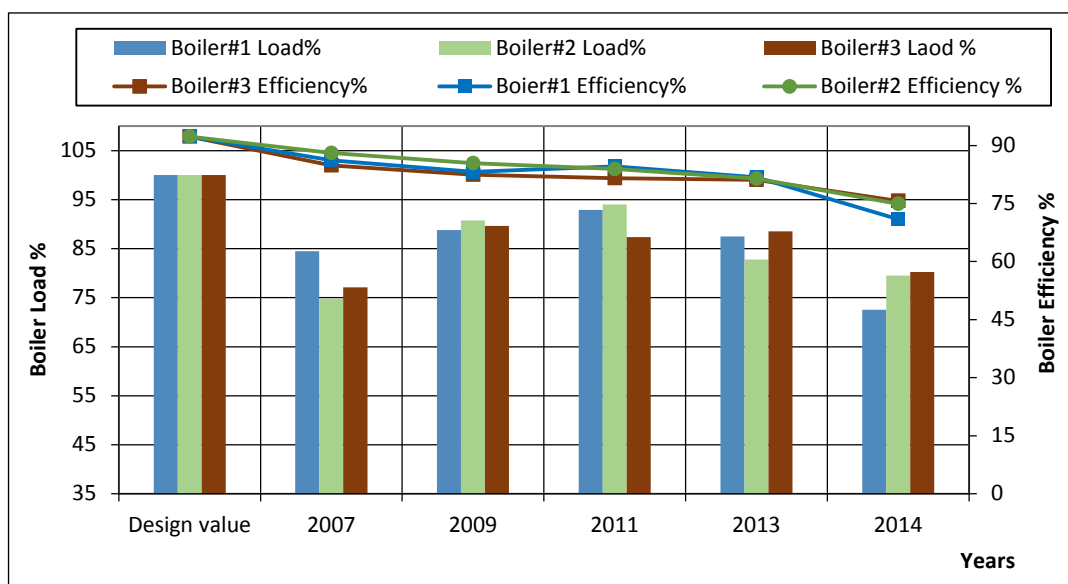


**Figure1:** Effect of boiler loads on boilers thermal efficiencies

The previous tables also show that the air/fuel ratio is unstable and variable in a random manner and certainly affects combustion rates. The deviation of this ratio from the design values leads to low efficiency and the emergence of heavy smoke in the chimneys, which causes deposits on the boiler pipes reducing the effectiveness of heat exchanger and the thermal efficiency especially in recent years of boilers age.

Figure (2) shows the air/fuel ratio and economizer effectiveness. The random change in the air/fuel ratio affects the combustion efficiency. The increase of air ensures complete combustion, but causes a loss of part of the thermal energy with the excess air in combustion gases. On the other hand, the lack of air quantity leads to incomplete combustion and therefore the emergence of thick black smoke in chimneys and increase the amount of this smoke, which causes the accumulation and crust on the pipes in the economizer and consequently, results in the low effectiveness of the economizer as well as a key factor in the corrosion of pipes and water leakage inside the boiler. The last was noticed through the water mass balance compared to the feed water and produced steam. This phenomenon was observed during the last years of operation of the boilers.

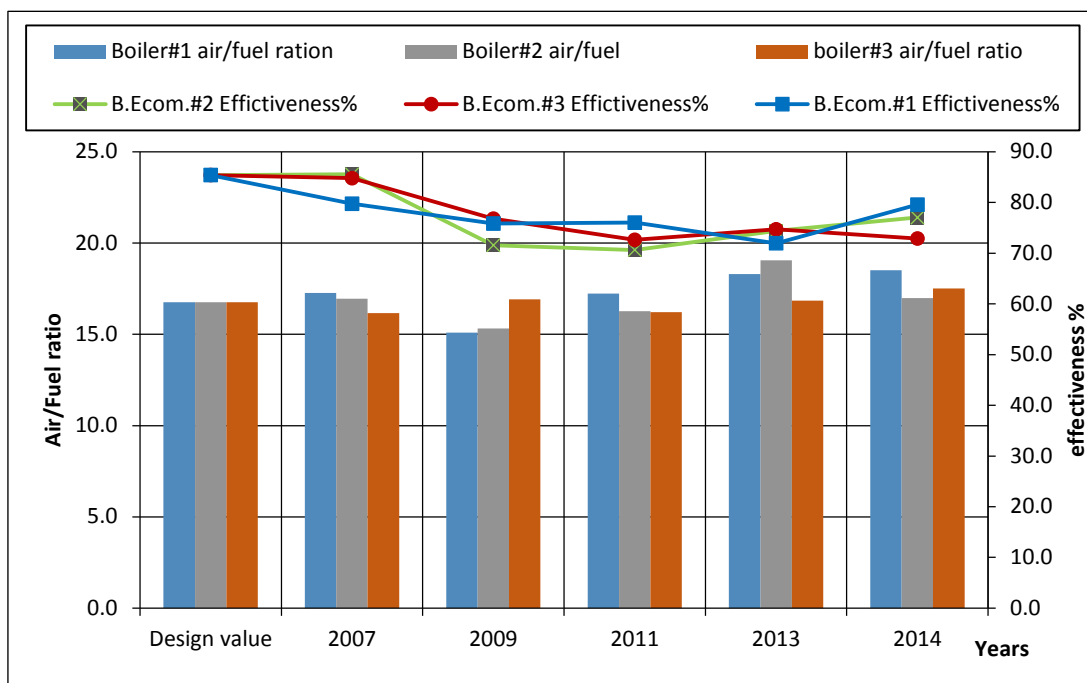


Figure 2: Air/fuel ratio and economizer effectiveness.

## 5. Conclusions

The boiler efficiency can be reduced by many factors. Zuara desalination boilers were exposed in the first years to long suspension period due to the absence of a network of transmission and distribution of water produced in the plant, as well as the sudden stops and frequent eruptions due to power outages in recent years. The previous problems have negative impact on the productivity of steam boilers and its efficiency and cause the corrosion for most of its parts and this lead to water leakage in the pipes. The poor mixing ratio of the air-to-fuel is a major cause of the black smoke of boilers, which due to its abundance and difficulty of disposal has affected the efficiency of the economizer and thus the performance of the boiler, So it is recommended to modify the combustion air rate of fuel in a correct ratio according to the design values as well as the use of the system of the boiler soot blower periodically and regularly according to manufactures company procedure.

## Acknowledgment

We would like to express our sincere thanks toward Zuara Desalination Plant engineers and staff for their valuable support in the implementation of this project.

## References

- [1]. R. Pachaiyappan and J. Prakash, "Improving the Boiler Efficiency by Optimizing the Combustion Air", Vol.787, pp. 238-242, Access online on 24 June 2018 at <https://doi.org/10.4028/www.scientific.net/AMM78.238>
- [2]. M. Bora1 and S. Nakkeeran " Performance Analysis From The Efficiency Estimation of Coal Fired Boiler",Vol.2,pp561-574, Access online on 24 June 2018 at [http://www.journalijar.com/uploads/901\\_IJAR-3240](http://www.journalijar.com/uploads/901_IJAR-3240)
- [3]. R. Suntivarakorand W. Treedetb "Improvement of Boiler's Efficiency Using Heat Recovery and Automatic Combustion Control System", Vol.100, pp.193-197, 2016. Access online on 26 June 2018 at <https://doi.org/10.1016/j.egypro.2016.10.164>
- [4]. Baladhiya, C. S. ; Doshi, J. S."Performance evaluation and optimization of steam generating systems",Vol.10 No.1 pp.222-227, Access online on 27 June 2018 at :<http://www.researchjournal.co.in/onli..>
- [5]. Ahmad M. Lahijani and Eris E. Supeni "*Evaluating the Effect of Economizer on Efficiency of the Fire Tube Steam Boiler*",Vol.07.1 pp1-4, Access online on 02 July 2018 at <https://www.researchgate.net/publication/324196534>
- [6]. Manuals and performance test sheets for boilers of Zuara desalination plant, designed and constructed by SIDEM company 2005.
- [7]. Amit Kumar Jain, "An Approach towards Efficient Operation of Boilers," *International Journal of Scientific & Engineering Research*, Vol. 3, pp 01-11 , Access online on 10 July 2018 at. <https://pdfs.semanticscholar.org/70f1>.
- [8]. Yunus A. Cengel and Michael A. Boles, "Thermodynamics An Engineering Approach", Eight Edition. ISBN 978-0-07-339817-4
- [9]. Frank P. Incropera, "Introduction to heat transfer", Sixth Edition ISBN 13 978-0470-50196-2

# Estimation of Original Oil in Place for Belhedan Oil Field by Using Volumetric Method, Material Balance Equation Method, and Reservoir Simulation Method

Ali Omran Nasar<sup>1</sup>, Jibriel Abusaleem<sup>2</sup>, Essa M. Tabar<sup>3</sup>

<sup>1</sup> ali\_omran95@yahoo.com, <sup>2</sup> jabusaleem@su.edu.ly, <sup>3</sup> etabare4@gmail.com<sup>3</sup>

<sup>1,2,3</sup> Department of Petroleum, College of Engineering, Sirte University, Libya

## ABSTRACT

Knowing the amount of the hydrocarbon pore volume correctly is basically required to have properly design of oil and gas reservoirs. The accuracy in calculating of the hydrocarbon pore volume depends on the used method. Usually two conventional methods use to estimate the Original Oil In Place (OOIP) very quickly. These two methods are volumetric method and Material-Balance-Equation (MBE) method. However, there is another quick method that can be used to calculate (OOIP) which is reservoir simulation method. In this paper, three difference methods were used to calculate OOIP to provide Waha Oil Company with the calculated value.

Moreover, each method required sort of data; the volumetric method depends on static data. However MBE and reservoir simulation method require dynamic data of the reservoir and the area around. Usually the driving mechanism is the key point when MBE and reservoir simulation are used. The drive mechanism in studied area (Belhedan oil field) is described from the field information as a strong water drive with small gas-cap. The given field data don't have any information about the gas cap and the water dive. As a result, applying the MBE method to calculate OOIP for this case require some information about the gas cap and the aquifer. So the MBE gave a value of OOIP didn't agree with the value of OOIP that obtained from the volumetric and reservoir simulation. Lack in the information makes MBE unusable method in this case. It has been trying to solve this problem by use some correlation in calculate some parameters and ignore others. However, doing all that, the result couldn't reach any closed value that is calculated by volumetric and reservoir simulation which will explain. In the end of the paper, a prediction of well performance (well v-4) will be done from 1970 until 2020.

**Keyword**— Original Oil In Place, Volumetric Estimation, Material-Balance-Equation (MBE), and Reservoir Simulation Model.

## 1. Introduction

Knowing the amount of original oil in place is the most important parameter for reservoir engineers to make a quick decision whether the discovered area is profitable or not. There are two conventional methods and two unconventional methods use to calculate the OOIP. The two conventional methods are volumetric method and Material-Balance-Equation (MBE) method, and the two unconventional methods are reservoir

simulation method and decline curve analysis method<sup>(1)</sup>. In reservoir engineer's perspective, the most used methods in petroleum industry are volumetric method and reservoir simulation method. This is because, they are more sophisticated than the other methods to calculate OOIP. The volumetric is quick method and reservoir simulation is more accurate, for these reasons one of them usually is chosen. Among the mentioned methods this paper will focus on volumetric, MBE, and reservoir simulation.

The volumetric depends on basic data of reservoir rock and reservoir fluid properties. However, the reservoir simulation needs a lot of information starts with geological history and ends with production history additional to reservoir rock and fluid properties<sup>(1)</sup>. On the other hand, MBE depends on combinations of fluid properties, rock properties, and production data. Since each method required different sort of data the result will be different, but which one is better this will be discussed. Moreover, each method has some advantages and disadvantages. First, volumetric is a simple method and doesn't require a lot of information; however it is limitations the reservoir heterogeneity where the reservoir assumed is a homogenous and not accurate enough. Second, MBE depends on production data which usually are available and other reservoir properties can be obtained from laboratory experiments. However, it isn't proper to be use when the reservoir is connected to aquifer or gas cap with no enough information about them. The reservoir simulation is quick and accurate method in calculating OOIP. The only problem can face reservoir engineers is building reservoir model that capable to produce hydrocarbon as the real reservoir. In the end, whether the calculation of initial hydrocarbon in place is made manually (volumetric – MBE) or by computer applications (reservoir simulation), the procedures are the same in principle. The three mentioned methods will be explained briefly and individually.

### 1.1. Volumetric Method

In a new area, usually volumetric estimation made before drilling first well, where the reservoir is assumed to be exists and there is no chance of failure. The volumetric method depends on calculation of reservoir volume which obtained of geophysical maps. There are different methods use to estimate it, like dividing the reservoir into small grid bulk or dividing the area of contour maps into pisses as show in Figure below.

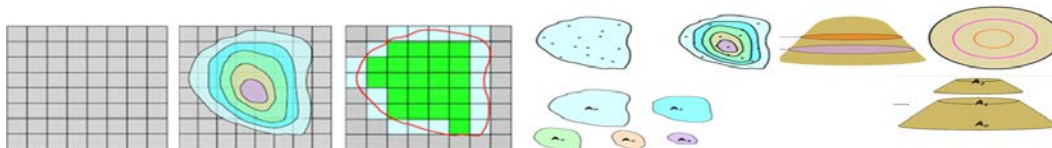


Figure 1: Methods of reservoir volume calculations<sup>(2)</sup>.

After the volume is estimated by one of the shows methods in Figure 1, it should multiple by rock porosity and fluid saturation which will result the estimation of recoverable barrels of oil or mcf of gas. In order to covert recoverable hydrocarbon (oil or gas) to standard condition, it should be divided by its formation volume factor. The equation that uses to calculate OOIP by volumetric method can be written as:

$$OOIP = \frac{7758 Ah\phi(1 - S_{wi})}{B_{oi}} \quad (1)$$

## 1.2. Material Balance Equation, MBE

Material balance equation is the second method that used in this paper to estimate OOIP. Essentially, MBE depends on analyzing of production volumes, pressure condition, and fluid properties to calculate OOIP. In order to have proper understating of MBE solution assume a tank model that located at datum depth and behave like real reservoir condition that having different condition ( reservoir pressure and fluid properties ) as shown in Figure 2 <sup>(3)</sup>. After start producing from that model, the reservoir pressure will start decrease and the oil and gas condition will change and produce new materials in the reservoir beside that some other elements will inter to the reservoir as shown in tank below.

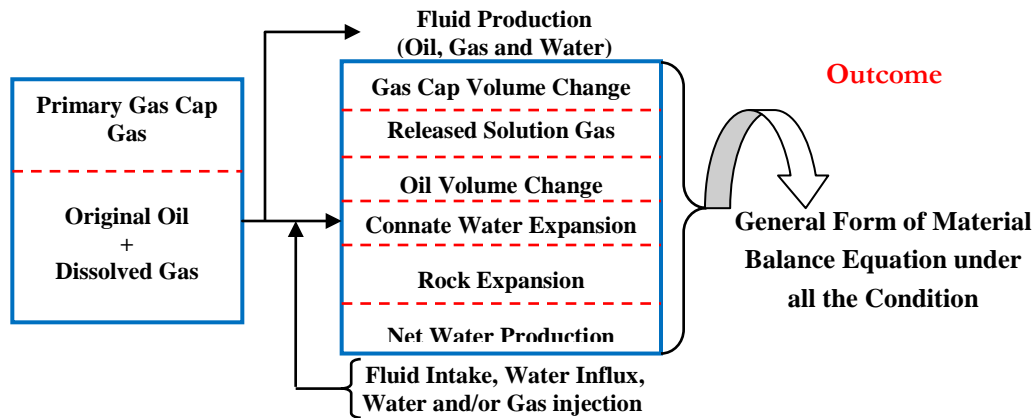


Figure 2: Tank model of reservoir under original condition and after start producing <sup>(3)</sup>.

By replacing all mentioned terminologies and combine them, the general form of the material balance equation for the tank mode of above reservoir can be written as<sup>(3)</sup>:

$$N = \frac{Np[B_o + (R_p - R_s)B_g] - (W_e - W_pB_w) - G_{inj}B_{ginj} - W_{inj}B_w}{(B_o - B_{oi}) + (R_{si} - R_s)B_g + mB_{oi} \left[ \frac{B_g}{B_{gi}} - 1 \right] + B_{oi}(1 + m) \left[ \frac{C_w S_{wi} + C_f}{1 - S_{wi}} \right] \Delta p} \quad (2)$$

The above equation is the general form MBE which uses to estimate initial hydrocarbon pore volumes, predict reservoir pressure, calculate water influx, predict future reservoir performance, and predict ultimate hydrocarbon recovery under various types of primary drive mechanisms. Furthermore, the general form of the MBE has been developed to be an equation of straight line equation for simplicity, where some elements that are not exist in the reservoir <sup>(3)</sup>. The straight-line solution method requires plotting variable group versus

another variable group. Each group depends on the driving mechanism of production in which the reservoir is producing, and it is the most important tasks. Depending on the driving mechanism the solution of MBE can be taken one of the several cases: undersaturated oil reservoir case, saturated oil reservoir case, gas cap reservoir case, water drive reservoirs case, and combination drive reservoirs case<sup>(3)</sup>. Since the driving mechanism of Belhedan oil fields is described as strong water drive with small cap gas, the solution of MBE as straight line equation should use either water drive case, or combination drive case. From field information the gas cap is very small and was neglected in any calculation, because there isn't enough information about it. In a water-drive reservoir mechanism, identifying the type of the aquifer and characterizing its properties are perhaps the most challenging tasks can face any reservoir engineers to calculate the amount of OOIP correctly. Havlena and Odeh solve the general form of MBE by rearrange the general form of MBE and ignores other for the purpose of simplicity by assuming no pressure maintenance comes from gas or water injection. The rearrangement of MBE equation can be written as <sup>(3)</sup>:

$$N_p [B_o + (R_p - R_s) B_g] - (W_e - W_p B_w) = \quad (3)$$

$$N \left[ (B_o - B_{oi}) + (R_{si} - R_s) B_g + \left[ \frac{B_g}{B_{gi}} - 1 \right] + B_{oi} (1 + m) \left[ \frac{C_w S_{wi} + C_f}{1 - S_{wi}} \right] \Delta p \right]$$

Moreover, Havlena and Odeh had simplified the above equation to be an equation of straight line equation and shortages the number of terms to have them in equation of couple groups with different names as shown below:

$$F - W_e = N(E_o + mE_g + E_{f,w}) \quad (4)$$

In equation 4, each new symbol have different name and represent different section of the reservoir which are: F represents the reservoir volume of cumulative oil and gas produced which named as the underground withdrawal.  $W_e$  refers to the net water influx that is retained in the reservoir.  $E_o$ ,  $E_g$ ,  $E_{f,w}$  these group presents the expansion of oil and its originally dissolved gas production, net expansion of the gas cap that occurs with the production, and the expansion of the initial water and the reduction in the pore volume respectively.

Havlena and Odeh in 1963 expressed an equation for undersaturated oil reservoir where  $m=0$ , and rearranging the equation 4. So the equation can be written as <sup>(4)</sup>:

$$F = N(E_o + E_{f,w}) + W_e \quad (5)$$

Havlena and Odeh had further expressed equation 5 in a more condensed form as <sup>(4)</sup>:

$$\frac{F}{E_o + E_{f,w}} = N + \frac{W_e}{E_o + E_{f,w}} \quad (6)$$

Dake in 1978 points out that the term  $E_{f,w}$  can frequently be neglected in water-drive reservoirs. This is because water influx helps to maintain the reservoir pressure. The equation 6 cannot be solved directly to

calculate the OOIP, since it is require calculating water influx first. Several water influx models can be used to calculate the water influx. One of these models is Schilthuis steady-state method, which will be use in this study. The steady-state aquifer model as proposed by Schilthuis in 1936 is given by <sup>(4)</sup>:

$$W_e = C \int_0^t (P_i - P) dt = C \sum (P_i - P) \Delta t \quad (7)$$

Combining equation 6 with 7 gives a straight line equation as shown below <sup>(4)</sup>:

$$\frac{F}{E_o + E_{f,w}} = N + C \frac{\sum (P_i - P) \Delta t}{E_o + E_{f,w}} \quad (8)$$

### 1.3. Reservoir Simulation Modelling

Usually reservoir simulation uses to find the accurate value of hydrocarbon initially in place under different conditions, and also to help reservoir engineers having a proper understanding of reservoir behaviour and making prediction which help engineers in making investment decisions. In this study, a compositional reservoir simulator has been utilized with the intention of modelling and simulating the reservoir <sup>(5)</sup>. CMG (Computer Modelling Group) is the reservoir simulation that has been used. This commercial software is used in this study to determine reservoir capacities in order to maximize potential recovery and making oil prediction.

## 2. Data of Studied Reservoir

The data that are used in this study were obtained from Waha Oil Company. Table 1 and 2 presents basic information of reservoir fluid, rock properties, and average reservoir properties for each layer, respectively. Table 3 presents PVT data. The production data versus reservoir pressure had been clean up before it use because some data doesn't have pressure records, and it start from 1965.

**Table 1:** Reservoir Data Summary as of July 2013 Belhedan - Gargaf Formation <sup>(6)</sup>:

Basic Reservoir Data		Average Rock & Fluid Properties	
1-Top of Pay Formation, ft	6300	8- Porosity , %	8.0
2- Datum Depth, ft	6500	9- Permeability, md	10-100
3- Total producible Wells	29	10- Water Saturation, %	33.0
4-Productive Acreage, acres	18600	11- Rock Compressibility, Psia-1	4.6*10 <sup>-6</sup>
5- Average Net Pay, ft	190	12- Water Compressibility, Psia-1	3.3*10 <sup>-6</sup>
6- Original BHP at Datum, Psia	3100	13-F.V.Fat Original Pressure, RB/STB	1.135
7- Reservoir Temperature, deg F	210	14- Current Reservoir Pressure, Psia	2322

**Table 2:** Gargaf Layers, Average Reservoir Properties above the Oil-Water Contact (°):

Gargaf Layer	Gross, ft	Net ft	Net/Gross	Porosity,%	Sw, %	HCPTh, ft
GL-1	39.7	27.0	0.68	8.5	37.6	1.43
GL-2	80.1	47.7	0.60	7.6	37.8	2.55
GL-3	75.6	37.6	0.50	6.7	36.3	1.97
GL-4	74.5	38.8	0.52	7.0	35.7	2.11
GL-5	52.9	27.0	0.51	6.8	38.9	1.37
GL-6	29.4	21.0	0.71	7.5	31.5	1.07

**Table 3:** PVT Data for well v42 (°):

P, Psia	V/Vs at	B <sub>od</sub> , rb/stb	R <sub>sd</sub> , scf/stb	μ <sub>od,c</sub> p	C <sub>od</sub> 1/psi	B <sub>o</sub> rb/STB	R <sub>s</sub> scf/STB
478	1.0386	1.154	122			1.123	84.3
536	1.0000	1.158	133	1.29		1.127	95.0
600	0.9994	1.157			9.38E-06	1.126	
700	0.9984	1.156		1.31	1.00E-05	1.125	
800	0.9975	1.155			9.02E-06	1.124	
900	0.9966	1.154			9.03E-06	1.123	
1000	0.9956	1.153		1.35	1.00E-05	1.122	
1200	0.9938	1.151			9.06E-06	1.120	
1400	0.9921	1.149		1.39	8.57E-06	1.118	
1700	0.9896	1.146			8.42E-06	1.115	
2000	0.9871	1.143			8.44E-06	1.112	
2300	0.9846	1.140			8.46E-06	1.109	
2600	0.9823	1.138			7.80E-06	1.107	
3000	0.9794	1.134			7.40E-06	1.103	
3500	0.9757	1.130			7.58E-06	1.099	
4000	0.9722	1.126			7.20E-06	1.096	

### 3. Results and Discussion

$f(x) = a_0 + \sum_{n=1}^{\infty} \left( a_n \cos \frac{n\pi x}{L} + b_n \sin \frac{n\pi x}{L} \right)$  The calculation of OOIP has been done by using different methods. The result of each method was compared and sent it to Waha Oil Company as it's required.

#### 3.1. First, Volumetric Method

Estimation of OOIP has traditionally been done using volumetric method. All the data need to calculate OOIP are listed in Tables 1 and 2, which include an average value of porosity, saturation, and total net pay

thickness for the six layers. Applying equation 1 the initial oil in place is calculated to be 1.29 MMMSTB as shown below.

$$OOIP = \frac{7758 Ah \phi (1 - S_{wi})}{B_{oi}} = \frac{7758 * 18600 * 190 * 0.08 * (1 - 0.33)}{1.135} = 1.294 \text{MMMSTB}$$

It is well know that the volumetric method is a quick and an easy method of calculating OOIP. However, its result isn't that accurate when it compare with other methods, but it is satisfied method which can be use to make a quick decision when its need it.

### 3.2. Second, Material Balance Equation Method, MBE

The MBE method supposes to be more accurate in the results than the volumetric method, but due to the lack of information about the aquifer around the reservoir, and changing in the reservoir pressure, the MBE mightn't be the correct choice. The reservoir pressure has been changed rapidly in increasing and decreasing. The changing in the pressure is a result of opening and closing the well as it is mentioned from the company in additional to water influx. Using MBE as straight line equation in such this case which is depending basically on the reservoir pressure and production data will led for incorrect value of OOIP. Since it's a straight line equation, which is require smooth changing of reservoir pressure. In order to calculate the OOIP by MBE as straight line equation there are two important elements must be known, these elements are; reservoir type and reservoir driving mechanism. First, since the reservoir pressure in given data is higher than the bubble point pressure, the reservoir is labeled as an undersaturated oil reservoir. Second, The driving mechanism can be obtained by plotting  $F / E_o + E_{f,w}$  versus  $N_p$  to see if the reservoir has water influx or not. To start calculating OOIP all the data are available except one is missing which is the oil formation volume factor, for that a correlation of plotting oil formation volume factor from the PVT experiment versus reservoir pressure as shown Figure 3.

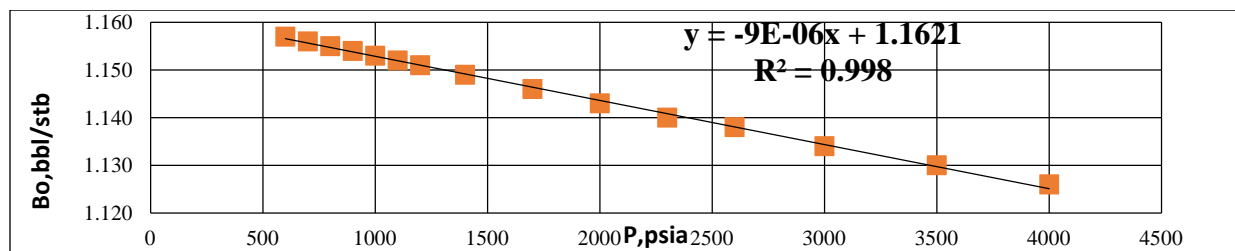


Figure 3: Curve fitting for  $B_o$  vs pressure.

From Figure 3 a straight line equation can be used to estimate  $B_o$  for any given reservoir pressure by:  $B_o = -9E-06x + 1.1621$ . Now calculating OOIP by using MBE can be achieve quickly since all the required data are available. After calculation by using Havlena and Odeh approach, the result of MBE as straight line equation

couldn't give a correct value of OOIP since no exact straight line could be obtained as shown in Figure 4. This is return to the change in the reservoir pressure and lacking in the information about the aquifer. Such this case has been introduced by other publishers and their values were far away from the one that is calculated by other methods. The calculations are shown in Table 4a & 4b.

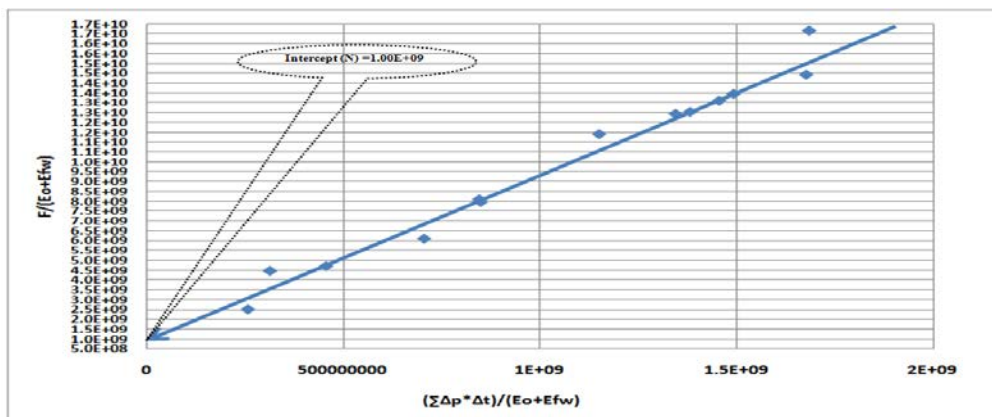


Figure 4: Plot  $F/(E_o+E_{fw})$  vs  $(\sum \Delta p * \Delta t)/(E_o+E_{fw})$  for well v42.

As a rule of thumb, the best straight line passes through the large number of points and middles the other. The OOIP from the MBE as straight line is  $1E09$  which less than the value obtained from the volumetric method. Right now a decision couldn't be making whether this value is the correct or the volumetric estimation. In the end of MBE method, MBAL software for MBE method is used to see if better result can be obtained. MBAL is commonly used for modelling the dynamic reservoir effects prior to building a numerical simulator model (7). As a result, the result shows difference from MS excel sheet which gave higher value of OOIP which is  $2.2 E09$ , it is indicate whether MBAL or excel sheet the result can never reach a closed value of the volumetric estimation.

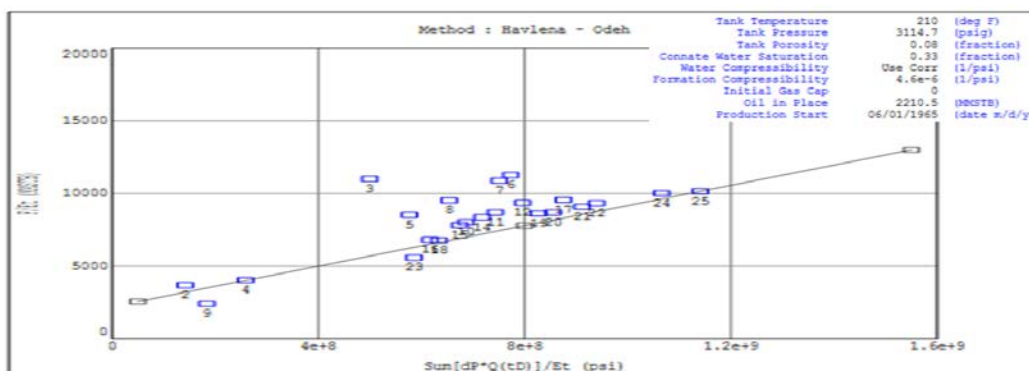


Figure 5: MBAL software result for estimation OOIP by using MBE method, analysis window (7).

**Table 4-a:** Calculation of OOIP using MS excel of well V42 (6):

<b>Date</b>	<b>Np</b>	<b>Wp</b>	<b>P</b>	<b>Bo</b>	<b>Δt</b>	<b>Δp</b>	<b>Eo</b>
<b>m/d/year</b>	<b>MSTB</b>	<b>MSTB</b>	<b>psia</b>	<b>bbf /STB</b>	<b>days</b>	<b>psia</b>	<b>bbf /STB</b>
6/1/1965	4349.1	1.1	3079	1.1340	0	21	0
6/1/1974	12454.5	23.3	2796	1.1370	3285	304	0.001936
6/1/1976	13396.1	29.8	3032	1.1350	730	68	-0.000188
6/1/1982	16799	56.7	2727	1.1380	2190	373	0.002557
6/1/1983	17138.7	67.8	2962	1.1350	365	138	0.000442
6/1/1986	18646.1	77.6	3007	1.1350	1095	93	0.000037
6/1/1988	19583.7	108.3	2986	1.1350	365	114	0.000226
6/1/1989	20020.8	108.9	2338	1.1410	365	762	0.006058
6/1/1991	21202.9	128.9	2951	1.1360	730	149	0.000541
6/1/1992	21747.9	137.5	2982	1.1350	365	118	0.000262
6/1/1994	22570.9	147.8	3031	1.1350	365	69	-0.000179
6/1/1996	23421	191.3	2916	1.1360	730	184	0.000856
6/1/1997	24150.8	279.8	2853	1.1360	365	247	0.001423
6/1/1999	25037.8	579.6	2764	1.1370	730	336	0.002224
6/1/2000	25404.2	741.2	2935	1.1360	365	165	0.000685
6/1/2001	25770	906.9	2748	1.1370	365	352	0.002368
6/1/2002	26068.7	1023.8	2850	1.1360	365	250	0.00145
6/1/2003	26245	1060.4	2850	1.1360	365	250	0.00145
6/1/2005	26999.4	1553.9	2850	1.1360	730	250	0.00145
6/1/2006	27402.7	1922.5	2850	1.1360	365	250	0.00145
6/1/2008	28144.9	2703.3	2600	1.1390	730	500	0.0037
6/1/2009	28367	3119.8	2850	1.1360	365	250	0.00145

**Table 4-b:** Calculation of OOIP using MS excel of well V42 <sup>(6)</sup>:

Efw	Eo+Efw	F	F/(Eo+Efw)	$\Delta p * \Delta t$	$\Sigma \Delta p * \Delta t$	$(\Sigma \Delta p * \Delta t) / (Eo + Efw)$
bbf /STB	bbf /STB	bbf	STB	Psiadays	Psiadays	Psiadays/ bbf /STB
8.61E-05	-5.25E-04	4.93E+06	-9.40E+09	0.00E+00	0.00E+00	0.00E+00
1.25E-03	3.18E-03	1.42E+07	4.46E+09	9.99E+05	9.99E+05	3.14E+08
2.79E-04	9.09E-05	1.52E+07	1.68E+11	4.96E+04	1.05E+06	1.15E+10
1.53E-03	4.09E-03	1.92E+07	4.69E+09	8.17E+05	1.87E+06	4.56E+08
5.66E-04	1.01E-03	1.95E+07	1.94E+10	5.04E+04	1.92E+06	1.90E+09
3.82E-04	4.19E-04	2.12E+07	5.08E+10	1.02E+05	2.02E+06	4.82E+09
4.68E-04	6.94E-04	2.24E+07	3.22E+10	4.16E+04	2.09E+06	3.01E+09
3.13E-03	9.18E-03	2.30E+07	2.50E+09	2.78E+05	2.37E+06	2.58E+08
6.11E-04	1.15E-03	2.42E+07	2.10E+10	1.09E+05	2.48E+06	2.15E+09
4.84E-04	7.46E-04	2.48E+07	3.33E+10	4.31E+04	2.52E+06	3.38E+09
2.83E-04	1.04E-04	2.58E+07	2.48E+11	2.52E+04	2.58E+06	2.48E+10
7.55E-04	1.61E-03	2.68E+07	1.67E+10	1.34E+05	2.71E+06	1.68E+09
1.01E-03	2.44E-03	2.78E+07	1.14E+10	9.02E+04	2.80E+06	1.15E+09
1.38E-03	3.60E-03	2.91E+07	8.08E+09	2.45E+05	3.05E+06	8.46E+08
6.77E-04	1.36E-03	2.97E+07	2.18E+10	6.02E+04	3.11E+06	2.28E+09
1.44E-03	3.81E-03	3.03E+07	7.95E+09	1.28E+05	3.23E+06	8.49E+08
1.03E-03	2.48E-03	3.08E+07	1.24E+10	9.13E+04	3.33E+06	1.34E+09
1.03E-03	2.48E-03	3.10E+07	1.25E+10	9.13E+04	3.42E+06	1.38E+09
1.03E-03	2.48E-03	3.24E+07	1.31E+10	1.83E+05	3.60E+06	1.45E+09
1.03E-03	2.48E-03	3.33E+07	1.34E+10	9.13E+04	3.69E+06	1.49E+09
2.05E-03	5.75E-03	3.50E+07	6.09E+09	3.65E+05	4.06E+06	7.05E+08
1.03E-03	2.48E-03	3.57E+07	1.44E+10	9.13E+04	4.15E+06	1.68E+09

### 3.3. Third, Reservoir Simulation Method

In this study, reservoir simulation software was used to calculate the initial oil in place. CMG (Computer Modelling Group) is reservoir engineering software. CMG consist of different applications which are BUIDER, IMEX, and RESULTS. The BUILDER is to build reservoir simulation model, IMEX for black oil reservoir, and RESULTS to have results graph <sup>(8)</sup>. As a result, a reservoir simulation model was built with 29

vertical wells. The input data for that model were obtained from Waha Oil Company as listed in Tables 1, 2, and 3. In this case of field study, there is a lot of missing information, which returns to the difficulty to obtain them either from the company or from the reservoir itself. For this reason, CMG software was chosen in this study to estimate the OOIP. This simulator can generate some information which aren't available from the source. To build model there are some steps need to be followed. First, start with basic information which includes: started date, field unit, and grid number. Second, a grid system type has been used to build the area for the Belhedan reservoir. The surface area of the reservoir is 18600 acre, and consists from six layers with different reservoir properties. Third, reservoir rock and fluid used as an average value for each layer. After inserting all the required data, the reservoir model becomes ready to run and get result. Only one step still left in this model is drilling wells. A twenty nine vertical well has been drilled in the reservoir. The run was achieved and the result will be discussed acceptable. In the end, Figure 6 shows the grid top, grid thickness, reservoir porosity, permeability, net pay, water saturation, and other information as showed below.

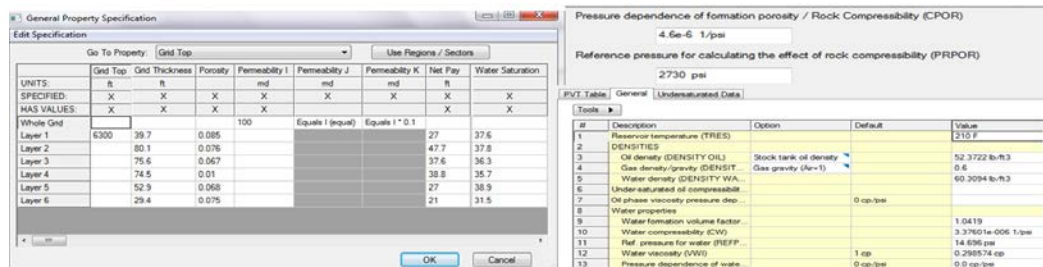


Figure 6: General property specification<sup>(8)</sup>

Finally, after the model has been run and the result of that model of original oil in place is highly which is 1.4 MMMScf. The result of OOIP is acceptable and close to volumetric method then MBE, which make simulation has the correct value as sent it to the company for verification. Figure 7 shows the results of CMG model and oil prediction from 1965 to 2020 respectively. The prediction was done without having history matching where the well assumed producing oil from the day started until 2020.

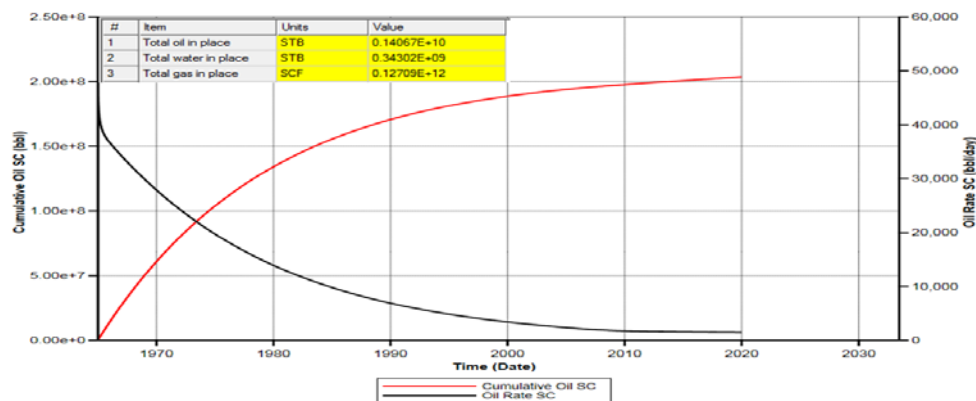


Figure 7: Result of simulation run and cumulative oil prediction and oil flow rate<sup>(8)</sup>

#### 4. Conclusions

Three different methods were used to calculate the OOIP. The obtained results from these methods were different. The difference in the results between them returns to the availability of the reservoir data. The amount of OOIP that is getting from Waha Oil Company is around 1.36 MMMSTB which is close to software result and volumetric result. The diversity in the results is return for some reasons which can be summary as: First, Volumetric method is the easiest, quickest method and doesn't need much information to estimate OOIP. Second, results of MBE as straight line equation method by excel or MBAL software aren't acceptable at all, because there are some missing information about the driving mechanism that providing the energy to the reservoir. Third, Reservoir simulation method is a modern method in petroleum industry to calculate the OOIP and making prediction and history matching as well, the software is more acceptable since it generate any other information in case its missing.

#### Acknowledgment

The authors would like to express their gratitude to the Waha Oil Company for supplying the data ,and to West Virginia University for providing the software used in this study.

#### References

- [1]. B.C Craft, M. Hawkins, "Applied Petroleum Reservoir Engineering", Englewood Cliffs, NJ 07632, 1991.
- [2]. Aminian, K, "Class Note of Reservoir Engineering PNGE 330", Spring 2006.
- [3]. Tariq Ahmed, "Applied Reservoir Engineering, second Edition Handbook, Butterworth-Heinemann 2001.
- [4]. Tariq Ahmed, Paul D. Mc Kinney, "Advanced Reservoir Engineering", Anadarko Canada Corporation, 2005.
- [5]. West Virginia University, "Petroleum Engineering Department", [http:// www.wvu.edu](http://www.wvu.edu),2014.
- [6]. Waha Oil Company, "Reservoir Engineering Department", January 1st 2014.
- [7]. MBAL software, "West Virginia University, Petroleum Engineering Department", [http:// www.wvu.edu](http://www.wvu.edu),2014.
- [8]. CMG software, "West Virginia University, Petroleum Engineering Department", [http:// www.wvu.edu](http://www.wvu.edu),2014.

#### Nomenclature

$\phi$ = Porosity, dimensionless.	$S_w$ = Water saturation, percentage
A= Cross section area, acre	h = Net pay thickness, ft
$P_i$ = Initial reservoir pressure, Psi	$\Delta p$ = Change in reservoir pressure = $P_i - P$ , Psi
P =Average reservoir pressure, Psi	N=Initial (original) oil in place, STB
$P_b$ = Bubble point pressure, Psi	$G_p$ =Cumulative gas produced, scf
$N_p$ = Cumulative oil produced, STB	$R_p$ = Cumulative gas-oil ratio, scf/STB
$W_p$ = Cumulative water produced, bbl	$R_s$ = Gas solubility, scf/STB
$R_{si}$ = Initial gas solubility, scf/STB	$B_o$ = Oil formation volume factor, bbl/STB
$B_{oi}$ = Initial oil formation volume factor, bbl/STB	$B_g$ = Gas formation volume factor, bbl/scf
$B_{gi}$ = Initial gas formation volume factor, bbl/scf	$G_{inj}$ =Cumulative gas injected, scf
$W_{inj}$ = Cumulative water injected, bbl	G =Initial gas-cap gas, scf
$W_c$ = Cumulative water influx, bbl	$C_i$ =Formation (rock) compressibility $Psi^{-1}$
m=Ratio of gas-cap to reservoir oil volume, bbl/bbl	$C_w$ =Water compressibility, $Psi^{-1}$

# Pressure Transient Analysis by Using MS. Excel Sheet and Computer Programming

Essa M. Tabar<sup>1</sup>, Ali Omran Nasar<sup>2</sup>, Tariq Basher<sup>3</sup>

1etabare4@gmail.com, 2ali\_omran95@yahoo.com, 3tariq.alkaseh@gmail.com

<sup>1,2,3</sup>Petroleum Engineering Department, Engineering Faculty, Sirte University, Libya

## ABSTRACT

Paper shows an effective using of two programs (MS Excel and computer programming) to analysis the pressure build up test data. The programs were used to determine the best infinite-reservoir acting by the relationship which between the shut-in pressure and logarithm of the shut-in time. The purpose of well test analysis is to identify the type of reservoir involved and to determine the parameters of the reservoir quantitatively. Data from one well, has been analyzed by application of modern well-test analysis techniques, such as derivative analysis and computer programming, in addition to the conventional log-log and semi-log methods, and then double check by using Type curve matching. MS Excel sheet and computer programming are using to identify: Wellbore storage effect, Middle time region “ straight line”, Late time region “ boundary effect”, and then calculate the permeability and skin factor. The results of two programs shows that the well is located near a sealing fault. Hence, they indicate that Horner method is the most accurate than derivative methods.

**Keyword**— buildup test, pressure transient, derivative method, skin factor, permeability

## 1. Introduction

The pressure buildup test is conducted by producing a well at constant rate for some time, shutting the well in, allowing the pressure to buildup in the wellbore, and recording the pressure in the wellbore as a function of time. From these data, it is possible to estimate formation permeability and current drainage-area pressure, and to characterize damage or stimulation and reservoir heterogeneities or boundaries. The method used to analyze the pressure buildup tests can be classified into three main groups; conventional methods (Horner and MDH), pressure derivative in 1983[1], and then double check by sing type curve matching methods. This paper present analysis of one field cases of the pressure buildup test using MS Excel and computer programing (PT4).

During the last decade, the theory and application of pressure transient testing has tremendous improvements, and many solutions and techniques have been proposed to analysis variety of reservoirs .The purpose of analyzing well test, and production data is to determine the ability of a formation to produce reservoir fluids, where needed to do this by estimating formation properties from reservoir data. Some of the relevant properties that must be determined are permeability, skin effect, and initial reservoir pressure, in general, characterization or description of the reservoir-well system in order to evaluate well damage or

stimulation, fracturing or not of the well, the existence of faults or flow barriers, the approximate shape of the drainage area of the reservoir or the change of the reservoir lithological properties [2].

For analysis purpose, pressure drawdown and build-up test data are usually separated into three regions which represent different analysis, and interpretation scenarios. The "early time region" is typically affected by wellbore storage while "middle time "region is indicative of the characteristics of the reservoir itself (transient flow), and finally, the "late time region" pertains to data affected by reservoir boundaries. A typical pressure test may not contain all three regions. It is important to note that the reservoir properties calculated from both build-up and drawdown tests represent average properties within that drainage area.

There are many graphical techniques that can be used to analyze well test data; these techniques include Cartesian, semi-log, and log-log plots of pressure and pressure drop function as shown in Figure (1). The particular analysis technique to be used depends uniquely on the reservoir to be tested. In the fact, it is important to use the log- log plot first, as an excellent diagnostic tool to identify the regions of the flow in a reservoir.

The objective of this paper to describe the reservoir well system and determine some reservoir properties for the given well by using different methods, these methods are the conventional method (Horner & MDH), derivative method. MS Excel sheet and PT4.0 program were used to evaluate thiswell. The analysis was used for one well in a Libyan field. The pressure of buildup data is shown in Figure 2. Properties of the well and formation are given in Table 1

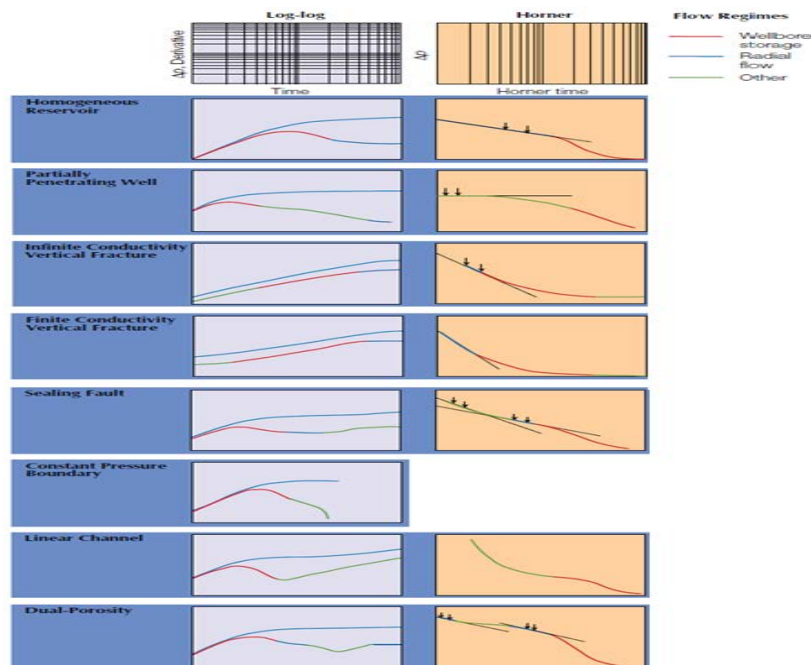
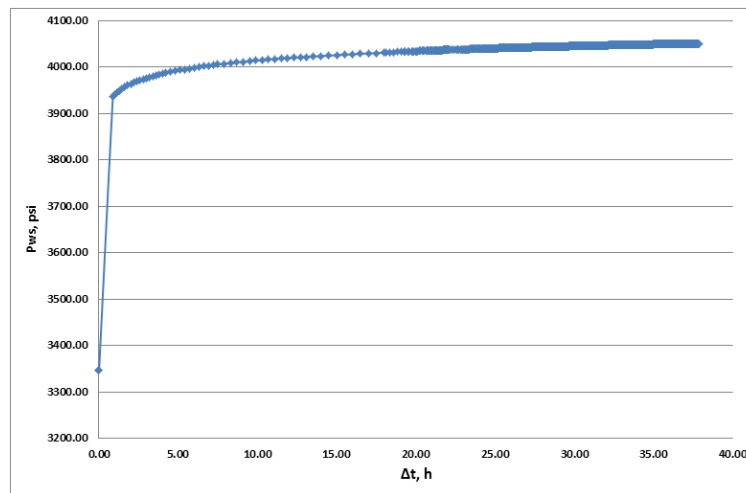


Figure 1: Log-log and semi-log plots for common reservoir systems.

**Table 1: Properties of the well and formation**

Property	Value
$q_o$ (STB/D)	3540
$\Phi$ (fraction)	0.171
$\mu_o$ (cp)	0.75
$C_t$ (psi <sup>-1</sup> )	1.27E-05
$r_w$ (ft)	0.354
$h$ (ft)	45.75
$B_o$ (RB/STB)	1.3
$P_{wf}$ (psia)	3346.50
$t_p$ (hours)	12.5



**Figure 2: Pressure buildup of the well**

## 2. Theories of Methods Used

### 2.1. Horner Method

Combining the law of conservation of mass and Darcy's law for the isothermal radial flow of fluid of small and constant compressibility toward a well in a circular reservoir, results a partial differential equation which called the Diffusivity Equation [3].

$$\frac{d^2 P}{dr^2} + \frac{1}{r} \frac{dp}{dr} = \frac{\phi \mu C_t}{0.000264k} \frac{dp}{dt} \quad (1)$$

Assuming that:

1. A well produce at a constant rate,
2. The reservoir is at uniform pressure,  $P_i$ , before production begins, and
3. The well drains an infinite area.

Solution of Eq.(1) is:

$$P = P_i + 70.6 \frac{q\beta\mu}{kh} E_i \left( \frac{-948\phi\mu C_i r^2}{kt} \right) \quad (2)$$

Where:

B=Formation volume factor, res vol./surface vol

$C_t$  = Total compressibility,psi<sup>-1</sup>

$E_i$  = Exponential wellbore storage coefficient

h = Net formation thickness, ft.

k = Reservoir rock permeability, md

P= Reservoir pressure, psi.

$P_i$  = Initial reservoir pressure, psi.

q =Flow rate, STB/D

r = Distance from center of wellbore, ft

t = Elapsed time, h

$\mu$  = Viscosity, cp.

$\phi$  = Porosity of reservoir rock, dimensionless.

$$E_i(-x) = -\int_x^\infty \frac{e^{-u}}{u} du = \text{the Ei function or exponential}$$

For  $x < 0.02$ ,  $E_i(-x)$  can be approximated with an error less than 0.6% by  $E_i(-x) = \ln(1.781x)$

For  $r = r_w$  the argument of the Ei function is sufficiently small after a short time that we can use the logarithmic approximation, thus, the is:

$$P_i - P_{wf} = -70.6 \frac{q\beta\mu}{kh} \left[ \ln \left( \frac{1688 \phi\mu C_i r_w^2}{kt} \right) \right] \quad (3)$$

It is convenient to define a skin factor, S, in term of the properties of the equivalent altered zone:

$$S = \left( \frac{k}{k_s} - 1 \right) \ln \left( \frac{r_s}{r_w} \right) \quad (4)$$

Where:

$k_s$ =Permeability of altered zone, md

$r_s$  = Radius of altered zone (skin effect),ft

$r_w$  =Wellbore radius, ft

$S$  = Skin factor, dimensionless.

For buildup test using principle of the superposition for well has produced for time  $t_p$  at flow rate ( $q$ ) before shut-in, and if we call time elapsed since shut-in  $\Delta t$ , the pressure drop can be modeled by Eq 5.

$$P_i - P_{ws} = -70.6 \frac{q\beta\mu}{kh} \left[ \ln \left( \frac{1688 \phi \mu C_i r_w^2}{k(t_p + \Delta t)} \right) - 2s \right] - 70.6 \frac{(-q)\beta\mu}{kh} \left[ \ln \left( \frac{1688 \phi \mu C_i r_w^2}{k\Delta t} \right) - 2s \right] \quad (5)$$

Where:

$t_p$  : Cumulative production/most recent production rate=pseudo producing rate, h

$\Delta t$  : Time elapsed since shut-in, h.

and become:

$$P_{ws} = P_i + 70.6 \frac{q\beta\mu}{kh} \ln \left[ \left( \frac{t_p + \Delta t}{\Delta t} \right) \right] \quad (6a)$$

or

$$P_{ws} = P_i + 162.6 \frac{q\beta\mu}{kh} \log \left[ \left( \frac{t_p + \Delta t}{\Delta t} \right) \right] \quad (6b)$$

The form of Eq6b suggests that shut-in BHP,  $P_{ws}$  recorded during a pressure build up test should plot as straight line function of  $\log [(t_p+\Delta t)/\Delta t]$ .Further, the slope of ( $m$ ) of this straight line should be:

$$m = -162.6 \frac{q\beta\mu}{kh}$$

It is convenient to use a positive number of ( $m$ ) as following Equation.

$$m = 162.6 \frac{q\beta\mu}{kh} \quad (7)$$

Eq 8 uses to calculate formation permeability ,  $k$ , which can be determined from a buildup test by measuring

the slope  $m$ . in addition, the extrapolation of straight line to infinite shut-in time  $\left( \frac{t_p + \Delta t}{\Delta t} \right) = 1$  the pressure

at this time will be original formation pressure,  $P_i$ .

$$k = 162.6 \frac{q\beta\mu}{mh} \quad (8)$$

The skin factor is obtained from Eq 9.

$$s = 1.151 \left[ \left( \frac{P_{1hr} - P_{wf}}{m} \right) - \log \left( \frac{k}{\phi \mu c_t r_w^2} \right) + 3.23 \right] \quad (9)$$

Where:

$P_{wf}$  = Flowing BHP, psi

$P_{1hr}$  = Pressure at 1-hour shut-in time on middle time-line, psi.

## 2.2. Derivative method.

Five-point method was used to estimate the derivative pressure as shown in Figure 3. The following procedure used to identify the flow regimes in this study:

- Plot pressure derivative versus time on log-log plot (Diagnostic Plot).
- Identify the end of wellbore storage from unit slope line.
- Identify middle time region when zero slope straight line appears.
- Identify the late time region if there is boundary effects.

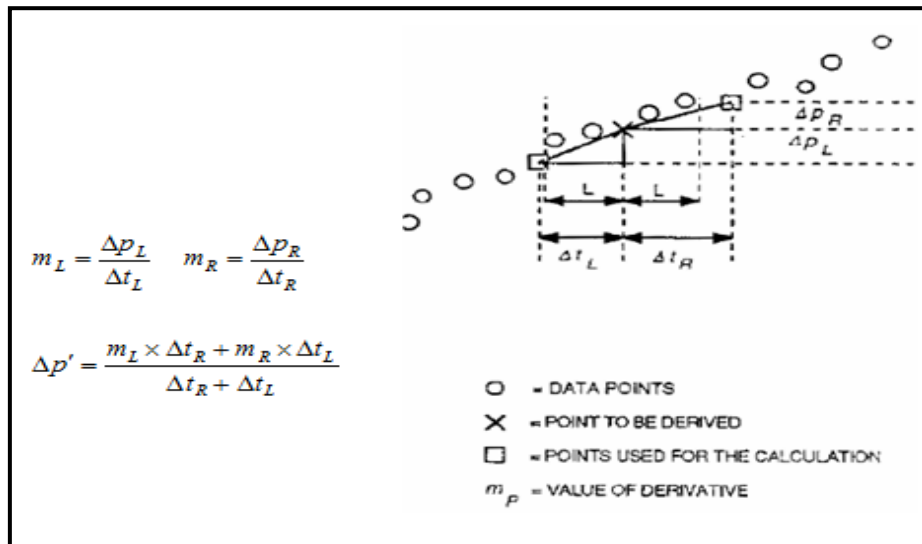


Figure 3: Five-point method for calculating the pressure derivative[4]

### 2.2.1. Determination of the pressure Derivative by MS Excel:

- 1- Plot  $\Delta p$  vs  $\Delta t$  on the log-log paper and then plot  $\Delta p'$  vs  $\Delta t$  in the same graph, where can be calculated  $\Delta P'$  from these equations:

$$m_L = \frac{\Delta p_L}{\Delta t_L} \quad (10)$$

$$m_R = \frac{\Delta p_R}{\Delta t_R} \quad (11)$$

$$\Delta p' = \frac{m_L \Delta t_R + m_R \Delta t_L}{\Delta t_R + \Delta t_L} \times \Delta t \quad (12)$$

Where:

$m_L$  = Value of derivative in pressure derivative smoothing algorithm in left side, psi/h.

$m_R$  = Value of derivative in pressure derivative smoothing algorithm in right side, psi/h.

$\Delta p'$  = Pressure derivative, psi/h.

$\Delta p_L$  = Additional pressure change owing to presence of no flow boundary in left side, psi.

$\Delta p_R$  = Pressure change in pressure derivative smoothing algorithm in right side, psi.

$\Delta t_L$  = Time change in pressure derivative smoothing algorithm in left side, h.

$\Delta t_R$  = Time change in pressure derivative smoothing algorithm in right side, h.

- 2- Estimate the formation permeability (k), skin factor (S) using the following relationship:

$$k = \frac{70.65 q \mu B}{m h} \dots\dots\dots(13)$$

$$S = 1.151 \left( \frac{(\Delta P)_s}{2.303 m'} - \text{Log} \left( \frac{K (\Delta t)_s}{\phi \mu C_t r_w^2} \right) + 3.227 \right) \dots\dots\dots(14)$$

Where:

$(\Delta p)_s$  = Pressure change coordinate during the infinite acting period, psi

$(\Delta t)_s$  = Time coordinate of a point during the infinite acting period, h.

### 2.3. Pressure Transient Software (PT4.0)

PT4.0 is one of the programs which used to analysis data that are obtained from drawdown and build-up tests. PT4.0 (Pressure transient (version.4)) is a full-featured system for evaluating pressure transient well tests. Using a standard Windows user interface, it implements most classical and log-log type curve methods, as well as an advanced "Adjust and Compare" technique to interactively interpret test data.

## 1. Calculations and Results

To illustrate the procedure, it is shown here the analysis of data of well by using MS Excel sheet and PT4.0 software. Figure 3 shows plot of  $\Delta p$  ( $P_{ws}-P_{wf}$ ) versus  $\Delta t$  on log-log plot., Figure 4 represents Horner semilog plot. The best straight line of first slope was found as shown in Figure 5. Figure 6 shows Horner semilog plot by using PT4.0 software MS Excel sheet was used to plot the derivative curve on log-log plot with the plot of ( $P_{ws}-P_{wf}$ ) versus  $\Delta t$  as shown in Figure 7. Figure 8 shows the plotting of Derivative curve by using PT4.0 software. Permeability of the formation and the skin factor were calculated as was described in previous sections. Results of analysis data of well are shown in Table 2.

**Table 2:** Results of analyzing data of the well

Property	Excel Sheet		PT4.0 Program	
	Horner	Derivative	Horner	Derivative
P* (psi)	4041	-	4043.8	-
m (psi/cycle)	90.486	-	92.68	-
K (md)	135.568	171.93	132.321	109.13
Kh, (md.ft)	6202.24	7865.8	6053.68	4993
S	1.138	3.055	0.96997	-0.308

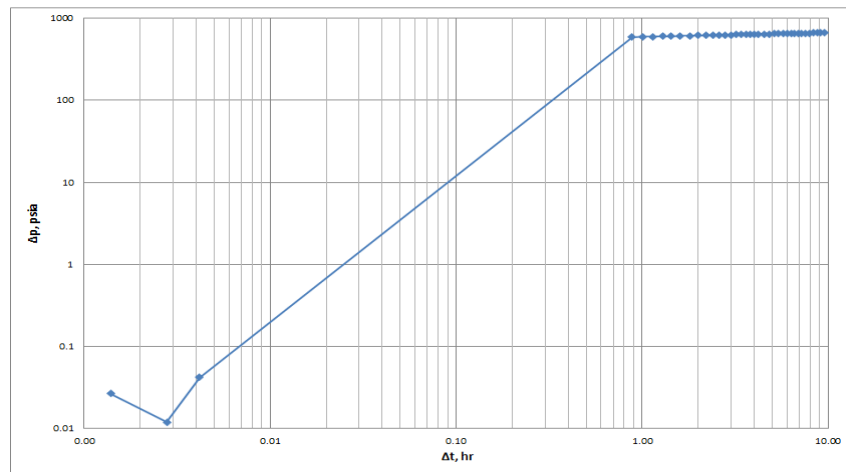


**Figure 3:**  $\Delta p$  ( $P_{ws}-P_{wf}$ ) versus  $\Delta t$  on log-log plot

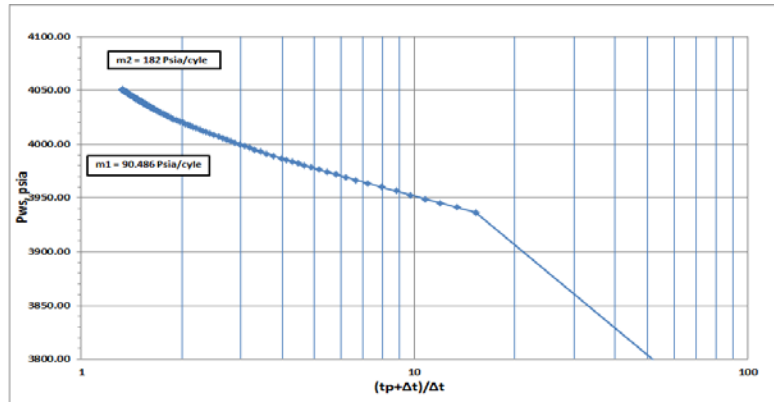


Figure 4: Horner plot of the wellby using MS Excel software

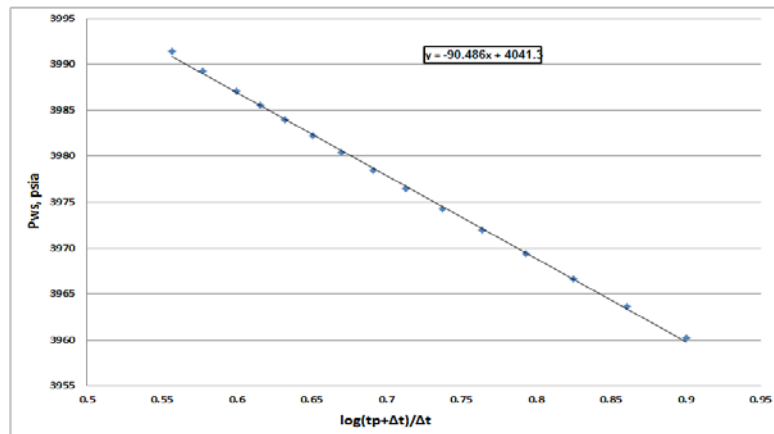


Figure 5: MTR straight line of Horner Plot

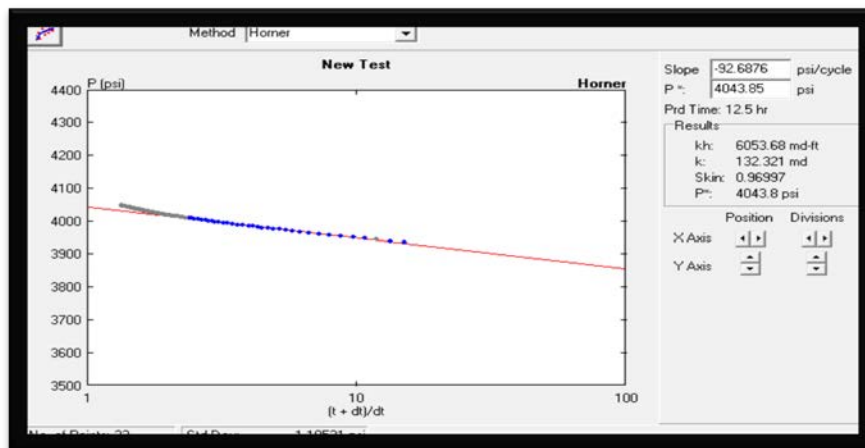


Figure 6: Horner plot for the well by using (PT4.0) software.

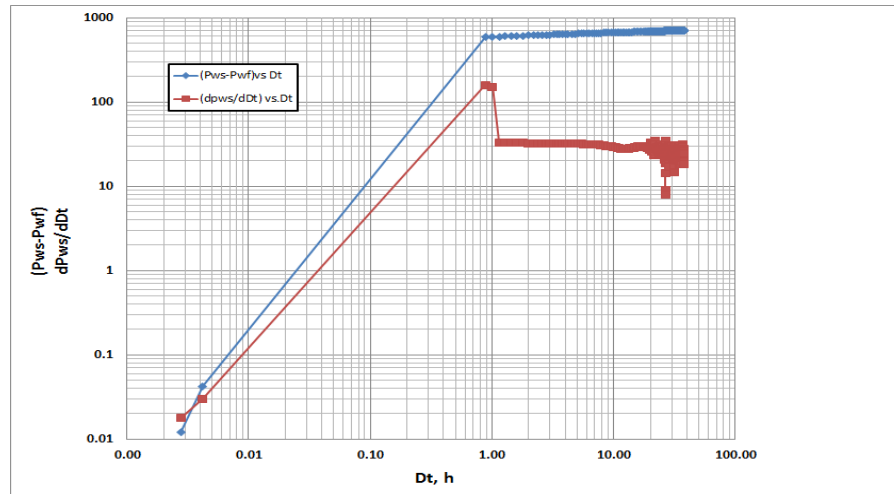


Figure 7: Derivative plot of the well by using MS Excel software

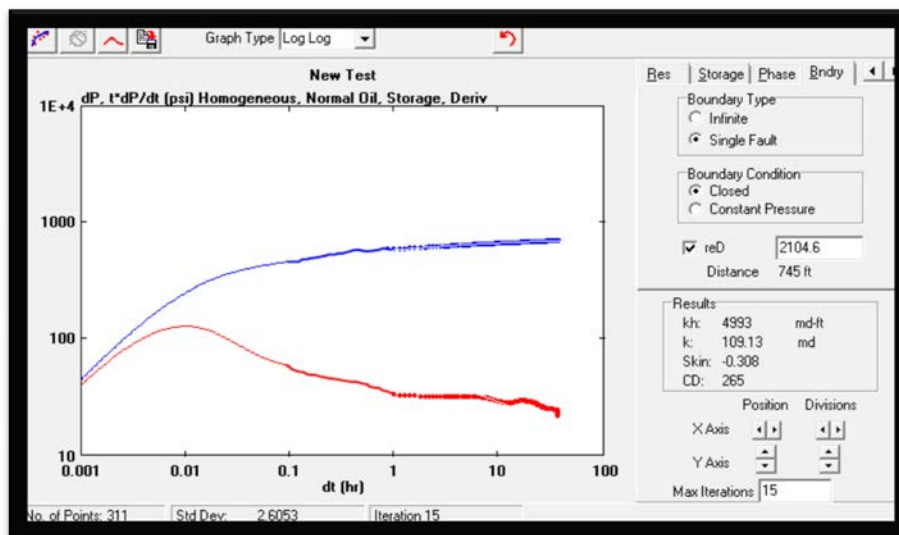


Figure 8: Derivative plot for the well by using (PT4.0) software.

## 2. Discussion

The paper presents a two programs that used to evaluate the pressure build up test for the well from Libyan field. MS Excel sheet and PT4.0 software were using to characterize the well, as well as estimation of formation permeability, skin factor and reservoir pressure. As shown for studied case, using of the pressure Horner curve was principle to identify the MTR of the test and to characterize the condition at the reservoir

boundary. The Horner plots for both programs in Figure 4 and Figure 6 show that sealing fault has appeared by two slopes. Otherwise, the derivative curve was also used to identify the MTR and to evaluate the reservoir condition and the sealing fault has not appeared clearly because the period of buildup test (37hrs) was small as shown in Figure 7 and 8. Table 2 shows the results of Horner and derivative methods by using both programs MS Excel and PT4.0 software. As the results, formation permeability by both programs are agree to each other and reservoir pressure as well. The skin factor of the well indicates that the zone around the well has small damage by using Horner plot for both programs while derivative plot gives positive value of skin factor by using MS Excel and negative value by using PT4.0 software. According to the results of the studied case which indicate that Horner method is the more accurate than derivative methods.

### 3. Conclusion

This paper presents a simple procedure to analyze the pressure buildup test using MS Excel and PT4.0 software. Sealing fault was appeared clearly in Horner plot by two slopes whereas derivative plot, the second slope was not presented clearly. Horner plot of MS Excel software gives appreciate results to PT4.0. whereas the derivative method gives not that much different results between both of programs. Results of the studied case indicates that Horner method is more accurate than method of direct derivative method. For the future, hopefully, there will be more cooperation between oil and gas governmental/international companies and PE in Sirte University, therefore to provide us the commercial petroleum simulators to develop models according to field data which help us to increase the knowledge of academic research and develop the student in academic and field study. Hence, using directly the modern programs in well testing will save time and provides reliable parameter values.

### References:

- [1]. D. Bourdet, T. M. Whittle, A. A. Douglas, and Y. M. Pirard: "A new Set of Type Curves Simplifies Well Test Analysis," *World Oil*, May 1983, pp95
- [2]. R. C. Earlougher, "Advances in Well Test Analysis," Society of Petroleum Engineers, Dallas, TX, 1977.
- [3]. D. R. Horner, "Pressure Buildup in Wells" Proceedings of Third World Petroleum Congress, E. J. Brill, Leiden, November 1951, p503.
- [4]. J. Lee, and R. A. Wattenbarger, "Gas Reservoir Engineering", SPE Textbook Series vol. 5, TX:, (1996).

## Evaluation Of Corrosion Resistance Of Mild Steel And Aluminium Using Anodic Inhibitor Method And Passivity

Dr Ali Ramadan Elkais<sup>1</sup> and Dr Mohamed K Zambri<sup>2</sup>

<sup>1</sup>elkaisali@gmail.com, <sup>2</sup>mkzambri@elmergib.edu.ly

<sup>1,2</sup> Department of Chemical and Petroleum Engineering, Faculty of Engineering, Elmergib University, Libya

### ABSTRACT

Mild steel and Aluminium considered from the metals that commonly used in engineering applications with a high proportion of up to 85%. On the other hand, due to the weakness of its resistance to corrosion environments different methods of corrosion protection are required to increase the resistance level particularly in the marine and acidic environments, where this give the significance of this study to be presented. **This** research involves studying the effect of some different corrosion resistance of mild steel and Aluminium by applying anodic inhibitor of mild steel (Sodium Dichromate and Potassium dichromate) in sea water environment and Aluminium by using passive film of  $Al_2O_3$  in acidic environment (Hydrochloric acid HCL and Nitric acid  $HNO_3$ ). An experimental work has been done and evaluation of corrosion resistance have been measured from weight loss during different period of time.

**Keyword**— Corrosion, Corrosion environment, Mild steel, Aluminum, passivity, inhibitor, Anodic

### 1. Introduction

There are many protection methods and measures have been used and considered to prevent or control corrosion process of metals and using the inhibitors was one of these methods. The inhibitor substance has been defined as the substance which can be added to a corrosive environment to decrease the rate of corrosion can occur due to this environment [1 - 3]. Inhibitor sources can be extracts (organic) , chemical solutions (Inorganic), Fig (1) illustrates the classification of inhibitors. In addition, the mechanism of how these substances minimize the corrosion rate can be summarized as these substances form a very thin film on the metal surface in different ways that can affect directly on the environment's corrosivity rate [4].

Anodic inhibitors which also can be called "*passivation inhibitors*" that work on minimizing the anode reaction and gradually cause blocking the anode reaction and supporting occurring the natural reaction of passivation metal surface to produce a very thin layer (film) adsorbed on the metal surface and protecting it from corrosion [6].

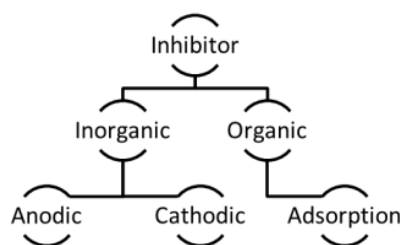
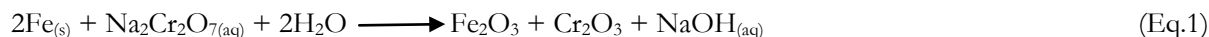


Figure (1): The classification of inhibitors [4]

## 2. Materials selection and Methods

In this work two metals were tested and different protection methods were applied on each of them. **The first** metal was Mild steel and chemical inhibitor was used to protect the metal from corrosion and sodium dichromate solution was used as coating material which historical been considered as very active inhibitor [5]. When the metal exposed to this chemical solution for a certain of time ( in this work 48 hours) a very thin layer from iron oxide and chromium oxide was produced (Eq. 1) where this layer works to protect the mild steel surface from corrosion by isolating it from surrounding environment (sea water & atmosphere).



**The second** metal was Aluminium and has been protected experimentally also by an oxide layer produced on the metal surface in different way (*passivation inhibitor*). This experiment is to prove that not all environments can produce the protection layer even they are have the same classifications (e.g. acids). In this work an Aluminium bar was exposed to different environments (HCL & HNO<sub>3</sub>) and an Aluminium oxide layer was produced from the reaction between the Nitric acid and aluminium surface to protect the metal from the corrosive environment.

## 3. Experimental work and results

### 3.1. Mild steel protection

In this experiment a sample of mild steel has been used to test the ability of a specific chemical inhibitor (Sodium dichromate Solution) to protect the metal surface from corrosion in two different environments (sea water & atmosphere). Sodium dichromate solution was prepared in two concentrations which are 0.1M and 0.5M and the following point were applied and considered:

- The sample of mild steel was polished, prepared, and weighted,  $W_1$  (Fig. 2).

- Immerse the sample in sodium dichromate solutions (0.1M & 0.5M) for a period of time (1 – 3 days). Figure 3 shows the protection layer of chrome oxide.
- After 1 day remove the sample from solutions and record the total weight,  $W_2$ .
- Calculate the weight of coating layer ( $W_2 - W_1$ ).
- Immerse the coated sample in the corrosive environment (sea water) for 24 hours.
- Remove the sample from sea water and record the total weight,  $W_3$ .
- Calculate the weight loss ( $W_2 - W_3$ ).
- Repeat the above steps for the other period of time, environment and time of coating with recording the results for each case.



**Figure 2:** Prepared sample of mild steel

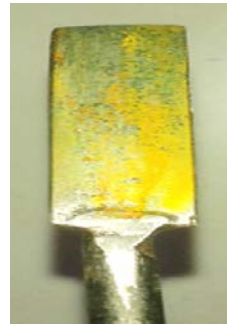


**Figure 3:** Coated sample of mild steel.

To make sure that the coating substance gives the aim that used to, the mild steel has been exposed to the same corrosive environment without applying the coating substance on the surface to produce the protection layer, Figure (4) shows the affected uncoated sample of mild steel before and after the sample exposed and immersed in sea water for 5 days . Figure (5) shows a coated sample of mild steel also before and after immersed in sea water for 5 days. The results obtained for different conditions are illustrated in tables 1 – 3:



**Figure 4:** Uncoated sample of mild steel immersed in sea water for 5 days



**Figure 5:** Coated sample of mild steel immersed in sea water for 5 days

**Table (1):** Corrosion of mild steel without protection

Samples	Weight of sample, gm	Time of exposure in sea water, hrs	Weight loss gm / cm <sup>2</sup>
1	26.7253	24	0.00295
2	27.1127	48	0.03333
3	26.7285	72	0.03809
4	26.8365	96	0.04095

**Table (2):** Protection of mild steel by 0.1M sodium dichromate in sea water and air

Environment	Sample weight, gm	Coating layer, gm	Weight loss	Exposure time
Sea water	26.5045	0.0006	0.0005	24 hrs
Atmosphere	26.3992	0.0007	0.00045	7 days

**Table (3):** Protection of mild steel by 0.5M sodium dichromate in sea water and air

Environment	Sample weight, gm	Coating layer, gm	Weight loss	Exposure time
Sea water	26.0047	0.0031	0.0010	24 hrs
Atmosphere	25.8415	0.0016	0.0004	5 days

### 3.2. Aluminium protection (*Passivation*)

The Aluminum metal has been considered one of the metals that have the ability to form an oxide layer on the surface comes from the reaction between the environment and the metal surface and this layer works to protect the metal from corrosion [6]. Therefore, to evaluate this property for the Aluminum metal, an aluminum samples were immersed in acids solutions (10%v/v HCL and 10% v/v HNO<sub>3</sub>). An oxide layer was formed from the reaction between the Aluminum and Nitric acid where this reaction occurs due to the availability of oxygen atoms in nitric acid. On the other hand, in case of HCL acid this oxide layer could not be formed due to the lake of oxygen in the reaction environment and a reaction of consuming the aluminum was occurred producing aluminum chloride and hydrogen gas (Eq. 2) and this later comes from consuming the electrons resulted from the aluminum to convert the hydrogen ion to hydrogen gas on the aluminum metal surface (Eq. 3). This was clear from monitoring the concentration of hydrogen ion in the reaction solution and the change in PH value. The results of this monitoring was recorded and presented in table 4. Figure (6) shows the different between two samples of Aluminum where the corroded one immersed in HCL and the protected one immersed in Nitric acid.

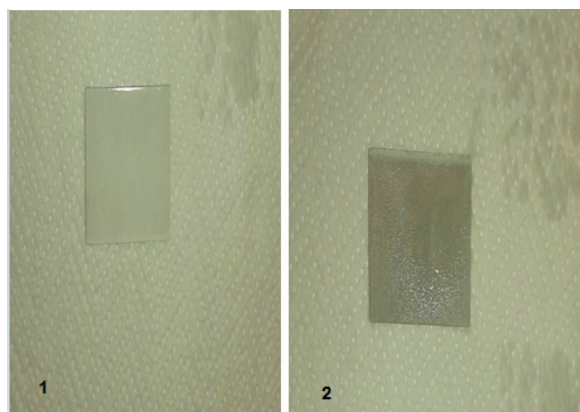


**Figure 6:** Aluminum sample (1) protected (HNO<sub>3</sub>) Aluminum sample (2) corroded (HCL)

**Table 4:** Concentration monitoring of hydrogen ion and pH at 20 °C

Days	HCL, 10% v/v			HNO <sub>3</sub> , 10% v/v		
	H <sup>+</sup> mv	Conc.	pH	H <sup>+</sup> mv	Conc.	pH
1	271		2.89	324		1.70
2	245		4.01	321		2.24
3	175		4.40	285		2.14
4	156		5.40	294		2.13
5	130		5.51	263		2.59
6	106		5.80	266		2.57
7	101		6.90	255		2.62
Weight loss in HCL acid solution = 0.9116 gm after 7 days						
Weight loss in Nitric acid solution = 0.1361 gm after 7 days						

In the table it was clear that the pH change with time due to the change in concentration of hydrogen ion in hydrochloric acid solution which comes from the passive layer of protection not formed. On the other hand, there was a slight change in the concentration of hydrogen ion in nitric acid because of the formation of protection passive layer. Figure 7 and Figure 8 prove that decreasing the concentration of hydrogen ion leads to increase the pH of HCL acid solution. In addition, there was a slight decrease in the concentration of hydrogen ion in nitric acid led to also a slight increase in pH because of the protection layer.

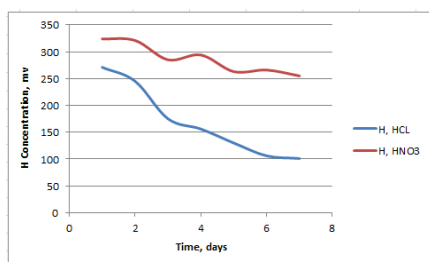


**Figure 7:** Monitoring of hydrogen ion concentration in HCL & HNO<sub>3</sub> solutions

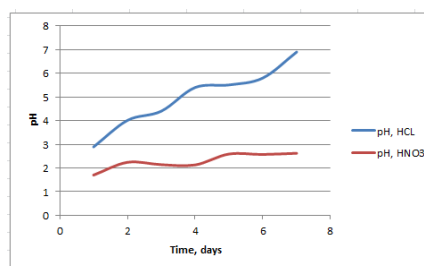


**Figure 8:** Monitoring of PH in HCL solutions

#### 4. Conclusions

The results obtained confirmed that the chemical solution of sodium dichromate can be successfully used as chemical inhibitor to protect the mild steel in sea water and atmosphere. Moreover, the most important result achieved in this work that the passive film (protection layer) cannot be formed for all metals and corrosive environments because of the dependency on the reaction between the metal surface and environment.

#### Acknowledgment

The authors are thankful to the Chemical & petroleum Engineering Department, Engineering Faculty, Elmergib University, Khums Libya, for providing laboratory facilities to complete the research.

#### References

- [1]. P. R. Roberge, "Handbook of Corrosion Engineering", *New York: Mc Graw Hill Hand-Book*, 1999
- [2]. Edrah S., Elkais A., Zambri M. (2016) Anticorrosion of Mild Steel in Sea Water at different temperatures by using green inhibitors "Posidonia oceanica" "1st International Conference on Chemical, Petroleum, and Gas Engineering" at Al-Mergib Unversity, Faculty of Engineering, department of Chemical and petroleum engineering 20 -22 / 2016.
- [3]. Taleb H. Ibrahim and Mohamed Abou Zour " Corrosion Inhibition of Mild Steel using Fig Leaves Extract in Hydrochloric Acid Solution" *Int. J. Electrochem. Sci*, 6 (2011) 6442 – 6455.
- [4]. Camila G. Dariva and Alexandre F. "Corrosion Inhibitors – Principles, Mechanisms and Applications", *Journal of INTECH (Open Science / Open minds)*, 2014, Access online on 01/04/2018 at <http://dx.doi.org/10.5772/57255>.
- [5]. B. E. Roethell, and G. L. Cox, "Prevention of Corrosion of Metals by Sodium Dichromate as Affected by Salt Concentrations and Temperature" *Industrial & Engineering Chemistry*, 1931, 23 (10), pp 1084–1090
- [6]. Firas F. Sayyid, Ali M. Ali, and Wadhah A. Tawfek, " Evaluation of Corrosion Resistance of Medium Carbon Steel using different Protection Methods" *Journal of Engineering and Technology*, 2012, Vol 30, Issue 7

# Optimum Deposition of Tungsten Oxide on Titania Nanotubular Arrays and Study the Photo activity of Nano-Composite Photoanode

Asma Mustafa Husin Milad<sup>1\*</sup>, Soud Saad Awitil<sup>2</sup>, Mohammad B. Kassim<sup>3</sup>, Wan Ramli Wan Daud<sup>4</sup>

<sup>1</sup>asma.aga2009@gmail.com, <sup>2</sup>soudsaad177@gmail.com, <sup>3</sup>mb\_kassim@ukm.edu.my, <sup>4</sup>wramli@eng.ukm.my

<sup>1,2</sup>Department of Computer Science, College of Engineering, Elmergib University, Libya

<sup>3</sup>School of Chemical Sciences and Food Technology, Faculty of Science and Technology, UKM, Bangi, Malaysia

<sup>4</sup>Department of Chemical & Process Engineering, Faculty of Engineering & Built Environment, UKM, Bangi, Malaysia

## ABSTRACT

The novelty of this research works in the two-step formation of tungsten oxide (WO<sub>3</sub>)-loaded TiO<sub>2</sub> nanotube arrays composite film by study the optimum conditions of electrodeposition of WO<sub>3</sub> nanoparticles on TiO<sub>2</sub> nanotubes arrays based on their photo-activity performance. The Whave been incorporated from a sodium tungstate-based aqueous electrolyte containing from 0.2 M sodium tungstate (Na<sub>2</sub>WO<sub>4</sub>) with addition of 0.13 M hydrogen peroxide (30%) and drops from H<sub>2</sub>SO<sub>4</sub> up to get pH = 1; it accumulates to form a self independent structure of WO<sub>3</sub> on the surface of the nanotubes. WO<sub>3</sub> was deposited for several times intervals at room temperature and annealed at 350 °C for 30 minutes. TiO<sub>2</sub> nanotubes(TNTA) were successfully grown by anodizing of titanium foil (Ti) in organic (98% vol., ethylene glycol, 2 vol.% Di water and 0.5 wt% ammonium fluoride and acidic (0.5M phosphoric acid and 0.14M sodium fluoride) electrolyte. The possible growth of TiO<sub>2</sub> nanotubes in the applied potential at 20V for 45 minutes was investigated. It were found such electrochemical condition resulted in formation of nanotube with average diameter 50 & 120 nm and the length 3.5 & 0.6 μm for organic and acidic electrolytes respectively. The anodized samples were annealed at 500 °C in N<sub>2</sub> gas for 3 hours. The structural, morphology and composition of TiO<sub>2</sub> nanotubes and WO<sub>3</sub>/TiO<sub>2</sub> nanotube were characterized with XRD, FESEM and EDX. FESEM results of the nanotubular arrays showed uniform arrays of titaniananotubular and showed. EDX results showed trace of tungsten has been incorporated into TiO<sub>2</sub>. The influences of tungsten content on the photocurrent densities of WO<sub>3</sub>/TiO<sub>2</sub>nanotubularphotoanodes were investigated by recording current-potential profiles. The preliminary results indicated that the WO<sub>3</sub>/TiO<sub>2</sub> produced showed good photocurrent densities due to the behavior of W<sup>6+</sup> ions which allows to electron traps that suppress electron-hole recombination and exploit the lower band gap of material to produce a water splitting process by increasing the charge separation and extending the energy range of photo-excitation for the system.

**Keyword**— Titanium oxide nanotubular arrays (TNT), Anodization, tungsten oxide (WO<sub>3</sub>), electrodeposition, photoelectron chemical measurements.

## 1. Introduction

Hydrogen is an attractive alternative source of energy because it is renewable if collected through the splitting of water, burns cleanly (producing only  $H_2O$ ), and could deliver energy in the same method as fossil fuels, via combustion or electricity through the use of fuel cells. Generated hydrogen through the splitting of water is a very desirable alternative fuel for the following reasons: sunlight is a plentiful and renewable energy source [1]; the hydrogen generating device has no moving parts, therefore maintenance is minimal; and the associated infrastructure is simple [2]. Photoelectrochemical reaction for water splitting is a process in which water is split into hydrogen ( $H_2$ ) and oxygen ( $O_2$ ) on the surface of a specific type of photoactive material, namely titania ( $TiO_2$ ) semiconductor [3, 4]. The photocatalytic splitting of water using oxide semiconductors is initiated by the direct absorption of a photon, which creates separated electrons and holes in the energy band gap of the material [5]. During the past few decades, significant efforts have been made to search for a low cost and efficient photoelectron chemical cell (PEC). An ideal PEC cell needs to have an optimum band gap with the right band positions for both its CB and VB. In addition, it needs to be readily available, non-toxic and stable in an aqueous solution. Moreover, this material has to have a high absorption and good photon-to-electron conversion efficiency. So far, no single material has been found that meets all the criteria above for a cheap and efficient PEC cell. Most of the existing materials suffer from either stability issues or low photon-to-electron conversion efficiency.  $TiO_2$  has high band gap level which has a potential for water splitting under UV-light, but it cannot absorb visible light and hence, suffer from low light absorption efficiency. Anatase  $TiO_2$  shows fewer recombination reactions due to the indirect band gap and hence, produces better photocatalytic activity compared to rutile that has a direct band gap. Moreover, other oxide such as  $WO_3$  has low band gap level of 2.2-2.8 eV [6] has good absorbance in visible light but it has insufficient CB or VB edge for water reduction and oxidation; it can absorb the blue region of the solar spectrum up to ca. 500 nm. Recently,  $WO_3$  was considered as a new photoanode material or mixture material with  $TiO_2$  for water splitting because  $WO_3$  can offer relatively small band gap and has high stability in an aqueous solution. Although  $WO_3$  has shown great potential such as photo-oxidation of water with visible light and has high photocurrent levels with nanocrystals, the quantum yield is still low [7, 8]. In this work, strategies were centred on controlling the structure or the chemical composition of the  $TiO_2$  nanotube arrays composite (TNTA). The electrochemical anodization is the simplest method of fabricating TNTA from a titanium foil. The 1-D nanostructures offer highly efficient charge transport channels longitudinally. Various efforts have been made to employ mixed  $WO_3/TiO_2$  systems to enhance the efficiency of electrochromic effects in aqueous solution [9, 10]. Whereas, the enhancement of the photocatalytic performances of  $TiO_2$  was possible since  $WO_3$  can serve as an electron accepting species [11]. However,  $WO_3/TiO_2$  or  $WO_x/TiO_2$  were mainly prepared by different methods as physical mixing [12], multi-step grafting of ammonium tungstate [13, 14], improved sol-gel method, co-precipitation [15], hydrothermal method [16]

and electrodeposition [17], where  $\text{WO}_3$  or  $\text{WO}_x$  only covered the surface of  $\text{TiO}_2$  with low amounts in most situations. The ability of  $\text{WO}_x\text{-TiO}_2$  to be excited by visible light and degrade the dyes were confirmed by several researchers, where Li et al. (2001) proven that the photoactivity of  $\text{WO}_x\text{-TiO}_2$  was significantly higher than that of pure  $\text{TiO}_2$  and an optimal content of  $\text{WO}_x$  in  $\text{TiO}_2$  was found to be 3% for  $\text{WO}_x$  in  $\text{TiO}_2$  was the highest rate of methylene blue (MB) photodegradation [18]. The most related researches about  $\text{WO}_3/\text{TiO}_2$  were summarized in Table 1.

As a result, the main focus of this work is to enhance the photocurrent density of TNTA and increased its ability to generate hydrogen by deposition of  $\text{WO}_3$  nanoparticles and to form a highly efficient nanocomposite structure. As well, the optimum conditions of electrodeposition of  $\text{WO}_3$  on TNTA to get the best photocurrent of TNTA semiconductors in PEC. A full investigation of the intrinsic material properties of the resulted samples was performed, which included crystallinity, morphology, and electronic absorption spectrum, by FESEM, X-ray diffraction (XRD) and UV-VIS diffuse reflectance. Finally the optimised photoelectrodes were investigation by measuring photocurrents enhancement via PEC measurements.

## 2. Materials and Methods

Short  $\text{TiO}_2$  nanotubular array (STNTA) was prepared by anodizing a Ti-foil in **anacidic electrolyte** [30] containing 0.5M *ortho*-phosphoric acid and 0.14M sodium fluoride at pH 2 under constant stirring and the voltage profile described above. Similarly, a much longer titania nanotubes were synthesized in accordance with the procedures reported by [31] which required the anodization of T-foil in an **organic electrolyte** consisting of ethylene glycol (EG) with 2% vol. DI water and 0.3 wt% of  $\text{NH}_4\text{F}$  at pH 5.9. The post-treatment process of the TNTA prepared above involved annealing, which is a vital step for the transformation of the amorphous state of titanium oxide into anatase crystals. Prior to annealing, the surface of the anodized samples was cleaned with deionized water to remove ionic residues, and the samples were dried under  $\text{N}_2$  flow at 100 °C for 12 hr. The TNTA samples were loaded in to a muffle furnace in a ceramic boat and were annealed at 500 °C for 3 hr in  $\text{N}_2$  flow. The temperature was increased at a rate of 5 °C/min. The synthetic procedures for making Tungsten Oxide/TNTA were improved from previously reported work through few modifications such as deposition bath compositions, calcination temperature and electrodes configurations as summarized in Table 2. However, Figure 1 shows the cyclic voltammetry scan of TNTA in deposition electrolyte, whereas, the cyclic voltammogram suggested that the electrodeposition potential of about -0.38 V which is similar to the reported potential for  $\text{W(IV)}$  reduction to  $\text{W(0)}$  [32].

**Table 1:** Summary of previous researches about Tungsten trioxide on TNTA

	Synthesis Method	Significant Findings	Ref
<b>WO<sub>3</sub>/TNTA nanocomposite</b>	Electrochemical deposition	The maximum conversion efficiency of 0.87% was obtained for WO <sub>3</sub> /TNTA nano-composite. H <sub>2</sub> and O <sub>2</sub> gases were collected during the photoreaction were had the volume ratio of 2.2:1 volume ratio.	[19]
<b>W-Doped TNTA</b>	A direct anodization	Showed that photocurrent densities of 3 wt% W-doped TNTA which were obtained were 0.25 mA/cm <sup>2</sup> at 1 V bias, which is much higher than that of the undoped sample.	[20]
<b>WO<sub>3</sub>/TNTA nanocomposite</b>	A facile hydrothermal method	Exhibited enhanced photocatalytic activity toward Rhodamine B (RhB) degradation when compared with pure TNTA and P25. The optimum percentage of WO <sub>3</sub> decorated on TNTA for the improvement of photocatalytic properties is 5 wt. %.	[21]
<b>WO<sub>3</sub>-TNTA</b>	A sol-gel template technique	Samples exhibited a strong photoresponse in the visible region and a low PL emission. High efficiency of 2,3-dichlorophenol degradation was obtained under visible light.	[22]
<b>W doped TNTA</b>	An anodization of Ti-W alloys	The content of 9 at% WO <sub>3</sub> in photoresponse experiments is most beneficial, in long term experiments a higher efficiency is observed for the 0.2 at% W content.. This demonstrates that under optimized WO <sub>3</sub> doping conditions a lasting visible light activation of TiO <sub>2</sub> nanotubes can be achieved.	[23]
<b>W-TNTA</b>	A radio-frequency (RF) sputtering	The effect of W on the photoelectrochemical properties of TNTA was due to W atoms which occupy the substitutional position within the vacancies of TNTA. Found the W-TNTA system plays important roles in efficient electron transfers due to the reduction in e <sup>-</sup> /h <sup>+</sup> recombination.	[24]
<b>WO<sub>3</sub>-TNTA</b>	A wet impregnation	A maximum photocurrent of 2.1 mA/cm <sup>2</sup> with a photoconversion efficiency of 5.1% was obtained, which is approximately twice higher than that of pure TiO <sub>2</sub> nanotubes. The findings were mainly attributed to higher charge carrier separation, which minimized the recombination losses and enhanced the transportation of photo-induced electrons in this binary hybrid photoelectrode.	[25]
<b>WO<sub>3</sub>-TNTA</b>	A wet impregnation	A low content of WO <sub>3</sub> species successfully diffused into the TiO <sub>2</sub> lattice and formed W-O-Ti bonds, which significantly promoted effective charge separation by trapping photo-induced electrons from TiO <sub>2</sub> . The photocurrent density, photoconversion efficiency, STH efficiency, and H <sub>2</sub> generation of the resultant hybrid nanotubes were increased.	[26]
<b>WO<sub>3</sub>-TNTA</b>	A wet impregnation	In PEC studies, high-crystallinity anatase-phase WTNs exhibited a higher photocurrent density (2.4 mA/cm <sup>2</sup> ) than WTNs of amorphous or polycrystalline phases.	[27]
<b>WO<sub>3</sub>/TiO<sub>2</sub> heterojunction</b>	Liquid phase deposition	TiO <sub>2</sub> film provides an excellent platform for WO <sub>3</sub> deposition. WO <sub>3</sub> expands the absorption band edge of TiO <sub>2</sub> film to visible light region. WO <sub>3</sub> /TiO <sub>2</sub> heterojunction film shows high photoelectrocatalytic activity.	[28]
<b>WO<sub>3</sub>-loaded TiO<sub>2</sub> nanotube</b>	tungsten as the cathode	WO <sub>3</sub> -loaded TiO <sub>2</sub> nanotube arrays with the highest aspect ratio, geometric surface area factor and at% of tungsten exhibited the more favorable photocatalytic degradation of MO dye under UV light irradiation	[29]

**Table 2 :** Electrodeposition and calcinations conditions of tungsten oxide on TNTA electrodes.

Electrodeposition Bath	Deposition Temperature	Electrodes Configuration	Calcination Conditions	Ref.
<ul style="list-style-type: none"> <li>• 0.2M of Sodium tungstate (<math>\text{Na}_2\text{WO}_4</math>, 99%, Merck)</li> <li>• 0.13M of Hydrogen Peroxide Solution (<math>\text{H}_2\text{O}_2</math>, 30%, Sigma-Aldrich) and</li> <li>• drops of Sulfuric acid (<math>\text{H}_2\text{SO}_4</math>, 70%, Merck)</li> </ul>	23-25 °C	Anode: Long-TNTA (LTNTA) & Short-TNTA (STNTA) Cathode: Pt Reference: Ag/AgCl	350 °C for 30 min in purified air	Krasnov and Kolbasov [33]

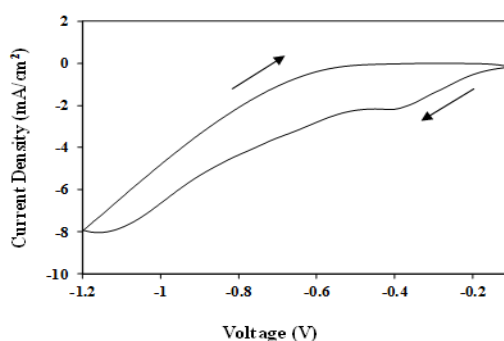


**Figure 1:** Cyclic voltammogram of TNTA electrode in 0.2M  $\text{Na}_2\text{WO}_4$ , 0.13M  $\text{H}_2\text{O}_2$  electrolyte.

The post-treatment process of the TNTA prepared above involved annealing, which is a vital step for the transformation of the amorphous state of titanium oxide into anatase crystals. Prior to annealing, the surface of the anodized samples was cleaned with deionized water to remove ionic residues, and the samples were dried under  $\text{N}_2$  flow at 100 °C for 12 hr. The TNTA samples were loaded in to a muffle furnace in a ceramic boat and were annealed at 500 °C for 3 hr in  $\text{N}_2$  flow. The temperature was increased at a rate of 5 °C/min.

The synthesized photoanodes were characterized by field emission scanning electron microscope (FESEM), energy dispersive X-ray (EDX), X-ray photoelectron spectrometer (XPS), X-ray diffraction (XRD) and ultraviolet and visible light (UV-VIS) spectroscopy. Photoelectrochemical data of the photoanodes were collected by using the in-house PEC system [34, 35] and the results were discussed in comparison with undoped TNTA.

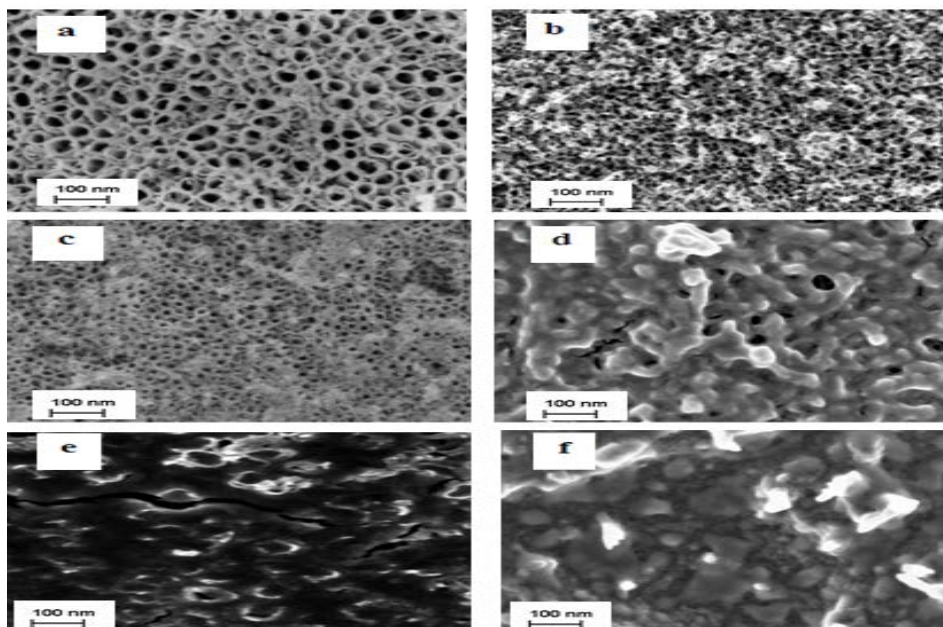
### 3. Results and Discussion

Figure 2 and Figure 3 show the morphology (FESEM top-view) of the STNTA and LTNTA with  $\text{WO}_3$  deposit, respectively. It can be seen that  $\text{TiO}_2$  tubes are covered with a very thin layer of  $\text{WO}_3$

started to form and became much thicker as the deposition period became longer (Figure 2c and 3c). However, in most cases the surface area shows open and nicely decorated tubes with small individual  $WO_3$  nanoparticles (diameter of  $\sim 5$  nm) was visible for 5 minutes deposition period and became larger (agglomeration) as the deposition time getting longer until a thick layer was formed as shown in Figure 2e & f and 3f. The EDX result is represented and it clearly indicates that W is present (Table 3) in the particles.

**Table 3:** Elemental Composition of  $WO_3$ /TNTA at different deposition periods.

Deposition Time (min)	Elemental content (Atomic %)							
	$WO_3$ /STNTA				$WO_3$ /LTNTA			
	Ti	O	C	W	Ti	O	C	W
1	35.38	64.57	-	0.04	41.69	51.08	7.13	0.11
5	37.96	61.88	-	0.16	37.07	59.09	3.61	0.23
10	38.69	61.05	-	0.26	28.89	57.02	13.82	0.28
15	57.41	42.19	-	0.40	26.55	55.32	17.68	0.45
30	51.26	47.73	-	1.01	30.72	59.61	9.01	0.66
45	32.60	60.58	-	6.823	26.45	65.04	5.77	2.74



**Figure 2:** FESEM top view of  $WO_3$ /STNTA at variety deposition time: (a) 1, (b) 5, (c) 10, (d) 15, (e) 30, and (f) 45 minutes.

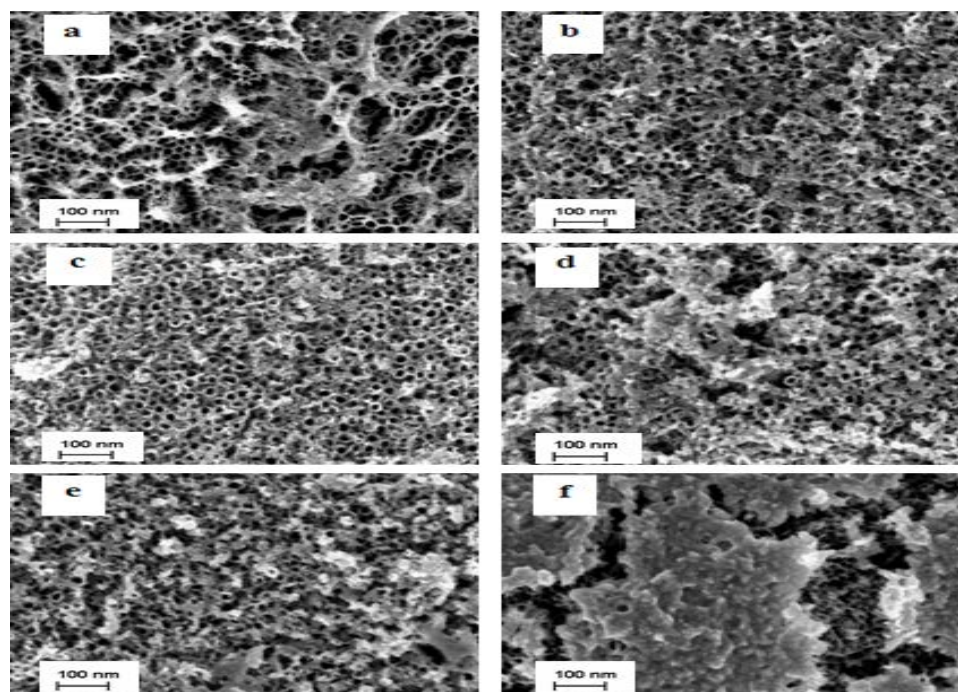


**Figure 3:** FESEM top view of  $\text{WO}_3/\text{LTNTA}$  at selection deposition time: (a) 1, (b) 5, (c) 10, (d) 15, (e) 30, and (f) 45 minutes.

For  $\text{WO}_3$ -TNTA nanocomposite electrode, the content existences of deposited  $\text{WO}_3$  nanoparticles on short and long TNTA were studied by XRD measurement. The XRD patterns for  $\text{WO}_3$ -STNTA and  $\text{WO}_3$ -LTNTA are depicted in Figure 4a & b, respectively. Previous investigations on bulk  $\text{WO}_3$  have reported the following phase transformation sequence upon heating: triclinic ( $\delta$ - $\text{WO}_3$ ) ( $-30^\circ\text{C}$ )  $\rightarrow$  monoclinic ( $\gamma$ - $\text{WO}_3$ ) ( $330^\circ\text{C}$ )  $\rightarrow$  orthorhombic ( $\beta$ - $\text{WO}_3$ ) ( $740^\circ\text{C}$ )  $\rightarrow$  tetragonal ( $\alpha$ - $\text{WO}_3$ ) [36]. In this work, the XRD patterns (Figure 4a & b) show diffraction signals for the monoclinic  $\text{WO}_3$  under the conditions (JCPDS No.83-950), indicating a desirable crystallinity was formed in the nanocomposite sample after calcinations at  $350^\circ\text{C}$  [37]. As shown in Figure 4a & b, there was no new diffraction peak can be ascribed to the crystal phase of  $\text{W}_x\text{Ti}_{1-x}\text{O}_2$  for the calcination temperatures used in this study which can be concluded that no reaction between oxides. The nanocomposite show sharp diffraction peaks at  $34.0^\circ$  (202),  $49.0^\circ$  (004), and  $55.3^\circ$  (024), for  $\text{WO}_3/\text{LTNTA}$ 's XRD spectrum which were similar to those detected by Lai and Sreekantan [25].

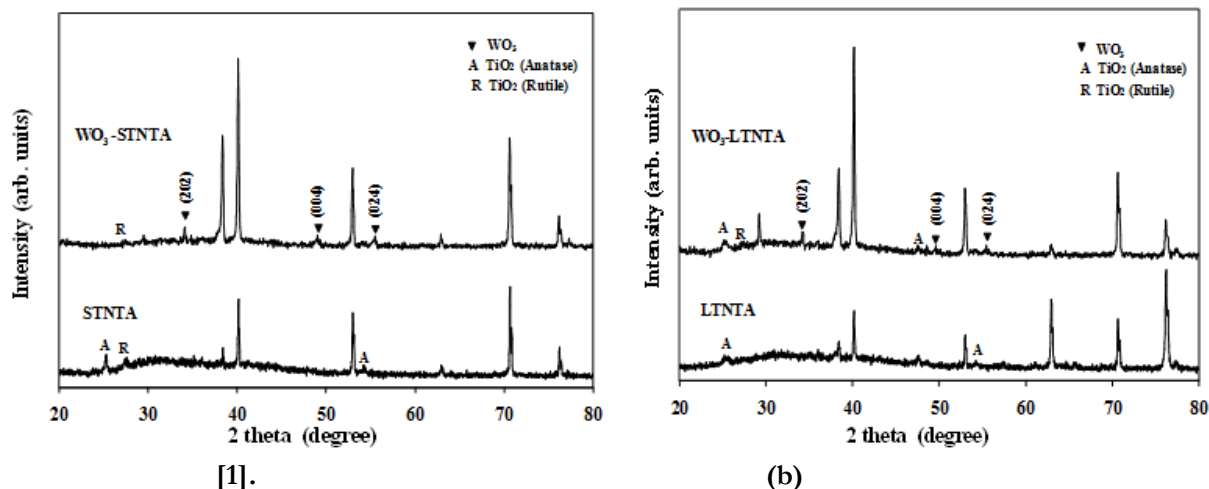


Figure 4: X-ray diffraction patterns of (a)  $WO_3/STNTA$  and (b)  $WO_3/LTNTA$ .

However, the peak at  $30^\circ$  was unknown. The XRD profiles of  $WO_3/LTNTA$  became stronger and sharper than  $WO_3/STNTA$  because most of the deposited  $WO_3$  nanoparticles were formed on the surface of the LTNTA (due to smaller tube diameter) but the particles were deposited in the tubes and on the surface (due to big diameter) of the STNTA. The reflectance (R %) of  $WO_3/TNTA$  nanocomposites were measured using UV-VIS spectroscopy, and the reflectance spectra are shown in Figure 5. The transmittances were almost zero due to the Ti base. The intensity of the reflectance depends on the morphology and amount of metal oxide formed on the surface. Besides absorption by the deposited nanoparticles, the detected scattering of light was very weak due to the morphological structure of tubes which absorbs the scattering light. The fluctuation of reflectance was strong in 1- $WO_3/TNTA$  samples in the visible region (400 to 800 nm) for one min deposition period as shown in Figure 6. This is due to the small amount of  $WO_3$  content. The  $WO_3/TNTAs$  with different  $WO_3$  contents were used as photoelectrodes in PEC water-splitting cell for evaluation of their photocurrent densities production. The photocurrent density-voltage response was plotted under  $100 \text{ W/m}^2$  illuminations. The corresponding experimental results are presented in Figure 6a & b for  $WO_3/STNTA$  and  $WO_3/LTNTA$  respectively for different deposition periods. The maximum photocurrent densities of 0.3 and  $0.37 \text{ mA/cm}^2$  were observed at 1 V vs. SCE in the 10- $WO_3/STNTA$  and 15- $WO_3/LTNTA$  with 0.16 and 0.45 at% of W content respectively, which is relatively higher compared with that of the pure STNTA and LTNTA ( $0.06$  and  $0.32 \text{ mA/cm}^2$  at 1 V vs. SCE, respectively). The  $WO_3/STNTA$  prepared by deposition for 1, 5, 15, 30 and 45 min exhibited decreased photocurrent densities of approximately 0.1, 0.18, 0.17, 0.14 and  $0.12 \text{ mA/cm}^2$  at 1 V vs. SCE, respectively. It is noted that  $WO_3/LTNTA$  photoanodes which were deposited for 1, 5, 10, 30 and 45 min produced photocurrent densities about 0.19, 0.26, 0.33, 0.22 and  $0.09 \text{ mA/cm}^2$  at 1 V vs. SCE, respectively. These results clearly showed the significant effects of different  $WO_3$  contents in the TNTA on the PEC performances. The resultant photocurrent densities of  $WO_3/STNTA$  increased linearly as shown in Figure 6a. Moreover in Figure 6b, the photocurrent

densities of  $\text{WO}_3/\text{LTNTA}$  at 1, 15 and 45 min deposition periods were mostly constant, and the other curves were increased slightly in logarithmic shape.

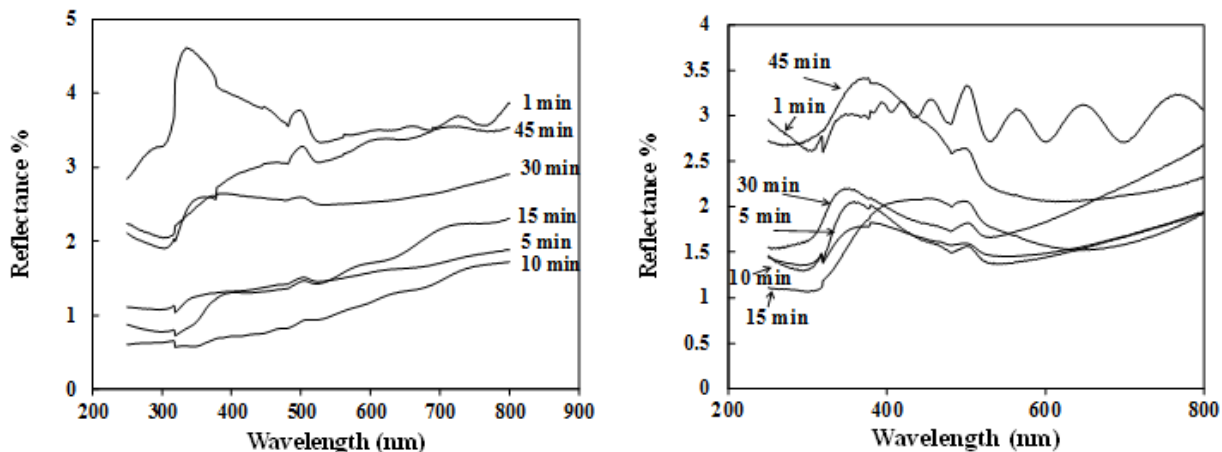


Figure 5: Reflectance spectra of  $\text{WO}_3/\text{STNTA}$  (left) and  $\text{WO}_3/\text{LTNTA}$  (right) at various deposition periods.

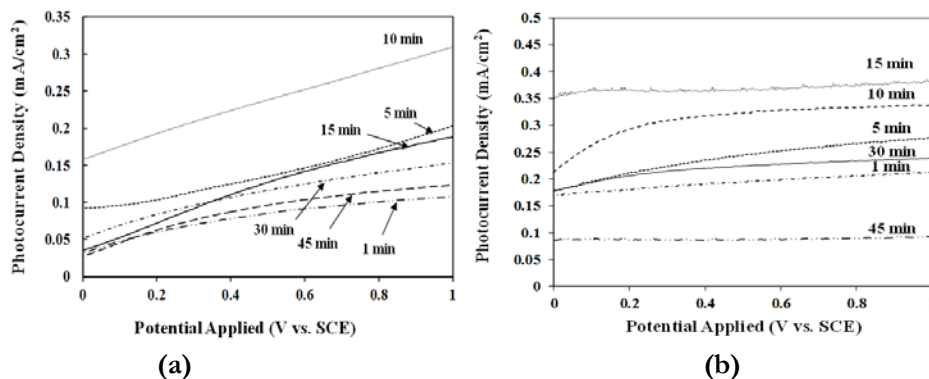
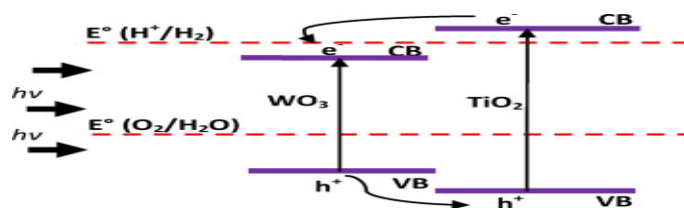


Figure 6: Photocurrent density as a function of measured potential (vs. SCE) for a)  $\text{WO}_3/\text{STNTA}$  and b)  $\text{WO}_3/\text{LTNTA}$  photoelectrodes deposited at different deposition period under light illumination.

Figure 7 was illustrated the predicted mechanism of electrons movement in  $\text{WO}_3/\text{TNTA}$  photoelectrodes. Composite  $\text{WO}_3$  and TNTA materials have shown a favorable electron injection from the CB of TNTA to that of  $\text{WO}_3$  and hole transfer between VBs in the opposite direction, which reduces  $e^-/h^+$  recombination in both semiconductors. The CB of  $\text{WO}_3$  is not negative enough for water reduction, some modifications are needed to achieve  $\text{H}_2$  evolution. Also  $\text{WO}_3/\text{TNTAs}$  have a higher UV response compared to  $\text{WO}_3$  materials. This is improvement could be attributed in part to better absorption and better transport due to the organized nanostructures. In addition, the electron transfer from TNTA to  $\text{WO}_3$  results in a wide electron-hole separation, which could improve the IPCE values as well



**Figure 7:** Schematic diagram showing the energy band position and the electron transfer direction for WO<sub>3</sub>/TNTA nanocomposite electrode after being excited by light.

#### 4. Conclusions

This work was focused on the synthesis, characterization, PEC testing of hetero-nanocomposite TNTA semiconductors with WO<sub>3</sub> nanoparticles. However, getting the best performance for the photoelectrochemical testings for electrodes were quite difficult since it was influenced by the stability and the ability of the electrodes to produce photocurrent. However, short and long TNTA synthesized by anodization of Ti-foil in two types of electrolytes (acidic and organic) lead to synthesis two different morphologies of TNTA. Subsequently, Metal oxides nanoparticles (WO<sub>3</sub>) which has a small band gap were deposited on TNTA individually from sodium tungstate aqueous solution at room temperature. The morphologies of deposited WO<sub>3</sub> on TNTA varied depending on deposition periods and crystal type. Similarly, the content of WO<sub>3</sub> on TNTA increased upon electrodeposition period according to EDX results. Likewise, for WO<sub>3</sub>/STNTA and WO<sub>3</sub>/LTNTA the maximum photocurrent were 0.3 mA at 10 minutes and 0.37 mA at 15 minutes, respectively.

#### Acknowledgment

The authors express their sincere thanks to Universiti Kebangsaan Malaysia for allowing this work to use the UKM-GUP-BTT-07-30-190, UKM-OUP-TK-16-73/2010 and UKM-OUP-TK-16-73/2011 research grants. A.M.H. Milad thanks the Elmergib University.

#### References

- [1]. M. Gratzel. "Photoelectrochemical cells". *Nature*, vol.414, pp. 338-344. 2001
- [2]. H. Wang and J. P. Lewis. "Second-generation photocatalytic materials: aniondoped TiO<sub>2</sub>". *Journal of Physics: Condensed Matter*, vol.18, pp. 421-434. 2006
- [3]. A. Fujishima and K. Honda. "Electrochemical photolysis of water at a semiconductor electrode". *Nature*, vol.238, pp. 37-38. 1972
- [4]. O. Khaselev and J. A. Turner. "A monolithic photovoltaic-photoelectrochemical device for hydrogen production via water splitting". *Science*, vol.280, pp. 425-427. 1998
- [5]. A. J. Bard and M. A. Fox. "Artificial Photosynthesis: Solar Splitting of Water to Hydrogen and Oxygen". *Accounts of Chemical Research*, vol.28, pp. 141-145. 1995
- [6]. M. Spichiger-Ulmann and J. Augustynski. "Aging effects in n-type semiconducting WO<sub>3</sub> films". *Journal of Applied Physics*, vol.54, pp. 6061-6064. 1983
- [7]. W. Erbs; J. Desilvestro; E. Borgarello; and M. Gratzel. "Visible-light-induced oxygen generation from aqueous dispersions of tungsten(VI) oxide". *Journal of Physical Chemistry B*, vol.88, pp. 4401-4006. 1984

- [8]. H. Ali; N. Ismail; M. S. Amin; and M. Mekewi. "Decoration of vertically aligned TiO<sub>2</sub> nanotube arrays with WO<sub>3</sub> particles for hydrogen fuel production". *Frontiers in Energy*, vol.12, pp. 249–258. 2018
- [9]. I. Shiyanovakaya and M. Hepel. "Bicomponent WO<sub>3</sub>/TiO<sub>2</sub> Films as Photoelectrodes". *Journal of Electrochemical Society*, vol.146, pp. 243-249. 1999
- [10]. S. Higashimoto; N. Kitahata; K. Mori; and M. Azuma. "Photo-electrochemical properties of amorphous WO<sub>3</sub> supported on TiO<sub>2</sub> hybrid catalysts". *Catalysis Letters*, vol.101, pp. 49-51. 2005
- [11]. H. Tada; A. Kokubu; M. Iwasaki; and S. Ito. "Deactivation of the TiO<sub>2</sub> photocatalyst by coupling with WO<sub>3</sub> and the electrochemically assisted high photocatalytic activity of WO<sub>3</sub>". *Langmuir*, vol.20, pp. 4665-4670. 2004
- [12]. C. S. Fu; C. Lei; G. Shen; and C. G. Yu. "The preparation of coupled WO<sub>3</sub>/TiO<sub>2</sub> photocatalyst by ball milling". *Powder Technology*, vol.160, pp. 198-202. 2005
- [13]. J. Engweiler; J. Harf; and A. Baiker. "WO<sub>x</sub>/TiO<sub>2</sub> catalysts prepared by grafting of tungsten alkoxides: Morphological properties and catalytic behavior in the selective reduction of NO by NH<sub>3</sub>". *Journal of Catalysis*, vol.159, pp. 259-269. 1996
- [14]. S. Eibl; B. C. Gates; and H. Knözinger. "Structure of WO<sub>x</sub>/ZrO<sub>2</sub> Catalysts Prepared from Hydrous Titanium Oxide Hydroxide: Influence of Preparation Parameters". *Langmuir*, vol.17, pp. 107-115. 2001
- [15]. H. M. Yang; R. R. Shi; K. Zhang; Y. Hu; A. Tang; and X. Li. "Synthesis of WO<sub>3</sub>/TiO<sub>2</sub> nanocomposites via sol-gel method". *Journal of Alloys and Compounds*, vol.398, pp. 200-202. 2005
- [16]. D. Ke; H. Liu; T. Peng; X. Liu; and K. Dai. "Preparation and photocatalytic activity of WO<sub>3</sub>/TiO<sub>2</sub> nanocomposite particles". *Materials Letters*, vol.62, pp. 447-450. 2008
- [17]. P. K. Shin and A. C. C. Tseung. "Study of Electrodeposited Tungsten Trioxide Thin Films". *Journal of Materials Chemistry*, vol.2, pp. 1141-1148. 1992
- [18]. X. Z. Li; F. B. Li; C. L. Yang; and W. K. Ge. "Photocatalytic activity of WO<sub>x</sub>-TiO<sub>2</sub> under visible light irradiation". *Journal of Photochemistry and Photobiology A: Chemistry*, vol.141, pp. 209-217. 2001
- [19]. J. H. Park; O. O. Park; and S. Kim. "Photoelectrochemical water splitting at titanium dioxide nanotubes coated with tungsten trioxide". *Applied Physics Letters*, vol.89, pp. 163106-163109 2006b
- [20]. J. Zhao; X. Wang; Y. Kang; X. Xu; and Y. Li. "Photoelectrochemical Activities of W-Doped Titania Nanotube Arrays Fabricated by Anodization". *IEEE Photonics Technology Letters*, vol.20, pp. 1213-1215. 2008
- [21]. M. Xiao; L. Wang; X. Huang; Y. Wu; and Z. Dang. "Synthesis and characterization of WO<sub>3</sub>/titanate nanocomposite with enhanced photocatalytic properties". *Journal of Alloys and Compounds*, vol.470, pp. 486-491. 2009
- [22]. E.-l. Yang; J.-j. Shi; H.-c. Liang; and W.-k. Cheuk. "Coaxial WO<sub>3</sub>/TiO<sub>2</sub> nanotubes/nanorods with high visible light activity for the photodegradation of 2,3-dichlorophenol". *Chemical Engineering Journal*, vol.174, pp. 539-545. 2011
- [23]. C. Das; I. Paramasivam; N. Liu; and P. Schmuki. "Photoelectrochemical and photocatalytic activity of tungsten doped TiO<sub>2</sub> nanotube layers in the near visible region". *Electrochimica Acta*, vol.56, pp. 10557-10561. 2011
- [24]. C. W. Lai and S. Sreekantan. "Visible light photoelectrochemical performance of W-loaded TiO<sub>2</sub> nanotube arrays: structural properties". *Journal of Nanoscience and Nanotechnology*, vol.12, pp. 3170-4. 2012
- [25]. C. W. Lai and S. Sreekantan. "Incorporation of WO<sub>3</sub> species into TiO<sub>2</sub> nanotubes via wet impregnation and their water-splitting performance". *Electrochimica Acta*, vol.87, pp. 294–302. 2013a
- [26]. C. W. Lai and S. Sreekantan. "Preparation of hybrid WO<sub>3</sub>-TiO<sub>2</sub> nanotube photoelectrodes using anodization and wet impregnation: Improved water-splitting hydrogen generation performance". *International Journal of Hydrogen Energy*, vol.38, pp. 2156-2166. 2013b

- [27]. C. W. Lai and S. Sreekantan. "Effect of heat treatment on WO<sub>3</sub>-loaded TiO<sub>2</sub> nanotubes for hydrogen generation via enhanced water splitting". *Materials Science in Semiconductor Processing*, vol.16, pp. 947-954. 2013c
- [28]. M. Zhang; C. Yang; W. Pu; Y. Tan; K. Yang; and J. Zhang. "Liquid phase deposition of WO<sub>3</sub>/TiO<sub>2</sub> heterojunction films with high photoelectrocatalytic activity under visible light irradiation". *Electrochimica Acta*, vol.148, pp. 180-186. 2014
- [29]. W. H. Lee; C. W. Lai; and S. B. A. Hamid. "One-Step Formation of WO<sub>3</sub>-Loaded TiO<sub>2</sub> Nanotubes Composite Film for High Photocatalytic Performance". *Materials*, vol.8, pp. 2139-2153. 2015
- [30]. V. K. Mahajan; S. K. Mohapatra; and M. Misra. "Stability of TiO<sub>2</sub> nanotube arrays in photoelectrochemical studies". *International Journal of Hydrogen Energy*, vol.33, pp. 5369-5374. 2008
- [31]. Z. B. Xie; S. Adams; and D. J. Blackwood. "Effects of anodization parameters on the formation of titania nanotubes in ethylene glycol". *Electrochimica Acta*, vol.56, pp. 905-912. 2010
- [32]. F. ShafiaHoor; V. S. Murulidharan; M. F. Ahmed; and S. M. Mayanna. "Study In The Electrochemical Behavior Of Wo<sub>3</sub>-Pt Coating: A Cyclic Voltammetric Approach". *IOSR Journal of Applied Chemistry (IOSRJAC)*, vol.1, pp. 09-14. 2012
- [33]. Y. S. Krasnov and G. Y. Kolbasov. "Electrochromism and reversible changes in the position of fundamental absorption edge in cathodically deposited amorphous WO<sub>3</sub>". *Electrochimica Acta*, vol.49, pp. 2425-2433. 2004
- [34]. L. J. Minggu; W. R. Wan Daud; and M. B. Kassim. "An overview of photocells and photoreactors for photoelectrochemical water splitting". *International Journal of Hydrogen Energy*, vol.35, pp. 5233-5244. 2010
- [35]. K. Shankar; K. Tep; G. K. Mor; and C. A. Grimes. "An electrochemical strategy to incorporate nitrogen in nanostructured TiO<sub>2</sub> thin films: modification of bandgap and photoelectrochemical properties". *Journal of Physic D*, vol.39, pp. 2361-2366. 2006
- [36]. T. Vogt; P. Woodward; and B. Hunter. "The high-temperature phases of WO<sub>3</sub>". *Journal of Solid State Chemistry*, vol.144, pp. 209-215. 1999
- [37]. W. Li; J. Li; X. Wang; J. Ma; and Q. Chen. "Photoelectrochemical and physical properties of WO<sub>3</sub> films obtained by the polymeric precursor method". *International Journal of Hydrogen Energy*, vol.35, pp. 13137-13145. 2010

## Modeling the Effect of CO<sub>2</sub> on Thermodynamic Behavior of CO<sub>2</sub>/Libyan Natural Gas Mixture

Almadi A. Alhwaige<sup>1</sup>, Ali S. Ebshish<sup>2</sup>, Salem M. Abdusalam<sup>3</sup>, Ahmed M. Bshish<sup>4</sup>

Department of Chemical and Petroleum Engineering, College of Engineering, Elmergib University, Alkhoms, Libya  
<sup>1</sup>aaa148@case.edu ; <sup>2</sup>asbshish@elmergib.edu.ly; <sup>3</sup>ansalem01@yahoo.co.uk; <sup>4</sup>ahmedbshish@gmail.com

### ABSTRACT

A great challenge has been done for utilization of natural gas (NG) for potential applications at various operating conditions. Accurate thermo-physical properties of NG play an important role in design and processing of NG systems. Among of these properties, compressibility factor, density, and viscosity of gas mixtures provide the feasibility of a given process. Carbon dioxide (CO<sub>2</sub>) is present in large quantities that produced from NG reservoirs. Understanding the effect of CO<sub>2</sub> on thermodynamic properties of Libyan NG is important for developing the next generation of modern applications. The major thermodynamic properties considered in the present study were compressibility factor, density, and viscosity. The objective of this work is to investigate the effect of CO<sub>2</sub> content on properties of Libyan NG using theoretical calculations. MATLAB logarithms were developed to predict the thermo-physical properties of Libyan NG with different CO<sub>2</sub> concentrations. The effect of CO<sub>2</sub> on thermodynamic behavior of NG mixture under different conditions of pressure and temperature was studied using the Redlich Kwong equation of state (RK-EoS). CO<sub>2</sub> concentration has a great impact on the CO<sub>2</sub>/NG mixture properties. The results revealed that the compressibility factor of CO<sub>2</sub>/NG mixture is inversely proportional with the CO<sub>2</sub> concentration; however, as CO<sub>2</sub> content increases the gas mixture density increases.

**Keywords:** Libyan natural gas; Carbon dioxide; Thermodynamic Properties; z-factor; Gas density; Viscosity of gas mixture.

### 1. Introduction

Since many decades, the world depends strongly on the natural gas (NG) as a major source for energy supply. The main challenge for using this energy for wide different applications is how to utilize and process the NG from its reservoir to the place where the energy needed. The key role in designing and processing of NG system is to identify its accurate thermo-physical properties. The most important gas mixture properties in the design calculations are compressibility factor, viscosity and density of the gas mixture [1-4].

In particular, compressibility factor is a measure of the gas deviation from perfect behavior and is defined as the ratio of the real gas volume to the ideal volume [1,2]. In simple way, the density is equal to number of molecules multiply molecular weight over the occupied volume. The viscosity is the fluid (Liquid or Gas) property of resistance to flow and may be thought of as a measure of fluid friction [2].

Viscosity and density are essential physical quantities to describe the statics and dynamics behaviors of gas mixtures. These properties only can describe more than half of the fluid properties [2].

Gathering density and viscosity data on a NG gives manufacturers the ability to predict how it behaves in the real world. Availability of these properties provide analog for good concertation of NG transportation systems and contribute for excellent design processes with high production [4].

In the most cases, NG often contains some amounts of heavier hydrocarbons and non-hydrocarbons (impurities), which have a significant contribution to change the thermodynamic behavior of the NG [3]. In case of enhanced oil recovery (EOR) process, carbon dioxide (CO<sub>2</sub>) is widely used as injected gas to the gas-oil reservoirs for increasing the reservoir pressure. The injected CO<sub>2</sub> will mix with the NG/oil; therefore, the thermodynamic properties of these products are directly affected due to the change of CO<sub>2</sub> concentration in the products. Hence, effect of CO<sub>2</sub> on densities and viscosities of gas mixtures is considered very important [5].

Generally, the thermodynamic properties are obtained experimentally and theoretically. Equations of state (EoSs) and empirical correlations are considered the common methods to predict thermodynamic behaviors of NG when unavailable experimental data. In addition, analytical methods are more attractive than experimental work because experiments are expensive, time consuming, and sometimes are not applicable [6,7]. Previously, we reported a study for fitting the equations of state for predicting the thermodynamic properties of Libyan NG mixture [1]. The results revealed that the Redlich Kwong cubic equation of state (RK-EoS) provides a better fit to Standing and Katz chart (K-Z). Therefore, in this study, Redlich Kwong (RK) was used as the model for predicting the NG properties. The objective of the present work is to investigate the effect of CO<sub>2</sub> composition on the viscosity and density of the Libyan NG mixture at different range of temperatures and pressures.

## 2. Theory

Cubic equations of state (EoSs) are the simplest models that predicting the PVT behavior of fluids (liquid and gases) with a broad range of temperatures and pressures. Many forms of equations of state have been used to predict NG compressibility factor (z-factor) and consequently the other gas properties such as viscosity and density [1].

The general form of the cubic equation of states is given in Eq.1. The solution of this equation provides three different complex roots for molar volume. However, the disadvantage of this form is that it can be solved only by trial and error method. However, it was difficulty of guessing the initial value of molar volume for the trial and error method. Therefore, the modern form of the equations of state have was obtained by replacing the molar volume parameter with z-factor according to the relationship that is given in Eq.2. Eq. 3 shows the final version of the general form of the modern EoSs. Table 1 illustrates the parameters that presented in Eq.3 belong to the most widely used EoSs [1].

$$V = \frac{RT}{P} + b - \frac{a(T)}{P} \frac{V - b}{(V + \epsilon b)(V + \sigma b)} \quad (1)$$

$$V = \frac{ZRT}{P} \quad (2)$$

$$Z = 1 + \beta - q\beta \frac{Z - \beta}{(Z + \epsilon\beta)(Z + \sigma\beta)} \quad (3)$$

$$\beta = \Omega \frac{P_r}{T_r} \quad (4)$$

$$q = \frac{\Psi \alpha(T_r)}{\Omega T_r} \quad (5)$$

Where  $P_r$  and  $T_r$  are reduced pressure and temperature of pure components, respectively. The expression  $\alpha(T_r)$  is a function in  $T_r$  and  $\omega$ . The numerical assignments for parameters  $\Sigma$ ,  $\sigma$ ,  $\Omega$ ,  $\omega$  and  $\Psi$  are depending on the type of EoS as shown in Table 1.

Table 1: Parameters assignments for generic EoS.

E.O.S.	$\alpha(T_r)$	$\Sigma$	$\epsilon$	$\Omega$	$\Psi$	$Z_c$
VdW	1	0	0	1/8	27/64	3/8
RK	$T_r^{-1/2}$	1	0	0.08664	0.42748	1/3
SRK	$\alpha_{SRK}(T_r; \omega)$	1	0	0.08664	0.42748	1/3
PR	$\alpha_{SRK}(T_r; \omega)$	$1 + \sqrt{2}$	$1 - \sqrt{2}$	0.07779	0.45724	0.30740

$$\alpha_{SRK}(T_r; \omega) = \left[ 1 + (0.480 + 1.574\omega - 0.176\omega^2)(1 - T_r^{1/2}) \right]^2$$

$$\alpha_{PR}(T_r; \omega) = \left[ 1 + (0.37464 + 1.54226\omega - 0.26992\omega^2)(1 - T_r^{1/2}) \right]^2$$

The gas density ( $\rho_g$ ) and viscosity ( $\mu_g$ ) of gas mixtures are defined as given in the following relations.

$$\rho_g = \frac{pM_g}{ZRT} \quad (6)$$

$$\mu_g = 1 * 10^{-4} k_v EXP \left[ x_v \left( \frac{\rho_g}{62.4} \right)^{\gamma_g} \right] \quad (7)$$

$$k_v = \frac{(9.4 + 0.02M_g)T^{1.5}}{209 + 19M_g + T} \quad (8)$$

$$x_v = 3.5 + \frac{986}{T} + 0.01M_g \quad (9)$$

Where,  $\rho_g$  is the density of the gas mixture in  $g/cm^3$ ,  $\mu_g$  is the viscosity in  $\phi$ ,  $M_g$  is the molecular weight of gas mixture, R is the universal gas constant,  $\gamma_g$  is the specific gravity for gas, and  $x_v$  is the parameter used to calculate  $\gamma_g$ .

### 3. Methodolog

In this work, the thermodynamic properties of compressibility factor, viscosity and density of Libyan NG were theoretically predicted. Table 2 list the used the data of Libyan NG, which was obtained

from Milletah Oil and Gas (MOG) Company. Matlab logarithm of Redlich Kwong equation (RK-EoS) was launched for predicting the z-factor, viscosity, and density of NG mixtures with different CO<sub>2</sub> compositions at various values of reduced temperatures and reduced pressures.

**Table 2:** The composition of gas mixture.

Component	Formula	Composition %
Hydrogen Sulphide	H <sub>2</sub> S	01.27
Carbon Dioxide	CO <sub>2</sub>	15.65*
Nitrogen	N <sub>2</sub>	04.59
Methane	C <sub>1</sub>	70.06
Ethane	C <sub>2</sub>	04.40
Propane	C <sub>3</sub>	01.76
i-Butane	i-C <sub>4</sub>	00.40
n-Butane	n-C <sub>4</sub>	00.67
i-Pentane	i-C <sub>5</sub>	00.30
n-Pentane	n-C <sub>5</sub>	00.30
n-Hexane	n-C <sub>6</sub>	00.29
n-Heptane	n-C <sub>7</sub>	01.80
n-Octane	n-C <sub>8</sub>	00.08
n-Nonane	n-C <sub>9+</sub>	00.02
Water	H <sub>2</sub> O	02.00

\*In this study, the CO<sub>2</sub> composition was changed, but the composition ratios of the other gases maintained constants.

In the initial step, the critical temperature ( $T_c$ ) and critical pressure ( $P_c$ ) for gas mixture were calculated using Eqs.10 and 11, respectively. Then, the reduced temperature ( $T_r$ ) and reduced pressure ( $P_r$ ) were evaluated using Eqs. 12 and 13, respectively.

$$T_c = \sum_{i=1}^n T_{ci} y_i \quad (10)$$

$$P_c = \sum_{i=1}^n P_{ci} y_i \quad (11)$$

$$T_r = \frac{T}{T_c} \quad (12)$$

$$P_r = \frac{P}{P_c} \quad (13)$$

Where  $P_{ci}$  and  $T_{ci}$  are the critical pressure and critical temperature of pure component  $i$ , respectively;  $y_i$  is the mole fraction of component  $i$ .  $T_r$  and  $P_r$  are reduced temperature and reduced pressure, respectively.  $T_c$  and  $P_c$  are critical temperature and critical pressure of the gas mixture, respectively.

The second step, the compressibility factor ( $Z$ ) was estimated using RK-EoS as given in Eq. 3. RK-EoS was found the best EoSs for prediction the compressibility factor of the Libyan gas mixture [1]. Finally, the density and viscosity of the gas mixture were predicted using Eqs. 6, and 7 respectively. Since the main objective of this study is to investigate the effect of  $\text{CO}_2$  composition in the NG properties, the composition of  $\text{CO}_2$  in the gas mixture was varied from 10 % to 50%. Besides, the densities and viscosities of these gas mixtures were evaluated at different temperatures and pressures.

## 4. Results and Discussion

### 4.1. Compressibility Factor

The compressibility factor as a function of reduced pressure and reduced temperature has been computed using Redlich Kwong equation of state (RK-EoS). The predicted results using RK-EoS were compared with the  $z$ -factor that previously obtained from Standing-Katz (S-K) chart and the results are shown in Figure 1.

The properties were evaluated at different reduced pressure ranging from 1 to 13, and at reduced temperatures of 1.5, 2, and 3. The S-K chart was used as a reference chart to examine the reliability of using RK-EoS in predicting the compressibility factor. As clearly seen from Figure 1, the behaviour of the compressibility factor that obtained using RK-EoS is in a good agreement with that obtained by S-K chart. As previously reported by Salem and his co-workers [1], among of the equations of state, RK-EoS showed the best fit to S-K chart to describe the Libyan NG behavior. Therefore, the RK-EoS was selected in this study for predicting the further thermodynamic properties of the gas mixture.

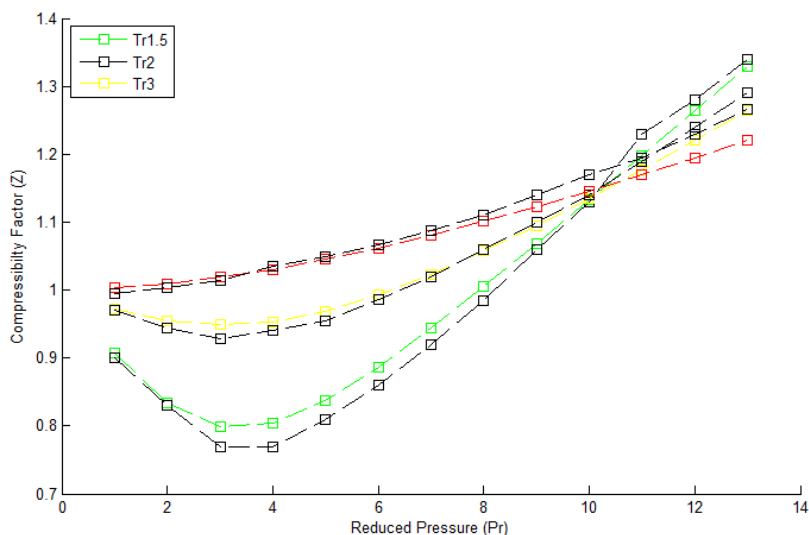


**Figure 1:** Effect of reduced temperature on the compressibility factor at various pressures: RK-EoS in coloured lines and S-K in Black lined [1].

### 4.2. Effect of $\text{CO}_2$ Concentration on the Viscosity of Gas Mixture

Viscosity of NG mixture is very important quantity for knowing how the production and transportation processes are designed. Pressure and temperature have great influence on the viscosity behavior of NG mixture. Viscosity of the gas mixture is evaluated using Eq.7 by applying the z-factor that obtained from RK-EoS. The composition of CO<sub>2</sub> in the gas mixture has been varied from 10% to 50% and for each case the viscosity was calculated. Figure 2 shows the viscosity of the NG mixtures with different CO<sub>2</sub> compositions at different reduced temperatures.

As seen in Figure 2, the results indicated that the viscosity of gas mixture increase with an increase in the amount of CO<sub>2</sub>. This finding is very important to take in account because the design of the production and transportation process strongly depends on determination of accurate value of viscosity. In addition, the results demonstrate that the viscosity of gas mixture is proportional with the reduced pressure. For example, at  $T_r = 1.25$ , the viscosity of the gas mixture was increased from 1 to 2.5 cp with an increase in the reduced pressure from 4 to 8. This seems to be quite logic because the viscosity dependent with the density, which is increased with the system pressure. Furthermore, it is clearly that all cases predicted that the viscosity have nonlinear relationship with the reduced pressure at the low values; however, it became nearly linear at high values of reduced pressure. Therefore, there is no effect of the reduced pressure at high reduced pressure values. On the other hand, the viscosity has inverse relationship with reduced temperature. Figure 3, displays the viscosity of gas as a function in the reduced temperatures at CO<sub>2</sub> composition of 0.1565. The results indicated that the viscosity has linearly proportional relationship at low reduced temperatures; however, it increases nonlinearly at high reduced temperature.

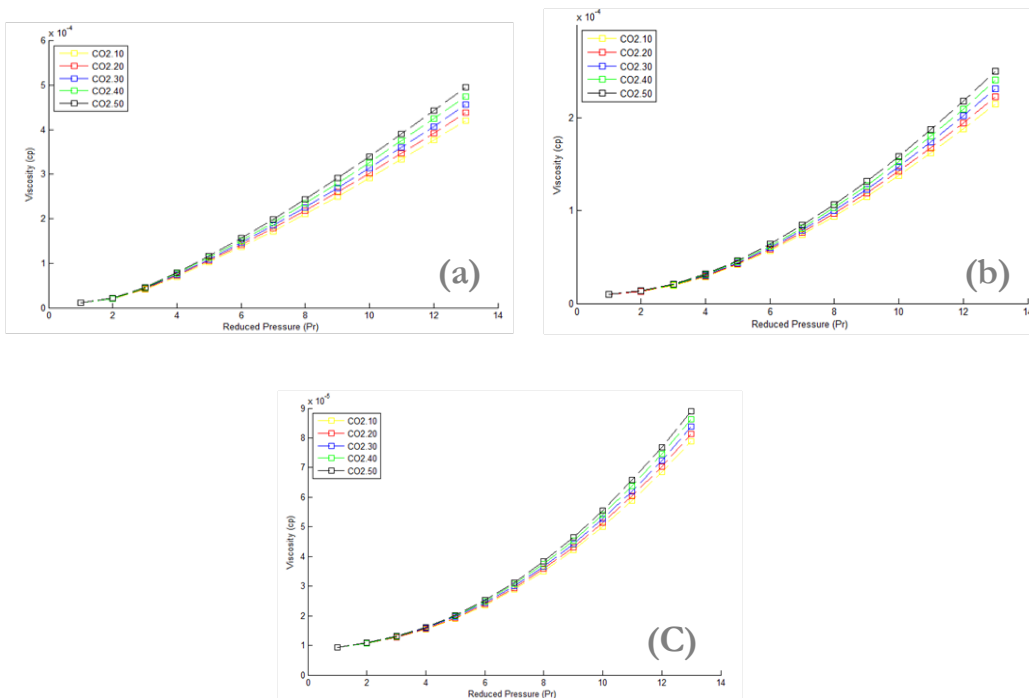


**Figure 2:** the effect of CO<sub>2</sub> on the viscosity of natural gas mixture at different reduced temperatures; (a) at  $T_r = 1.25$ , (b) at  $T_r = 1.5$ , and (c) at  $T_r = 2$ .

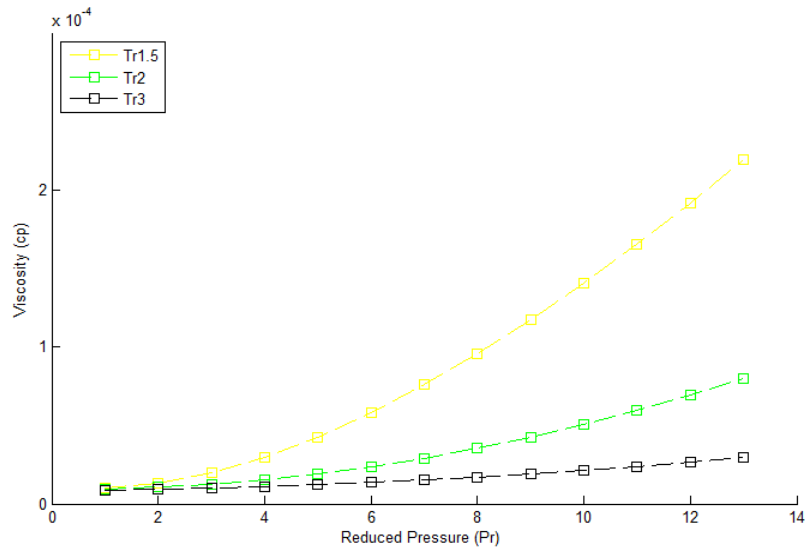


**Figure 3:** The viscosity of MOG gasmixture versus reduced pressure at different reduced temperatures.

#### 4.3. Effect of CO<sub>2</sub> Composition on the Density of Gas Mixture

In this part, the density of the gas mixture has been evaluated using Eq.6 with z-factor values obtained from RK-EoS. Figure 4 shows the effect of CO<sub>2</sub> composition on the density of the gas mixture at different reduced pressures and reduced temperatures. As seen in Figure 4, the density of the gas mixture doesn't remarkably change with varying CO<sub>2</sub> concentration in gas mixture. In addition, the behaviour of the gas density seems to be identical at all values of CO<sub>2</sub> compositions. However, the numerical values of the densities indicate that there is a slight increase in the gas density with increase the concentration of CO<sub>2</sub>.

Furthermore, Figure 4 shows that the gas density increases notably with increasing reduced pressure, especially at high reduced temperature. At low reduced temperature, the density was sharply increased at beginning and then, it became increased gradually to reach equilibrium. However, the density values increased linearly with reduced pressure. Figure 5 shows the effect of reduced temperature on the gas mixture at fixed CO<sub>2</sub> composition of 0.1565. The results showed that the density has an inverse relation with the reduced temperatures. For instant, the density values were read 5, 7, and 12 g/cm<sup>3</sup> for decreasing the reduced temperature as 1.25, 2.0, 3.0, respectively.

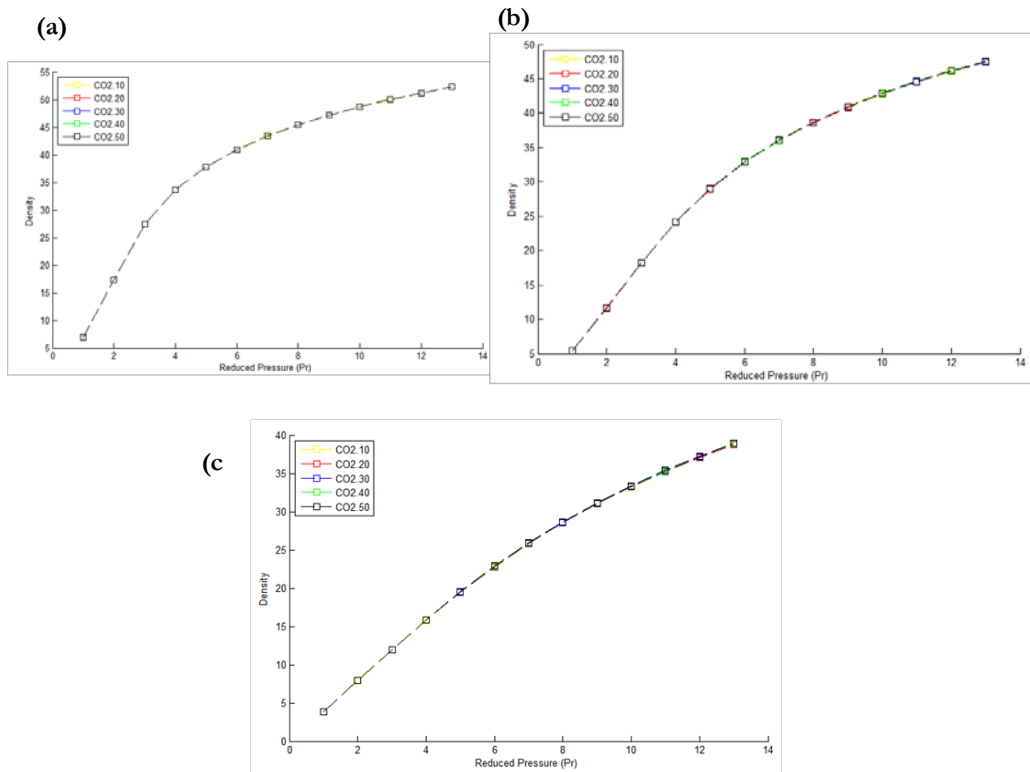


**Figure 4:** the effect of CO<sub>2</sub> Concentration on the density of natural gas mixture at different reduced temperatures; (a) at  $T_r = 1.25$ , (b) at  $T_r = 1.5$ , (c) at  $T_r = 2$ .

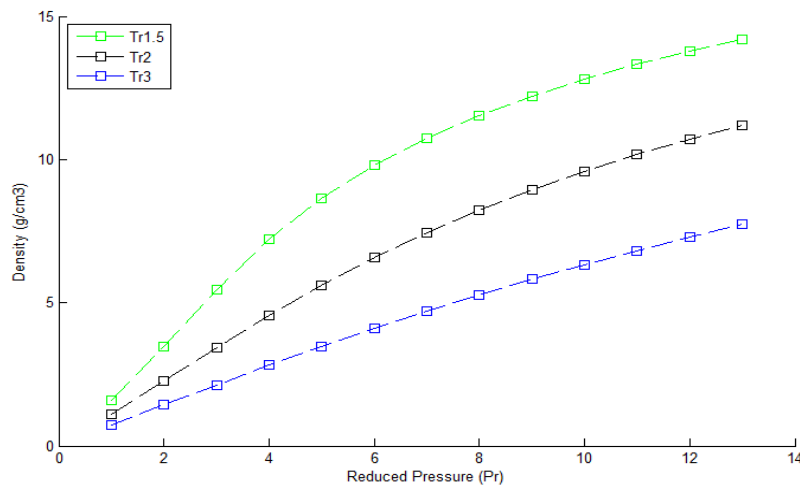


**Figure 5:** The density of MOG gas versus reduced pressure at different reduced temperatures.

## 5. Conclusions

Prediction of thermodynamic properties of Libyan NG under diverse conditions is very important in designing and processing of NG system. Among of these properties, density and viscosity have significant contribution to describe more than half of the other properties belong to gas mixtures.

Redlich Kwong equation of state (RK-EoS) was used in this work to investigate the effect of CO<sub>2</sub> composition in the Libyan NG mixture of MOG on its viscosity and density. The data of NG mixture with different compositions of CO<sub>2</sub> was correlated to RK-EoS to obtain the compressibility factor of the gas over a range of reduced pressures from 1 to 14 and reduced temperatures from 1.5 to 3. Then, the z-factor obtained from RK-EoS was used to predict the viscosity and density of the mixture over mentioned conditions. The results showed that the increase of CO<sub>2</sub> content in the gas mixture leads to an increase in the viscosity. It also revealed that the density of the mixture is slightly increased with the increase in the CO<sub>2</sub> content. This finding is very useful to gas manufacturers for better design of gas piping and storage system. Moreover, this study demonstrated that the viscosity and density are increased with increase of the applied pressure. Nonetheless, the results showed that the density and viscosity are inversely proportional to the operating temperatures.

## References

- [1]. Salem M. A.; Ahmed M. B.; Ali S. E.; Almahdi A. A. Simulation of Thermodynamic properties of natural gas Mixture feedstock of mellitahgas plant, 1st International Conference on Chemical, Petroleum, and Gas Engineering (ICCPGE-2016), December 20-22, 2016; Alkhoms, Libya, 2016, 1, 229-235 (<http://iccpge.elmergib.edu.ly/iccpgePapers/281.pdf>).
- [2]. Viswanathan A. Viscosities of natural gases at high pressures and high temperatures, Master Thesis, Petroleum Engineering, Taxes University 2007. (<http://oaktrust.library.tamu.edu/bitstream/handle/1969.1/5823/etd-tamu-2007A-PETE-Viswana.pdf?sequence=1>)
- [3]. Fayazi A.; Arabloo M.; Mohammadi A. H. Efficient estimation of natural gas compressibility factor using a rigorous method. J. Natural Gas Sci. Eng., 2014, 16, 8-17 (<https://doi.org/10.1016/j.jngse.2013.10.004>).
- [4]. Wetenhall B.; Race J. M.; Downie M. J., The effect of CO<sub>2</sub> purity on the development of pipeline networks for carbon capture and storage schemes, International J. Greenhouse Gas Control 2014, 30, 197–211. (<http://dx.doi.org/10.1016/j.ijggc.2014.09.016>).
- [5]. Moshfeghian M. Impact of CO<sub>2</sub> on natural gas density, 2018. ([http://www.petroskills.com/blog/entry/00\\_totm/apr18-fac-impact-of-co2-on-natural-gas-density#.Wusq0vkvzwc](http://www.petroskills.com/blog/entry/00_totm/apr18-fac-impact-of-co2-on-natural-gas-density#.Wusq0vkvzwc))
- [6]. Kumar, N. Compressibility factor for natural and sour reservoir gases by correlations and cubic equations of state, M.Sc. Thesis, 2004 Texas Tech University (<http://hdl.handle.net/2346/1370>) or (<https://ttu-ir.tdl.org/ttu-ir/handle/2346/1370>).
- [7]. Heidaryan E.; Salarabadi A.; Moghadasi J. A novel correlation approach for prediction of natural gas compressibility factor, J. Natural Gas Chemistry, 2010, 19, 189–192 ([https://doi.org/10.1016/S1003-9953\(09\)60050-5](https://doi.org/10.1016/S1003-9953(09)60050-5)).

## Novel Green Sorbents Derived from *Mesembryanthemum*-Based Biomass for Wastewater Treatment Applications

Almaki Abushaina<sup>1</sup>, Abdelrahman Sultan<sup>\*1</sup>, Wael Elhrari<sup>2</sup>, Almahdi A. Alhwaige<sup>\*1</sup>

<sup>1,\*1</sup>Department of Chemical and Petroleum Engineering, College of Engineering, Elmergib University, Alkhoms, Libya

<sup>2</sup>Polymer Research Center, Tripoli, Libya

<sup>1</sup>chealmaki@yahoo.com; <sup>\*1</sup>sultanabdelrahman@yahoo.com; <sup>2</sup>almhdi\_e2000@yahoo.co.uk; <sup>\*1</sup>wael@prc.ly

### ABSTRACT

A great challenge has been done for utilization of natural gas (NG) Biomass-based materials have received much attention recently in both academia and industry. Biomaterials have been widely applied for development of porous solids for wastewater treatment applications due to their low-cost, non-toxic, and containing of various chelating groups such as amino and hydroxyl moieties. This study reports for the first time, development of novel sorbent from *Mesembryanthemum*-based biomass for water purification applications. The obtained sorbent has been characterized using Fourier Transform Infrared spectroscopy (FTIR). The performance for removal of various water pollutants was investigated in batch mode. The effects of adsorption factors including, contact time, sorbent dose, pH and initial concentration. The results revealed that the obtained sorbent exhibited an extreme high potential for adsorbing water pollutants.

**Keyword**— Biomass; Wastewater treatment; Methylene blue dye; Adsorption; Adsorption isotherm models.

### 1. Introduction

Wastewater treatment have been received a significant attention due to the increase of pollution of water sources. Water pollutants are different in nature and have diverse sources. Among of them, dyes, organic synthetic materials, are mainly found in effluents of various industrial discharges, including dyeing and textile factories. Dyes are considered to be toxic and hazardous materials to human health and environment even at low concentrations [1]. Therefore, plenty of research work was conducted by many researchers to develop methods for removal of pollutants from the industrial effluents, such as chemical oxidation, incineration, wet oxidation, air stripping, adsorbents, electrolyte decomposition, ion exchange method, biological methods. Adsorption technique has been considered a powerful alternative method for the removal of dyes and other pollutants from industrial wastewaters. Therefore, it becomes the most popular water purification method due to its advantages, including the effectiveness, working at wide range of operating conditions, and the simplicity of removing a broad range of pollutants, even from the gaseous environment [2–4]. Adsorption process is a surface phenomenon in which the pollutants attachment to the adsorbent surface via physical or chemical interactions [5].

The adsorption efficiency is affected by the nature and type of adsorbent surface. Since the dyes have different structures and different functional groups, the researchers tried for long time to develop adsorbents that are both efficient and economical for dye removal. Early, activated carbon has been considered as an effective adsorbent due to its high porosity and large surface area. But due to its high

production cost, researchers tried to use several inexpensive materials as sorbents for the removal of pollutants from wastewaters [6-13]. Agricultural-based biomasses have been considered as low cost effective absorbents since they contain polysaccharides and proteins that have various functional groups like carboxyl, hydroxyl and phosphates, which are the most attractive sites for many pollutants. Among of these biosorbents, almond shell, maize cob waste, wood sawdust, and sunflower seed hull have been evaluated for wastewater treatment applications [14]. *Mesembryanthemum crystallinum* (*Cryophytum crystallinum*) is ice plant that belongs to the family Aizoaceae, which is a creeping plant with succulent leaves (see Figure 1). *Mesembryanthemum crystallinum* (MC) is flat succulent plant native to Africa, Sinai and southern Europe, and naturalized in North America, South America and Australia. *Mesembryanthemum crystallinum* is a halophyte plant widely used in the traditional medicine [15]. In the present study, the performance of *Mesembryanthemum crystallinum* (MC), collected from Libya biotope, for wastewater treatment applications has been investigated. In order to evaluate their potential of use, adsorption of methylene blue dye at various conditions has been studied.



Figure 1: Image of *Mesembryanthemum crystallinum*.

## 2. Materials and Methods

### 2.1. Materials

Methylene blue (MB) dye,  $H_2SO_4$ , and NaOH were the chemicals that have been used in this research work. The leaves and branches of the *Mesembryanthemum crystallinum* (MC) plant were collected from their native biotope in Libya during May 2018.

### 2.2. Biosorbents Preparation and Adsorption Experiments

The Novel Leaves-MC and Branches-MC biosorbents were prepared as follows. After overnight drying at 60 °C, Leaves and branches of *Mesembryanthemum crystallinum* (MC) plant were ground separately using a manual mortar (size range 1-3 mm). The produced powders were used in adsorption experiments without any further modifications. The adsorption experiments were carried out in a flask and the aqueous solution was agitated with magnetic carrier at 150 rpm. To evaluate the

adsorption study, 0.6g of biosorbent were added into 100 mL of MB dye aqueous solution with a specific initial concentration and pH. Various samples were taken at different contact time for investigation of the removal percentage. After, removal of the sorbent sample, the concentration was obtained using UV-VIS spectrophotometer via measuring absorbency values at 664 nm. The adsorption percentage was calculated according to Eq.1.

$$R\% = \frac{(C_{A0} - C_A)}{C_{A0}} \times 100 \quad (1)$$

where  $C_{A0}$  and  $C_A$  are the initial and the concentration of MB dye in the solution at time (t), respectively.

### 2.3. Characterization

The structure of the *Mesembryanthemum crystallinum* (MC) was confirmed by Fourier a Bruker Vertex infrared spectroscopy (FTIR), resolution 3  $\text{cm}^{-1}$ , in the range of 4000-500  $\text{cm}^{-1}$  using the KBr pellet technique. Dry leaves of *Mesembryanthemum crystallinum* (MC) were crushed into powder in a mortar and an amount about 6-8 mg of sample was used in each pellet.

## 3. Results and Discussion

### 3.1. Analysis of FTIR

The FT-IR spectra of leaves powder of used *Mesembryanthemum crystallinum* (MC) for adsorption of MB dye is shown in Figure 2. The FTIR spectrum of the sample was obtained in the scanning range of 500~4000  $\text{cm}^{-1}$ . The absorption bands for FT-IR show existence the characteristics of cellulosic nature. The absorption band at 3426  $\text{cm}^{-1}$  was due to the banding of hydroxyl groups (-OH). In addition, the FT-IR results also show significant peaks at about 2935 and 2848  $\text{cm}^{-1}$ , which can be assigned to the C-H symmetrical and C-H asymmetrical stretching vibration from the organic-moiety. The band at 1634  $\text{cm}^{-1}$  is suggested to  $-\text{NH}_2$  groups stretching vibrations and N-H for primary amine. Furthermore, appearance of bands at 1316  $\text{cm}^{-1}$  and 1018  $\text{cm}^{-1}$  assigned to the existence of the features of carbohydrate polymers nature. The apparent existence of amine and hydroxyl functional groups together with leaves of *Mesembryanthemum crystallinum* (MC) confirms the sample is in hydrophilic in nature, which helps to substantiate the effective removal of dyes through the photodegradation- adsorption process [20].

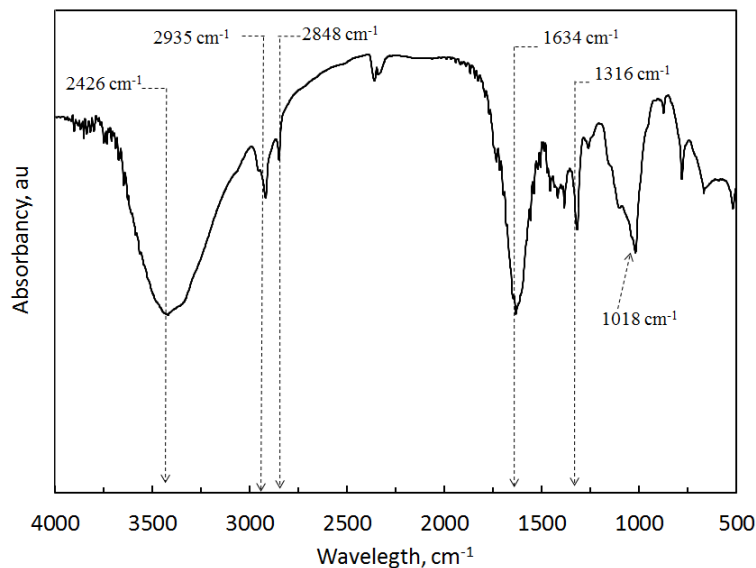


Figure 2: FT-IR spectra of leaves powder of Mesembryanthemum crystallinum (MC).

### 3.2. Effect of Absorbent Type

Due to their abundance, biomaterials — organic materials derived from living substances — have attracted a lot of research attention as potential non-toxic, low-cost and environmentally friendly adsorbents [5,13,14]. In this study, both leaves and branches of *Mesembryanthemum crystallinum* (MC) in the form of powder were examined to remove methylene blue dye (MB dye) from aqueous solution over a wide range of time (0–100 min). The results showed that the prepared adsorbents exhibited high adsorption capacities for MB dye. For example, the maximum percentage removal ( $R\%$ ) of 95.3 % and 80.1% were achieved for Leaves-MC and Branches-MC, respectively (see Figure 3). This suggested that presence of active groups in both biomass particles has significant contribution for MB dye adsorption via ionic exchange mechanism interaction. In addition, higher adsorption efficiency of (Leaves-MC) can be justified on the basis of availability of more adsorption sites and higher surface area for leaves than branches.

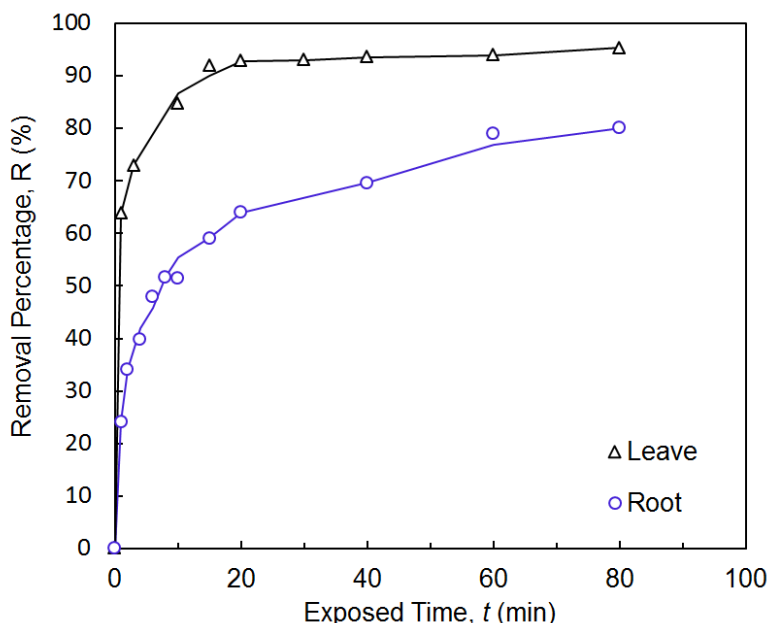


Figure 3: Effect of sorbent type on the adsorption efficiency of MB dye.

### 3.3. Effect of Contact Time

Figure 2 represents the effect of contact time on MB dye adsorption using Leaves *Mesembryanthemum crystallinum* (MC) Biomass (Leaves-MC) and Branche *Mesembryanthemumcrystallinum* Biomass (Branches-MC). The adsorption experiments were evaluated for initial concentration of 25 mg MB dye/L using 0.6 g sample dosage at ambient conditions for 80 min. As seen in Figure 2, the adsorption efficiency was increased with contact time. For example, the removal percentage was increased from 63.8 % to 92.8 % with an increase in time from 1 min to 20 min, respectively. This increase is attributed to the mass transfer limitations of MB dye from the bulk concentration to the sorbent surface. These observations are in good agreement with the previously reported studies [13].

In addition, it was observed that the MB dye adsorption was fast during the first 2 min, after which it became slower and finally reached equilibrium. The removal percentage of MB dye using Leaves-MC reached a constant rate after 20 min; however, Braches-MC showed an equilibrium adsorption after 1 h. The rapid MB dye adsorption was due to the large number of active sites available at sample surface for adsorption at the beginning of the contact time. However, the availability of these active sites decreased with contact time due to saturation with adsorbates. The remaining available active sites on sorbent surface become difficult to occupy by pollutants due to the repulsion between the solute molecules of the solid and bulk phases. Also, the surface energy of sorbents has a significant contribution for the interactions of pollutants with sorbents [14].

### 3.4. Effect of Sorbent Dosage

The amount of sorbent is an important parameter, which is proportionally affects the adsorption efficiency of the pollutants. Figure 4 shows the results of MB dye removal using Leaves-MC sample

at initial pH value of 8 and initial MB dye concentration of 25 mg/L for a contact time of 80 min. The dosage of the Leaves-MC adsorbent varied from 0.3 to 1.2 g. The results showed that the removal percentage of MB dye increases with increasing the amount of sorbents, which ascribed to the increase in the number of active sites. For instance, the adsorption efficiency was increased from 63.95% to 92.83% with increasing the adsorbent dosage from 0.3 g to 0.6 g, respectively. Even though a sorbent dosage greater than 0.6 g led to a non significant increase in MB dye removal (see figure 3), a dosage of 0.6 g of Leaves-MC was selected for all further experiments.

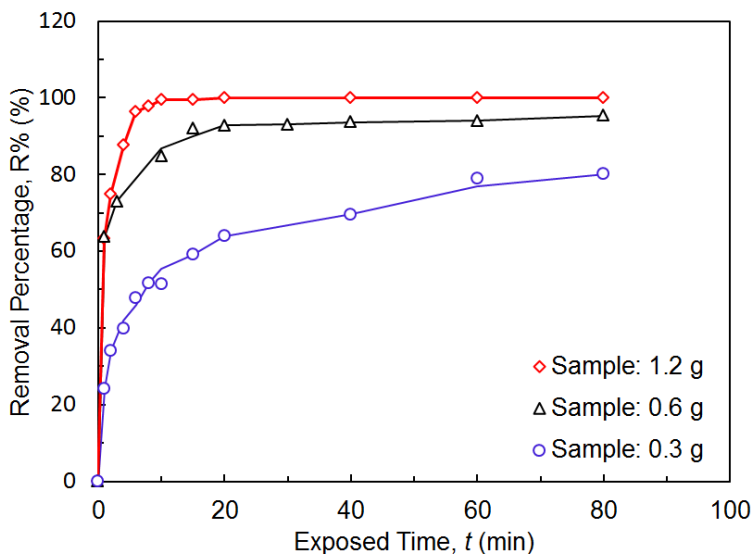


Figure 4: Effect of sorbent dosage on the adsorption efficiency of MB dye.

### 3.5. Effect of Initial MB Dye Concentration

The effects of the initial concentration of MB dye on the removal efficiency were also investigated using 0.6 g of Leaves-MC with a contact time of 1 h. The initial concentration of MB dye in the solution was varied between 12.5 to 50 ppm, while all the other parameters were kept constant during the experiments. Figure 5 demonstrated the removal percentage as a function in contact time for different initial MB dye concentration. For example, the percentage removal of MB dye decreased from 92.8 % to 69.1 % when increasing the initial concentration from 25 to 50 ppm, respectively. This decrease in adsorption of MB dye is due to the fact that the time required to attain equilibrium was expected to be longer at higher concentrations than at lower concentration. As seen in Figure 5, adsorption with initial concentration of 12.5 ppm showed approximately constant adsorption efficiency after only 6 min. Although 97.7% MB dye removal was obtained using an initial concentration of 12.5 ppm, increasing the initial concentration of MB dye in the solution leads to a decrease in the adsorption efficiency.

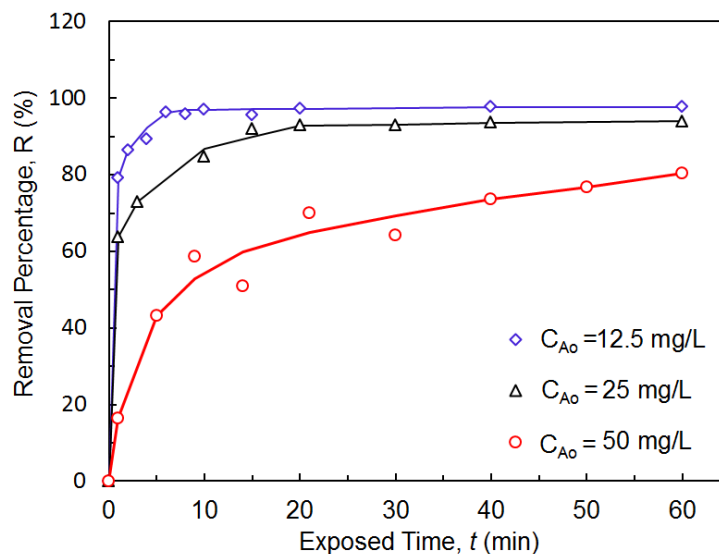


Figure 5: Effect of initial concentration on the adsorption efficiency of MB dye.

### 3.6. Effect of Initial pH

The initial pH of aqueous solution is an important parameter affecting the adsorption efficiency [13]. Therefore, the effects of initial solution pH were studied in the pH range of 2.0 -12.0 using Leaves-MC sorbent at MB initial concentration of 25 mg/L, adsorbent dose of 0.6g and room temperature, and the results were represented in Figure 6. As shown in the insert Figure, a maximum removal percentage of 94.9 % of MB dye was observed at initial pH of 12.0 after 1 h. In addition, the removal efficiencies of MB dye were slightly decreased to 93.6 % and 85.2 % with the decrease in initial pH to 8.0 and 2.0, respectively. The reduction in the MB dye removal percentage is attributed to the fact that the unfavorable adsorption of dye cations on the positively charged sorbent surface caused by the electrostatic repulsion. However, at higher initial pH value (pH = 12.0) the surface of Leaves-MC may gain a negative charge, which contributes to an increase in MB dye adsorption due to the electrostatic force of attraction with sorbent surface. It is well-known that for basic dye adsorption, negatively charged groups on the adsorbent are necessary. At lower pH values charge of the surface of Leaves-MC may get positively charged ions and thus the competitive effects of ions as well as the electrostatic repulsion between the dye molecules and the positively charged active adsorption sites on the surface of the Leaves-MC lead to a decrease in the uptake of dye molecules. Similar adsorption tendency of MB dye were reported by several studies [6,13].

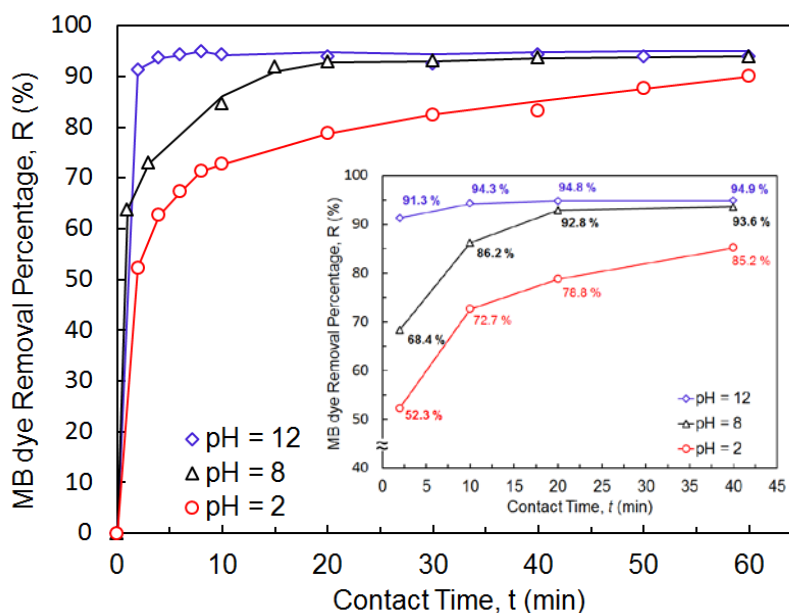


Figure 6: Effect of initial pH of MB dye aqueous solution on the adsorption efficiency of MB dye.

Early studies indicated that the adsorption of cationic dye molecules onto the sorbent surface is significantly dependent on initial pH since the functional groups, which are the key point for interaction between dye molecules and adsorbent, can be protonated or deprotonated to produce different surface charges in solution at different pH values [1,6,13,16]. Furthermore, after 4 minutes, the removal percentage was approximately constant in the pH of 12.0 for MB, whereas it increased gradually for pH 2.0 and 8.0.

#### 4. Conclusions

In this paper, *Mesembryanthemum crystallinum* (MC)-based biosorbents for the removal of toxic MB dye from aqueous solution have been studied. The use of (MC)-based biosorbents offers many attractive features such as the outstanding adsorption efficiency for MB dye and the fact that these materials are low-cost, non-toxic and biocompatible. Several parameters such as adsorbent dosage, contact time, pH and initial concentration were found to significantly affect the MB dye removal efficiency. The optimum removal from the aqueous solution was achieved at pH 12.0, 0.6 g sample dosage, 4 min contact time, and 25 ppm initial MB dye concentration. In addition, these sorbents showed a fast kinetics for first 4 min, and then a gradual increase in adsorption efficiency was observed until reach equilibrium in a short time (10 – 20 min). A maximum 94.9 % removal percentage of MB dye from aqueous solution was achieved. This high adsorption capacity by Leaves-MC is mainly attributed to additional adsorption sites.

#### References

- [1]. Chen, S.; Zhang, J.; Zhang, C.; Yue, Q.; Li, Y.; Li, C. Equilibrium and kinetic studies of methyl orange and methyl violet adsorption on activated carbon derived from *Phragmites australis*. *Desalination* 2010, 252, 149–156. <https://doi.org/10.1016/j.desal.2009.10.010>
- [2]. S. Los', L. Duclaux, W. Kempin'ski, M. Polomska, Size effect in the characterization of microporous activated nanostructured carbon. *Microporous Mesoporous Mater.* 130 (2010) 21–25. <https://doi.org/10.1016/j.micromeso.2009.10.007>
- [3]. C. Petit, T.J. Bandosz, Role of surface heterogeneity in the removal of ammonia from air on micro/mesoporous activated carbons modified with molybdenum and tungsten oxides. *Microporous Mesoporous Mater.* 118 (2009) 61–67. <https://doi.org/10.1016/j.micromeso.2008.08.016>
- [4]. D.D. Asouhidou, K.S. Triantafyllidis, N.K. Lazaridis, K.A. Matis, S.S. Kim, T.J. Pinnavaia. Sorption of reactive dyes from aqueous solutions by ordered hexagonal and disordered mesoporous carbons. *Microporous Mesoporous Mater.* 117 (2009) 257–267. <https://doi.org/10.1016/j.micromeso.2008.06.034>
- [5]. K.Y. Foo, B.H. Hameed, An overview of landfill leachate treatment via activated carbon adsorption process, *J. Hazard. Mater.* (2009), doi:10.1016/j.jhazmat.2009.06.038.
- [6]. El Mouzdahir, Y.; Elmchaouri, A.; Mahboub, R.; Gil, A.; Korili, S. A. Adsorption of Methylene Blue from Aqueous Solutions on a Moroccan Clay. *J. Chem. Eng. Data* 2007, 52, 1621–1625. DOI: 10.1021/je700008g
- [7]. Zolgharnein, J.; Shahmoradi, A. Adsorption of Cr(VI) onto *Elaeagnus* Tree Leaves: Statistical Optimization, Equilibrium Modeling, and Kinetic Studies. *J. Chem. Eng. Data* 2010, 55, 3428–3437. DOI: 10.1021/je100157y
- [8]. Sharma, Y. C.; Uma; Sinha, A. S. K.; Upadhyay, S. N. Characterization and Adsorption Studies of *Cocos nucifera* L. Activated Carbon for the Removal of Methylene Blue from Aqueous Solutions. *J. Chem. Eng. Data* 2010, 55, 2662–2667. doi/abs/10.1021/je900937f
- [9]. Fetterolf, M. L.; Patel, H. V.; Jennings, J. M. Adsorption of Methylene Blue and Acid Blue 40 on Titania from Aqueous Solution. *J. Chem. Eng. Data* 2003, 48, 831–835. doi/abs/10.1021/je025589r
- [10]. Karadag, D.; Turan, M.; Akgul, E.; Tok, S.; Faki, A. Adsorption Equilibrium and Kinetics of Reactive Black 5 and Reactive Red 239 in Aqueous Solution onto Surfactant-Modified Zeolite. *J. Chem. Eng. Data* 2007, 52, 1615–1620. DOI:10.1021/je7000057
- [11]. Srivastava, V. C.; Mall, I. D.; Mishra, I. M. Equilibrium Modeling of Ternary Adsorption of Metal Ions onto Rice Husk Ash. *J. Chem. Eng. Data* 2009, 54, 705–711. DOI:10.1021/je8003029
- [12]. Wu, Y.; Zhang, L.; Gao, C.; Ma, J.; Ma, X.; Han, R. Adsorption of copper ions and methylene Blue in a single and binary system on wheat straw. *J. Chem. Eng. Data* 2009, 54, 3229–3234. DOI:10.1021/je900220q
- [13]. C. Duran, D. Ozdes, A. Gundogdu and H. B. Senturk. Kinetics and Isotherm Analysis of Basic Dyes Adsorption onto Almond Shell (*Prunus dulcis*) as a Low Cost Adsorbent. *J. Chem. Eng. Data* 2011, 56, 2136–2147. dx.doi.org/10.1021/je101204j
- [14]. Hasar, H. Adsorption of nickel (II) from aqueous solution onto activated carbon prepared from almond husk. *J. Hazard. Mater.* 2003, 97, 49–57. DOI:10.1016/S0304-3894(02)00237-6
- [15]. Bouftira C.; Abdelly S. S. Characterization of cosmetic cream with *Mesembryanthemum crystallinum* plant extract: influence of formulation composition on physical stability and anti-oxidant activity. *International J of Cosmetic Science*, 2008, 30, 443-452. <https://doi.org/10.1111/j.1468-2494.2008.00469.x>



- [16]. Alkan, M.; Dogan, M.; Turhan, Y.; Demirbas, O.; Turan, P. Adsorption kinetics and mechanism of maxilon blue 5G dye on sepiolite from aqueous solutions. Chem. Eng. J. 2008, 139, 213–223. DOI:10.1016/j.cej.2007.07.080

# Novel Green Photocatalysts Derived from Date Syrup-based biomass/TiO<sub>2</sub> for Photocatalytic Oxidation of Methylene Blue Dye in Aqueous Solutions

Mohammed A. El-Ghweil<sup>1</sup>, Almahdi A. Alhwaige<sup>2</sup>, Wael Elhrari<sup>3</sup>

<sup>1</sup>Department of Chemical Engineering, College of Engineering, Al-Asmariya Islamic University, Zliten, Libya

<sup>2</sup>Department of Chemical and Petroleum Engineering, College of Engineering, Elmergib University, Alkhoms, Libya

<sup>3</sup>Polymer Research Center, Tripoli, Libya

<sup>1</sup>mohmmedalgoker20@gmail.com; <sup>2</sup>almhdi\_e2000@yahoo.co.uk; <sup>3</sup>wael@prc.ly

## ABSTRACT

This study reports for the first time, development of novel photocatalyst from date syrup-based biomass and TiO<sub>2</sub> for photocatalytic oxidation of methylene blue MB dye in wastewaters. The properties of the derived photocatalysts have been studied using Fourier Transform Infrared spectroscopy (FTIR). The performance for photocatalytic oxidation of MB dye was investigated in batch slurry reactor. The effects of operating conditions including, contact time, photocatalyst amount, pH, initial concentration, and temperature on photocatalytic oxidation behavior were investigated. The Langmuir-Hinshelwood kinetic model was applied to study the kinetics photocatalytic oxidation of MB dye. The results revealed that the derived photocatalysts exhibited an extremely high potential for photocatalytic oxidation of MB dye. A maximum ~88% conversion of MB dye was achieved at 50 °C and atmospheric pressure. The finding of this study may open a new avenue for not only improving the photocatalytic performance, but also for further research areas.

**Keyword**— Biomass; Wastewater treatment; Methylene blue dye; Photocatalytic oxidation; Langmuir-Hinshelwood kinetic model.

## 1. Introduction

Even though water covers about 70% of the Earth's surface, soft water is greatly limited. Therefore, the demand for water purification has been increased with modern life due to the increase of the pollution of water sources with an increase in world population and industrial revolution [1-3].

Water pollution is the main modern environmental problem, which is mainly is caused by variety activities such as domestic use, industry, and agricultural. Currently, there is growing concern throughout the world in reducing water pollution due to the fact that these pollutants have significant environmental and health impacts for all living organisms. These various types of water pollutants can be classified into physical, biological, and chemical pollutants. However, organic pollutants are the most pollutants that available in water, including hydrocarbons and organic dyes. In addition, dyes are colored organic substances that capable of imparting their characteristic colors in water. Synthetic dye manufacturing started in 1856 by W.H. Perkin. Dyes are intensively used in many

industries to color the products, including textiles, foods, pharmaceuticals, cosmetics, paints, pigments, and ceramics. The majority of dyes cause a potential health hazard to all forms of life. Among of them, allergic responses, skin dermatoses, and damages livers and lungs [2,4]. Therefore, it is very important to remove toxic dyes from water.

Separation processes based on fluid mechanics including sedimentation, centrifugation, filtration, flotation and membranes have been widely implied for wastewater treatment applications. Recently, the advanced oxidation techniques are considered the powerful methods for wastewater treatment, which are the processes of destruction of pollutants by agents that exhibit high oxidation potentials without secondary pollution.

Heterogeneous photocatalytic oxidation process was developed in the 1970s. In the past two decades, numerous studies have been carried out on the application of heterogeneous photocatalytic oxidation process for wastewater treatment [1]. Photocatalytic process has been gained much attention due to its significant efficiency for degradation of wide range of organic pollutants in aqueous solutions, such as organic solvents, hydrocarbons, and dyes [5]. Additionally, it is working by simple method, operating at wide range of conditions, low energy requirements, and it is environmentally friendly method.

Nowadays, heterogeneous photocatalytic oxidation technique has been considered as an unconventional technology in environmental remediation because it is capable of oxidation of the pollutants without production of any harmful by-products (see Figure 1) [7]. In addition, there is no second pollution associated with this method because no disposal problems [4,6].

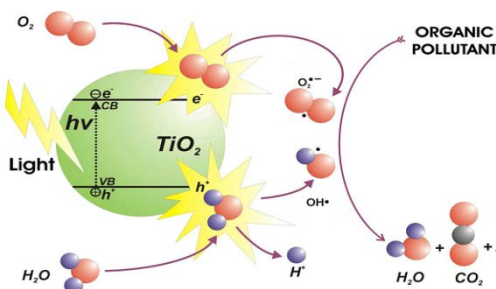


**Figure 1:** Schematic diagram of photocatalytic excitation of  $\text{TiO}_2$  as semiconductor by UV/solar irradiation [7].

Photocatalytic oxidation technique possesses many heterogeneous photocatalytic process consists on utilizing the near UV radiation to photo excite a semiconductor catalyst in the presence of oxygen. Photocatalytic reactions using semiconductors at the surface of the photocatalyst provide photo-induction of electron-hole pairs by band gap radiation. The most popular semiconductor is titanium dioxide ( $\text{TiO}_2$ ) with a band gap width of 3.2 eV. A wide range of pollutants have been oxidized using UV/ $\text{TiO}_2$  treatment. The objective of this research work has been proposed for development of a novel biomass-based photocatalyst with high performance for photocatalytic oxidation of MB dye.

## 2. Materials and Methods

## 2.1. Materials

Titanium dioxide ( $\text{TiO}_2$ ) was purchased from BDH Laboratory Supplies, England with purity of 99.0%. Methylene blue (MB) dye was obtained from Sigma-Aldrich. NaOH and  $\text{H}_2\text{SO}_4$  were purchased from Merck Chemical and these chemicals with analytical grade. All chemicals were used without further purification. The used date syrup (DS) was a homemade in Zliten city, Libya. The real water with pH  $\sim 7$  was obtained from water tap at Faculty of Engineering, Elmergib University, Alkhoms, Libya.

## 2.2. Preparation of Date-Syrup/ $\text{TiO}_2$ (DS- $\text{TiO}_2$ ) Photocatalyst

In this study, a novel photocatalyst has been developed using date syrup (DS) and titanium dioxide ( $\text{TiO}_2$ ). A 0.5 g of titanium dioxide ( $\text{TiO}_2$ ) was dispersed in 6 mL of homemade date syrup (DS) to make slurry. The mixture was stirred under heating at 70 °C for one hour (1 h) and then, the mixture was transferred into petri dish and dried in an oven at 60 °C for 24 h for drying. The dried DS- $\text{TiO}_2$  composites were carbonized to obtain DS- $\text{TiO}_2$  carbon monolith. The carbonized DS- $\text{TiO}_2$  monolith was ground to fine powders and then, it was used for photooxidation studies. The newly developed photocatalysts were abbreviated as DS- $\text{TiO}_2$ -x, where x refers to the inclusion of  $\text{TiO}_2$  semiconductor. In order to study the effect of important parameters like irradiation time, catalyst dosage, pH, and operating temperature, various batch experiments were run for each parameter.

## 2.3. Characterization

The structure of the *Mesembryanthemum crystallinum* (MC) was confirmed by Fourier a Bruker Vertex infrared spectroscopy (FTIR), resolution 3  $\text{cm}^{-1}$ , in the range of 4000-500  $\text{cm}^{-1}$  using the KBr pellet technique. Dry leaves of *Mesembryanthemum crystallinum* (MC) were crushed into powder in a mortar and an amount of 6-8 mg of the sample was used in each pellet.

## 2.4. Photocatalytic Oxidation of Methylene Blue Dye

The photocatalytic activity of the developed DS- $\text{TiO}_2$  photocatalyst was investigated by decomposition of the MB dye via photocatalytic oxidation technique. The photocatalytic oxidation experiments of MB dye were carried out by employing the obtained photocatalyst of date stone-titanium dioxide (DS- $\text{TiO}_2$ ) carbon powders under different experimental conditions. For each run of photocatalytic oxidation of MB dye, a one-liter (1L) from the stock solution was placed into the reactor vessel. After the addition of the desired photocatalyst quantity, the solution was exposed to a UV light for a period of time. Because the UV lamp produces a heat, the temperature of irradiated solution was controlled using water flow heat exchanger. The performance of photocatalytic oxidation of MB dye was tested at different time intervals (10-20 min). The photocatalyst was removed from the samples using a centrifugation at 800 rpm for 30 min and then, the concentration of MB dye in the solution was analyzed using a UV-visible spectrophotometer at  $\lambda=664$  nm. The unknown concentrations of the MB dye as function of time were calculated using the prepared calibration curve. Finally, according to the obtained MB dye concentration, the percentage conversion ( $\%A$ ) of photocatalytic oxidation was calculated using Eq. 1.

$$\text{Conversion percentage, } (x_A \%) = \frac{C_{A0} - C_A}{C_{A0}} * 100 \quad (1)$$

where,  $x_A\%$  is oxidation percentage of MB dye,  $C_{A0}$  and  $C_A$  are the initial concentration and the concentration of MB dye after irradiation time,  $t$ .

### 3. Results and Discussion

#### 3.1. Analysis of FT-IR

The FT-IR spectra of DS-TiO<sub>2</sub>-0.5 before used for photocatalytic oxidation of MB dye is shown in Figure 1. The absorption bands for prepared DS-TiO<sub>2</sub> show existence characteristics for both date syrup (DS) and titanium dioxide (TiO<sub>2</sub>). The absorption band at 3402 cm<sup>-1</sup> was due to the banding of hydroxyl groups (-OH) of DS. The FT-IR results also show significant peaks at about 2925 and 2887 cm<sup>-1</sup>, which can be assigned to the C-H symmetrical and C-H asymmetrical stretching vibration from the organic-moiety. The band at 1634 cm<sup>-1</sup> is ascribed to -NH<sub>2</sub> groups stretching vibrations and N-H for primary amine present in DS. Furthermore, appearance of bands at 920 and 876 cm<sup>-1</sup> assigned to the existence of TiO<sub>2</sub> compound in the prepared photocatalyst. The apparent existence of amine and hydroxyl functional groups together with DS-TiO<sub>2</sub> photocatalyst helps to the removal of dyes through the photodegradation-adsorption process [8].

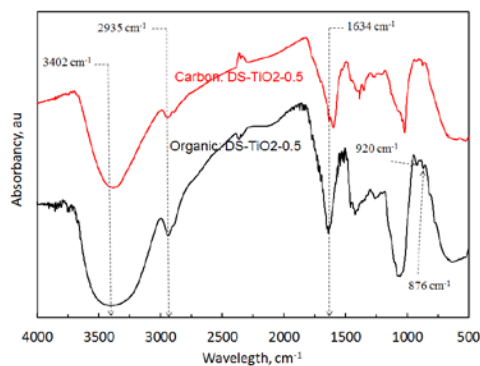
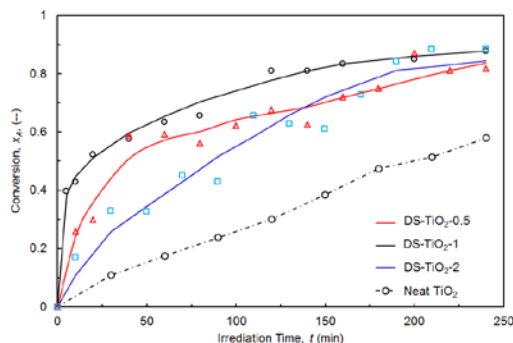


Figure 1: FT-IR spectra of DS-TiO<sub>2</sub>-0.5 photocatalyst.

#### 3.2. Effect of Irradiation Contact Time

The effect of irradiation time on photocatalytic oxidation efficiency of MB dye aqueous solution was investigated. The photocatalytic oxidation of 10 mg L<sup>-1</sup>MB dye aqueous solution were performed in slurry batch reactor using neat TiO<sub>2</sub>, DS-TiO<sub>2</sub>-0.5, DS-TiO<sub>2</sub>-1, and DS-TiO<sub>2</sub>-2 photocatalysts at 50 °C and pH ~ 7 and the results are shown in Figure 2. The results showed that the photocatalytic oxidation efficiency of MB dye increases with an increase in the irradiation time until reaches an equilibrium. For example, the sample DS-TiO<sub>2</sub>-0.5 showed an increased in the conversion of photocatalytic oxidation of MB dye from 25.9 % to 59.2 % with an increase of the irradiation time from 5 min to 60 min, respectively. The change in the photocatalytic oxidation conversion is ascribed

to the fact that the oxidation conversion becomes slow after a certain time because most of MB dye molecules have been decomposed and a decrease in the MB dye concentration may occur [8,9].



**Figure 2:** Effect of irradiation time on photocatalytic oxidation of MB dye at 50 C°, initial concentration 10 mg L<sup>-1</sup>, pH ~ 7.

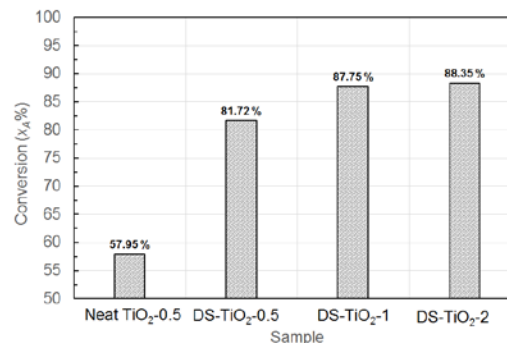


**Figure 3:** Equilibrium conversion of photocatalytic oxidation of MB dye using the obtained photocatalysis.

### 3.3. Effect of Sorbent Dosage

In photocatalytic processes, the amount of semiconductors has a large contribution for increasing the oxidation efficiency of MB dye up to a certain amount of catalyst. Therefore, because semiconductors are expensive materials, the used amount of catalyst should be optimized. Figures 2 and 3 demonstrate the effect of TiO<sub>2</sub> concentration on photocatalytic oxidation efficiency of MB dye. For example, when the irradiation time is 20 min the photocatalytic oxidation conversion of MB dye were 35.9 %, 52.2 %, and 18.3 %, for DS-TiO<sub>2</sub>-0.5, DS-TiO<sub>2</sub>-1 and DS-TiO<sub>2</sub>-2, respectively. As seen in Figure 3, the results indicated that the maximum photocatalytic oxidation conversion of MB dye using neat-TiO<sub>2</sub> of 57.95% after 240 min. However, the photocatalytic oxidation efficiency increases after combination of date syrup (DS) with different amount of TiO<sub>2</sub> and significant photocatalytic oxidation efficiency was achieved. For example, the equilibrium conversions of 81.32 % to 87.75 % were obtained using DS-TiO<sub>2</sub>-0.5 and DS-TiO<sub>2</sub>-1, respectively. In addition, DS enhances the adsorption of MB dye to the catalyst surface due to presence of date syrup functional groups. The comparison of the results for DS-TiO<sub>2</sub>-0.5 and DS-TiO<sub>2</sub>-1, it clearly that 0.5 TiO<sub>2</sub> in the sample DS-TiO<sub>2</sub>-0.5 is the optimum amount of TiO<sub>2</sub> because a small increase in the oxidation conversion as compared to the amount of catalyst added. The increase of catalyst amount above the optimum value it causes a decrease in photocatalytic oxidation efficiency of MB dye due to the agglomeration of catalyst particles the interception of the light by the suspension [10-13].

### 3.4. Effect of Initial Concentration of MB dye

The effect of initial concentration of MB dye on the photooxidation efficiency have been also investigated using varying initial MB dye concentration, namely 10, 25, 50 mg L<sup>-1</sup>. As seen in Figure 4, it is clearly that the results indicated that when the initial concentrations of MB dye increases, the photocatalytic oxidation efficacy decreases. For example, after 150 irradiation time, the photocatalytic oxidation efficiency was increased from 25.00 % to 56.62 % with a decrease in initial concentration from 50 mg L<sup>-1</sup> to 10 mg L<sup>-1</sup>, respectively. The decrease in the oxidation conversion is due to the fact that the quantity of light (quantum of photons) penetrating the MB dye aqueous solution to reach the

photocatalyst surface is reduced owing to the hindrance in the path of light thus the formation of the hydroxyl radicals is simultaneously reduced [9].

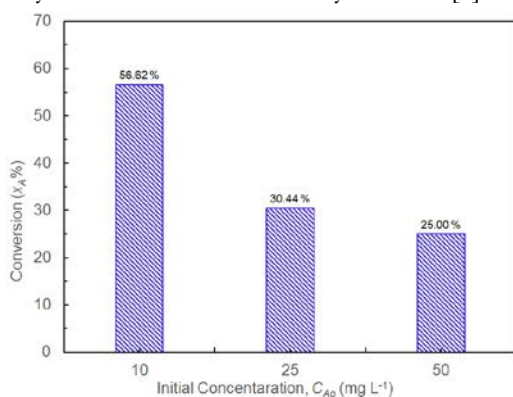


**Figure 4:** Effect of initial concentration on photocatalytic oxidation of MB dye at 50 °C for 150 min of irradiation time using DS-TiO<sub>2</sub>-0.5 photocatalyst.

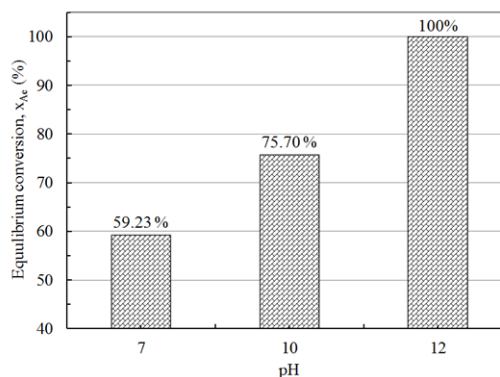


**Figure 5:** Effect of initial pH of MB dye aqueous solution on the adsorption efficiency of MB dye.

### 3.5. Effect of Initial pH

The initial pH of aqueous solution is an important parameter in the adsorption efficiency. The previous studies report that initial pH is the most important parameter that effects on the photocatalytic oxidation efficiency [8,10]. Therefore, in the present study, the effect of initial pH on conversion of photocatalytic oxidation of MB dye was evaluated for 10 mg L<sup>-1</sup> initial concentration of MB dye at 45 °C using DS-TiO<sub>2</sub>-0.5 photocatalyst for 60 min of irradiation time. The initial pH of the solutions were varied from 7 to 12, which were adjusted before exposure the solution to the UV light using acidic or basic solutions of H<sub>2</sub>SO<sub>4</sub> or NaOH, respectively, and it was not controlled during the reaction process. The photocatalytic oxidation of MB dye is found to be increase at alkaline pH due to its nature, cationic dye [8,11]. Therefore, the experiments were performed at neutral and alkaline conditions.

Figure 5 displays the effect of pH on the equilibrium photocatalytic oxidation of MB dye. The results showed that the oxidation conversion is proportional with the initial pH of the aqueous solution. For instance, the conversion of photocatalytic oxidation of MB dye was increased from 59% to 76% with an increase in pH value from 7 to 10, respectively. The pH influences the characteristics of the photocatalyst surface charge [10]. The increase in conversion of MB dye oxidation is attributed to the surface of photocatalyst gains negative charge, which is favorable to positively charged dye molecule such as MB dye. In addition, the increased efficiency in the alkaline pH range is due to the formation of OH\* radicals with an increase in pH [8]. This implies that high alkaline conditions significantly enhances the formation of the reactive intermediates that is hydroxyl radicals (OH\*), which further contribute in enhancing the reaction rate [9].

### 3.6. Effect of Temperature

To investigate the effect of operating temperature, the photooxidation efficiency of MB dye was evaluated at different temperatures. Two experiments were run for 10 mg L<sup>-1</sup> initial concentration of MB dye using DS-TiO<sub>2</sub>-0.5 for 180 min at operating temperature of 50 and 60 °C, respectively. Figure 6 represents the conversion of photocatalytic oxidation of MB dye as a function with operating temperatures. The results indicated that the oxidation conversion is increased proportionally with the operating temperature. For example, photocatalytic oxidation conversion is increased from 74.89 % to 86.94% with an increase in temperature from 50 °C to 60 °C, respectively. This increase is due to mass limitation of transport of reactants and reaction products to/from the catalyst surface, which increases with temperature. Therefore; the photocatalytic oxidation of MB dye is following an endothermic reaction [11].

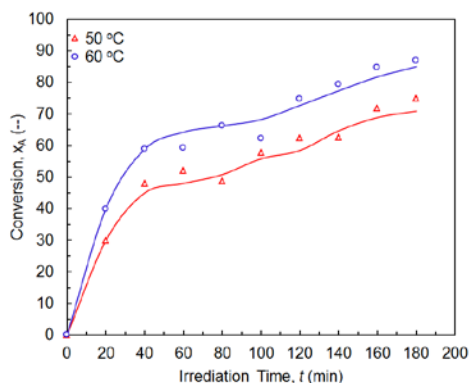


Figure 6: Effect of operating temperature on photooxidation efficiency.

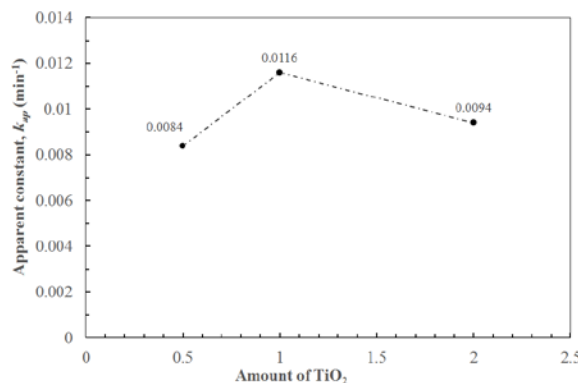


Figure 7: Effect of TiO<sub>2</sub> content on apparent kinetic constant ( $k_{ap}$ ) of MB dye.

### 3.7. Kinetic Analysis

The kinetics of the photocatalytic oxidation of MB dye aqueous solution has been also investigated using the obtained photocatalysts. The experimental data for discoloration of the MB dye using various heterogeneous photocatalysts was used to investigate the kinetic parameters of the photocatalytic oxidation reaction. The obtained experimental data was fit the Eq. 2, a plot of  $(-\ln(1-x_A))$  versus irradiation time (t) (The Figure is not included). A straight line was fitted to the data for each sample and the correlation factors ( $R^2$ ) were 0.93, 0.84, and 0.69 for DS-TiO<sub>2</sub>-0.5, DS-TiO<sub>2</sub>-1, and DS-TiO<sub>2</sub>-2, respectively. These findings suggested that photocatalytic oxidation reaction (discoloration rate) followed pseudo first-order kinetics. Therefore, the oxidation rate depended on the MB dye concentration. The value of apparent rate constant ( $k_{ap}$ ) has been also determined from the slope of the plot for each experiment. The  $k_{ap}$  values of the MB dye photocatalytic oxidation for the catalyst samples with varying TiO<sub>2</sub> concentrations of 0.5, 1.0, and 2.0 g were  $8.10 \times 10^{-3} \text{ min}^{-1}$ ,  $10.06 \times 10^{-3} \text{ min}^{-1}$ , and  $9.40 \times 10^{-3} \text{ min}^{-1}$ , respectively.

$$-\ln(1 - x_A) = k_{ap}t \quad (2)$$

Where  $x_A$  is the MB dye conversion,  $k_{ap}$  is the apparent reaction constant, and  $t$  is the reaction time. Figure 7 displays the effect of  $TiO_2$  content on apparent kinetic constant ( $k_{ap}$ ) of MB dye. As seen in the Figure, the results indicated that the amount of  $TiO_2$  has a small effect on the apparent constant ( $k_{ap}$ ), which is in the range of from  $8.10 \times 10^{-3} \text{ min}^{-1}$  to  $10.06 \times 10^{-3} \text{ min}^{-1}$ . The apparent rate constant was found to be increased with increasing  $TiO_2$  concentration up to 1 g and then it decreased, when other parameters are kept unchanged. According to the maximum apparent constant; the reaction rate expression for photocatalytic oxidation of MB dye in this study is given in Eq. 3.

$$-r_A = 10.06 \times 10^{-3} C_A \quad (3)$$

Where  $-r_A$  is the photocatalytic oxidation reaction rate in ( $\text{mg L}^{-1} \text{ min}^{-1}$ ) and  $C_A$  is the concentration of MB dye at time  $t$  in ( $\text{mg L}^{-1}$ ).

The initial kinetic of photocatalytic oxidation of organics is often described by Langmuir-Hinshelwood (L-H) [8]. In this study, initial kinetics of photocatalytic oxidation of MB dye using L-H model was also investigated using a data collected for photocatalytic oxidation of MB dye in aqueous solutions at  $50^\circ \text{C}$ ,  $\text{pH} \sim 7$  using DS- $TiO_2$ -0.5. The experimental data of photocatalytic oxidation of MB dye at different three initial concentrations (10, 25, and 50 mg MB dye/L) were fitted to L-H model, and then the kinetic parameters were obtained. The apparent reaction constants ( $k_{ap}$ ), were obtained according to Eq. 2. Figure 8 displays a plot of  $(-\ln(1-x_A))$  versus irradiation time at various initial MB dye concentrations. The plot showed a lineal relationship; therefore, the photocatalytic oxidation of MB dye follows a first order kinetics. In addition, the results indicated that the value of apparent reaction constant ( $k_{ap}$ ) were  $6.5 \times 10^{-3} \text{ min}^{-1}$ ,  $2.5 \times 10^{-3} \text{ min}^{-1}$ ,  $2.1 \times 10^{-3} \text{ min}^{-1}$  at initial MB dye concentrations of 10, 25, and 50 mg L<sup>-1</sup>, respectively. The initial reaction rate ( $r_{A0}$ ) is a product of apparent reaction constant and the initial MB dye concentration ( $r_{A0} = k_{ap} \cdot C_{A0}$ ) and the data was fitted with the L-H model (see Eq. 4) [8].

$$\frac{1}{-r_{A0}} = \frac{1}{kK C_{A0}} + \frac{1}{k} \quad (4)$$

The intercept of the plot of  $1/r_{A0}$  against  $1/C_{A0}$  is inverse the kinetic constant ( $k$ ) and the adsorption constant ( $K$ ). Figure 9 demonstrates the relationship of inverse of the initial reaction rate ( $1/r_{A0}$ ) as a function of ( $1/C_{A0}$ ). The obtained initial kinetic parameters of photocatalytic oxidation of MB dye the kinetic constant ( $k$ ) and the adsorption constant ( $K$ ) were found to be  $0.9296 \text{ mg L}^{-1} \text{ m}^{-1}$  and  $0.19925 \text{ L mg}^{-1}$ , respectively.

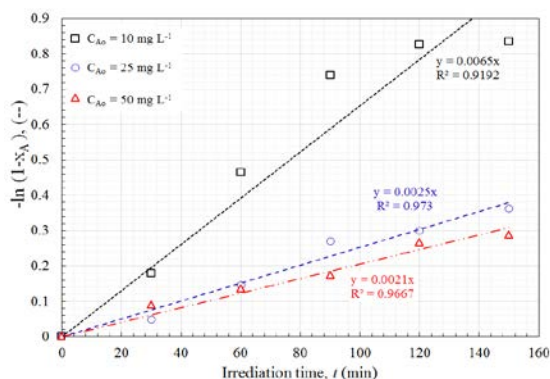


Figure 8: The fit of the experimental data with the first-order kinetic model

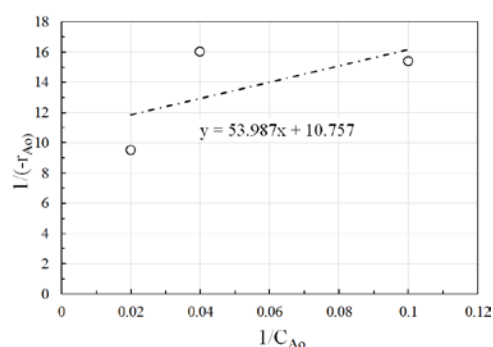


Figure 9: The plot of Langmuir-Hinshelwood model: Inverse the initial reaction rate against inverse the initial concentration.

#### 4. Conclusions

The presence of methylene blue dye (MB) in water has negatively impacts to the humans and the environment. In this study, as a modern technology for wastewater treatment, photocatalytic oxidation technique was selected in this work because it is simple method for decomposition of organic pollutants to CO<sub>2</sub> and water without contribution of any secondary pollution. In addition, the present study provides a novel root for development new photocatalysts. Therefore, we report in the first time of using date syrup (DS) in synthesis of new environmentally friendly photocatalysts and investigate its application for removal of MB dye from aqueous systems. The interactions of DS with TiO<sub>2</sub> were confirmed using FT-IR. Date syrup (DS) was composed with different quantities of TiO<sub>2</sub> as a semiconductor material. The developed EY-TiO<sub>2</sub> photocatalysts exhibit an excellent performance of MB dye photocatalytic oxidation. A significant increase in the conversion of MB dye after composed DS TiO<sub>2</sub>, and the sample of DS-TiO<sub>2</sub>-0.5 showed the optimal TiO<sub>2</sub> content. This study also conducted the photocatalytic oxidation for removing MB dye from aqueous solutions under several parameters. The photocatalytic oxidation efficiency was promoted by increasing the amount of oxidizing agent (TiO<sub>2</sub>), the initial pH of the solution, the irradiation time, and the operating temperature. The maximum conversion of 87.8 % for MB dye was achieved using the sample DS-TiO<sub>2</sub>-1. In addition, the kinetics of photocatalytic oxidation of MB dye was also investigated. The kinetic analysis indicated that DS-TiO<sub>2</sub> photocatalysts exhibit fast kinetics of MB dye photocatalytic oxidation with a reaction constant in the range of  $8.10 \times 10^{-3} - 10.60 \times 10^{-3} \text{ min}^{-1}$ . Therefore, the obtained results may open a new opportunity for the rapid and large-scale industrial preparation of novel biomass-based photocatalysts with excellent conversion of MB dye at wide range of various operating conditions.

#### References

- [1]. Ibhadon, A. O.; Fitzpatrick, P. *Heterogeneous Photocatalysis: Recent Advances and Applications*. Catalysts 2013, 3, 189-218.

- [2]. Alrumman1, A. S.; El-kott, F. A.;Keshk, M. S.*Water Pollution: Source a and Treatment*, 2016, DOI:10.5923/j.ajee.20160603.02
- [3]. Nkwonta, O. I.; Ochieng, G. M. *Water Pollution in Soshanguve Environs of South Africa*. International Journal of Environmental and Ecological Engineering,2009, 3.
- [4]. ÖDEN, M. K.; ÖZDEMİR, C. *Removal of Methylene Blue Dye From Aqueous Solution Using Natural Boron Ore And Leach Waste Material: Adsorption Optimization Criteria*Int. J. Res. Aca. Rev 2014, 2347-3215, 66-71.
- [5]. Shen, S.; Kronawitter, C.;Kiriakidis, G. *An overview of photocatalytic materials*, 2017,3,1-2.
- [6]. Ghaneian, M. T.; Taghavi, M.; Tabatabaee, M.; Ehrampoush, M. H.;Afsharnia, M.; Alami, A.; Mardaneh, J. *Synthesis, characterization and photocatalytic activity of TiO<sub>2</sub>/ZnO-supported phosphomolybdic acid nanocomposites*Journal of Molecular Liquids 2018, 249, 546 –553.
- [7]. Meenaksh, S.; Farzana, M. Hasmeth. *Synergistic Effect of Chitosan and Titanium Dioxide on the Removal of Toxic Dyes by the Photodegradation Technique*, 2013, 53, 55 –63.
- [8]. Shao, X.; Lu, W.; Zhang, R.; Pan, F. *Enhanced photocatalytic activity of TiO<sub>2</sub>-C hybrid aerogels for methylene blue degradation*, 2013, 3.
- [9]. Kumar, A; Pandey, G. *Preparation and Photocatalytic Activity of Co: La: TiO<sub>2</sub>Nanocomposites for the Degradation of Methyl Blue in Visible Light*, Journal Material Science 2017, 5.
- [10]. Hashemipour, H.; Salehi, M.; Mirzaee, M. *Experimental Study of Influencing Factors and Kinetics in Catalytic Removal of Methylene Blue with TiO<sub>2</sub>Nanopowder*, American J. Environmental Engineering, 2012, 2, 1-7.
- [11]. Pazouki, M.; Keyanpour-Rad, M.; Hosseinnia, A. *Photo-catalytic Degradation of Organic Dyes with Different Chromophores by Synthesized Nanosize TiO<sub>2</sub> Particles*. 2010, 8, 1327-1332.
- [12]. Herrmann J.; Houas, A.; Lachheb, H.; Ksibi, M.; Elaloui, E.; Guillard, C. *Photocatalytic degradation pathway of methylene blue in water*. Applied Catalysis B: Environmental2000, 31, 145–157.